Manipulating the reactivity of nanoscale catalysts

Conradsen, Christian Nagstrup; Chorkendorff, Ib; Nielsen, Jane Hvolbæk

Publication date:
2014

Document Version
Peer reviewed version

Ph.D. thesis
Department of Physics
Center For Individual Nanoparticle Functionality (CINF)
The Technical University of Denmark (DTU)

Manipulating the reactivity of nanoscale catalysts

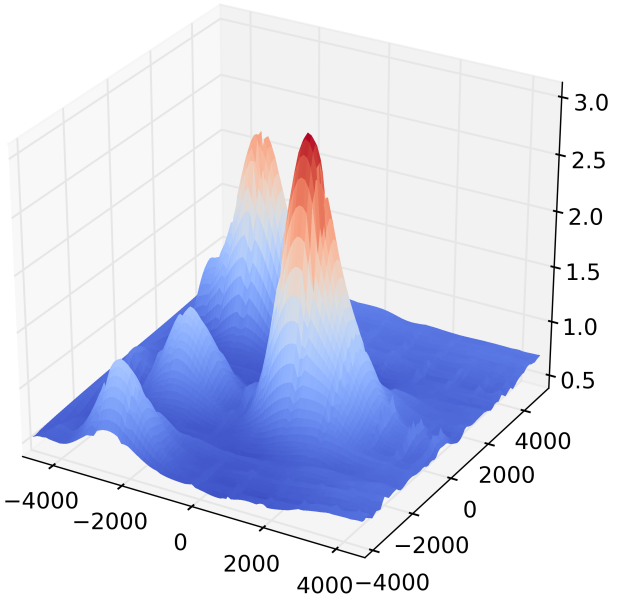

Supervisor: Prof. Ib Chorkendorff
Co-supervisor: Prof. Jane H. Nielsen

Christian Nagstrup Conradsen
December 2013

Preface

The study presented in this Ph.D. thesis has been conducted at the Center for Individual Nanoparticle Functionality (CINF), the Department of Physics at the Technical University of Denmark (DTU). The study was carried out in the period from 2010 to 2013 with Professor Ib Chorkendorff as main supervisor and Professor Jane H. Nielsen as co-supervisor. CINF is funded by the Danish National Research Foundation which is acknowledged for the support of the project and CINF. The thesis is submitted to fulfill the requirements for the Ph.D. degree at DTU.

I would like to acknowledge my main supervisor Professor Ib Chorkendorff for providing the opportunity for doing a Ph.D. at CINF. He has created a research center with a great atmosphere and working environment, intellectual and fun challenges, and interesting work field with a strong driving force towards making science. Vacuum science requires great patience and can be very frustrating in the sense of maintaining and fixing broken equipment. However, I have enjoyed the three years of challenging and interesting research done at CINF. Furthermore, I would like to thank my main supervisor for interesting, constructive and teaching discussions within the field of catalysis.
Another thanks should been given to Robert Jensen and Thomas Andersen for their help and assistance with tricky problems in general and with the automation of the experimental setup. A big thanks to Anders Nierhoff for the many hours spent on assisting in the alignment of the manipulator and python programming. Here Christian Strebel, David McCarthy and Christian Holse should also be mentioned for their assistance, discussions, good coffee breaks and proof reading the thesis. I would also like to show my gratitude to the workshop and especially Dan for helping when everything looked darkest.
I would like to thank my family and friends for all their support, good company and fun times when it was needed! Last but not least, an enormous thank you should be given to Nicoline. You always make me smile when I come home after both good and bad days of vacuum science.

Lyngby, December 1st 2013

Christian Conradsen

Abstract

This thesis presents the results of three different projects, all with focus on heterogeneous catalysis. The first part concerns the investigation of the structure sensitivity of the CO dissociation reaction on a Ru(0 1 54) single crystal and nanoparticulate ruthenium. The second part is an investigation of a model Cu/Ru system for ammonia oxidation and the deployment the system on a high surface area support. The last part of the thesis presents the dynamical changes of an industrial $Cu/ZnO/Al_2O_3$ catalyst during a pretreatment in hydrogen.

The structure sensitivity of ruthenium for the CO dissociation reaction is investigated by TPD. The importance of the step sites for CO dissociation is made clear in two separate experiments. By blocking the step sites with sulfur, carbon deposition is completely suppressed as a consequence of CO dissociation. The reverse tendency is found inducing defects to the single crystal by sputtering. The defects improve the activity of the single crystal by a factor of 8 for the methanation reaction.
CO desorption is studied on both a ruthenium single crystal and on ruthenium nanoparticles. In an collaborative project relating CO desorption, a crossover in CO desorption on a ruthenium single crystal and ruthenium nanoparticles is found. The investigation found that it is possible to shift between the CO TPD behavior of the two different systems. It is shown that sputtering the Ru(0 1 54) single crystal, a desorption profile similar to that of nanoparticles can be obtained. Equally, the desorption profile of a flat ruthenium single crystal can be obtained by annealing a thinfilm of nanoparticles to 900 K for 10 min.

In the second project it is found that forming a pseudomorphic overlayer of copper on ruthenium enhances the activity compared to both copper and ruthenium. A volcano shaped curve of the activity is found as a function of the copper overlayer thickness. The volcano has an optimum at a copper overlayer thickness of 2 Å corresponding to a coverage of 0.78 ML.
The Cu/Ru system is deployed to a real catalyst on a high surface area support. The catalyst also proved to be more active than both copper and ruthenium. The importance of Cu being an overlayer is investigated by co-evaporation and co-incipient wetness impregnation of the thinfilm and real catalyst respectively. Incorporating copper in ruthenium did not have any beneficial effect on the Cu/Ru system.

The dynamical changes of an industrial $Cu/ZnO/Al_2O_3$ catalyst are investigated by three

adsorption methods and XPS. A deviation in the copper surface area measured by H_2-TPD and N_2O-RFC is explained by the appearance of metallic zinc measured by XPS. The pretreatment in hydrogen resulted in a surface decoration of zinc on the copper nanoparticles. The findings resulted in that a reinterpretation of the methods used to determine the Cu surface area is needed. The project further made it possible to directly quantify the specific Cu and Zn areas independently.

Dansk Resumé

Denne afhandling præsenterer resultaterne fra tre forskellige projekter, alle med fokus på heterogen katalyse. Den første del af afhandlingen vedrører en undersøgelse af strukturfølsomheden af CO dissociationsreaktion på en Ru (0 1 54) enkelt krystal og på ruthenium nanopartikler. Den anden del af afhandlingen er en undersøgelse af et model Cu/Ru system til ammoniak oxidation, og implementeringen af systemet på et høj areal substrat. I den sidste del af afhandlingen præsenteres et projekt om dynamiske ændringer i en industriel $Cu/ZnO/Al_2O_3$ katalysator under en forbehandling i hydrogen.

Strukturfølsomheden af ruthenium for CO dissociationsreaktion er blevet undersøgt ved hjælp af TPD. Betydningen af trin sites for CO dissociation er tydeliggjort i to separate eksperimenter. Ved at blokere trin sites med svovl, er kul deponering som følge af CO dissociation fuldstændig undertrykt. Den omvendte tendens er observeret, ved at inducere defekter på enkelt krystalen. Defekterne har vist sig, at forbedre aktiviteten af enkelt krystalen med en faktor 8 for metaniseringsreaktionen.
CO desorption er undersøgt både på en ruthenium enkelt krystal og ruthenium nanopartikler. I et samarbejdsprojekt vedrørende CO desorption er der fundet en sammenhængen mellem denne på ruthenium enkelt krystalen og CO ruthenium nanopartiklerne. Undersøgelsen viste, at det er muligt at ændre CO desorptions adfærden mellem de to systemer. Dette er påvist, ved at beskyde Ru (0 1 54) enkelt krystalen med argon ioner for herved at opnå en desorption profil svarende til den for nanopartikler. Ligeledes kan en desorptions profil svarende til en ruthenium enkelt krystal opnås ved opvarming af en tyndfilm af nanopartikler til 900 K i 10 min.

I det andet projekt er det vist, at ved at danne et pseudomorfisk overlag af kobber på ruthenium kan aktiviteten øges i forhold til både kobber og ruthenium. Aktiviteten danner en vulkan formet kurve som funktion af tykkelsen på kobber overlaget. Denne vulkanformede kurve viser, at den optimale tykkelse af kobber overlaget er 2 Å svarende til en dækning på 0,78 ML.
Cu/Ru-systemet er videre udarbejdet til en rigtig katalysator på et høj areal substrat. Katalysatoren har ligeledes vist sig, at være mere aktiv end både kobber og ruthenium. Vigtigheden af Cu som et overlag er blevet undersøget ved henholdsvis at fordampe og imprægnere kobber samtidig med ruthenium. Dog viste det sig ikke at have nogen forbedrende effekt for Cu/Ru-systemet, at indkorperere kobber.

De dynamiske ændringer i en industriel $Cu/ZnO/Al_2O_3$ katalysator er blevet undersøgt med tre adsorptionsmetoder og XPS. En afvigelse i kobber arealet blev målt med H_2-TPD og N_2O-RFC og kan forklares ved fremkomsten af metallisk zink. En forbehandling i hydrogen har resulteret i en overflade udsmykning af zink på kobber nanopartikler.
Dette har resulteret i, at en genfortolkning af de metoder der anvendes til at bestemme Cu overfladeareal er nødvendig. Projektet har endvidere gjort det muligt direkte at kvantificere det specifikke kobber og zinc areal uafhængigt.

List of included papers

Paper I:

Probing the crossover in CO desorption from single crystal to nanoparticulate Ru model catalysts

S. Murphy, C. Strebel, S. B. Vendelbo, **C. Conradsen**, Y. Tison, K. Nielsen, L. Bech, R. M. Nielsen, M. Johansson, I. Chorkendorff and J. H. Nielsen
Published in Phys. Chem. Chem. Phys. **13** (2011), 10333-10341

Paper II:

Strong Cu-ZnO interaction in industrial type methanol synthesis catalyst: Quantification of Zn atoms in the Cu surface

S. Kuld, **C. Conradsen**, I. Chorkendorff and S. Sehested
Draft

Paper III:

Catalytic activity of model- and high surface area Cu/Ru catalyst for low temperature ammonia oxidation

C. Conradsen, S. Olsen, D. Charkraborty and I. Chorkendorff
Abstract

Contents

1 Introduction **1**
- 1.1 Energy - a global perspective . . . 1
- 1.2 Energy crisis . . . 3
- 1.3 Sustainable Energy . . . 4
- 1.4 Heterogeneous Catalysis . . . 6
  - 1.4.1 Reactivity of transition metals . . . 8
  - 1.4.2 Pseudomorphic Overlayers: Stress and Strain . . . 9

2 Experimental setup and methods **13**
- 2.1 The Parallel Screening Setup . . . 13
  - 2.1.1 The substrate - TiO_2 . . . 14
  - 2.1.2 Custom made sample holder for powder catalysts . . . 16
- 2.2 Deposition and characterization in ultra high vacuum . . . 17
  - 2.2.1 Deposition - the evaporator . . . 17
  - 2.2.2 Characterization - Temperature Programmed Desorption . . . 18
  - 2.2.3 Characterization - X-ray Photoelectron Spectroscopy . . . 19
  - 2.2.4 Characterization - Ion Scattering Spectroscopy . . . 21
- 2.3 Catalytic testing in high pressure . . . 22
  - 2.3.1 Gas sampling device . . . 22
  - 2.3.2 Gas supply system . . . 24
- 2.4 Heating the sample . . . 25
- 2.5 Automation of the setup . . . 26

3 CO desorption from single crystal and nanoparticulate Ru **29**
- 3.1 Introduction . . . 29
  - 3.1.1 The structure of ruthenium and CO . . . 30
- 3.2 CO desorption from single crystal Ru(0 1 54) . . . 32
  - 3.2.1 Cleaning the ruthenium single crystal . . . 32
  - 3.2.2 CO desorption . . . 33
  - 3.2.3 Step sites and defects of CO dissociation . . . 36
- 3.3 CO desorption from nanoparticle Ru . . . 39
- 3.4 Crossover in CO desorption from single crystal to nanoparticles . . . 40
- 3.5 Discussion . . . 43
- 3.6 Summary . . . 44

4 Ammonia oxidation on Cu/Ru thinfilms **47**

4.1 Introduction . . . 47
4.2 Fe, Ni and Pt thinfilms . . . 48
4.3 Cu and Ru thinfilms . . . 50
4.3.1 Thinfilms of co-evaporated Cu/Ru . . . 51
4.3.2 Thinfilms of Cu overlayers on Ru . . . 55
4.3.3 Cu/Ru on high surface area support . . . 57
4.4 Discussion . . . 60
4.5 Conclusion . . . 63

5 Reduction of industrial $Cu/ZnO/Al_2O_3$ catalyst 65
5.1 Introduction . . . 65
5.2 Experimental procedure . . . 67
5.2.1 Determining the specific copper area by H_2-TPD . . . 68
5.2.2 N_2O Reactive Frontal Chromatography . . . 70
5.2.3 H_2 uptake - H_2-Transient Adsorption . . . 70
5.3 X-ray Photoelectron Spectroscopy after reduction . . . 73
5.4 Discussion . . . 79
5.4.1 Geometric model . . . 81
5.4.2 Surface alloy . . . 82
5.5 Summary . . . 85

6 Summary and Conclusion 87

Bibliography 89

Included papers 97

Chapter 1

Introduction

The presented Ph.D. thesis is the culmination of three years work and has involved a number of projects within the field of catalysis. The main topic of the thesis is fundamental research in the area of heterogeneous catalysis, i.e. the interactions between solid catalysts and gas phase reactants. A surface scientific approach applying Ultra High Vacuum techniques is used to understand model systems but also to understand real working industrial catalysts. The subjects covered in the thesis have been studied experimentally. The projects have been collaborative work involving other Ph.D. students and post-docs working at other ultra high vacuum facilities in line with the scientific philosophy at CINF. The projects covered in this thesis range from fundamental research of single molecules on a surface, to a project on how surface science can go from fundamental research to designing a real catalyst with applications, before finally ending with a project on characterizing a state of the art industrial catalyst.
Catalysis is the main subject of the thesis, and is a scientific field that will play an important role for humanity in the future. Fossil fuels are running low and alternative energy sources for the future need to be developed [1]. Harvesting and storing energy from sustainable sources is often associated with catalysis. In the following sections it will be made clear how catalysis will play a crucial role when we are forced to switch from using fossil fuels to sustainable energy sources.
In this chapter the basic principles in catalysis will be introduced and used to discuss how catalysis has an enormous impact in the chemical industry. Furthermore, it will be discussed how catalysis potentially will play an even bigger role in solving the future energy crisis. Improving or inventing new catalysts will be the key issue to overcome the barriers for new inventions to come into play. An introduction to how the reactivity of a catalyst can be tuned for a specific reaction will be presented, to gain insight and understanding on how catalysis will help us in the future.

1.1 Energy - a global perspective

Global energy consumption has increased for decades as the world's population has increased, and living standards have improved. In fig. 1.1 the worldwide energy consumption is shown from 1987 to 2012. A clear trend for an increasing energy use since 1987 is seen

and in the period from 1987 to 2012 the energy consumption is almost increased by 50%.

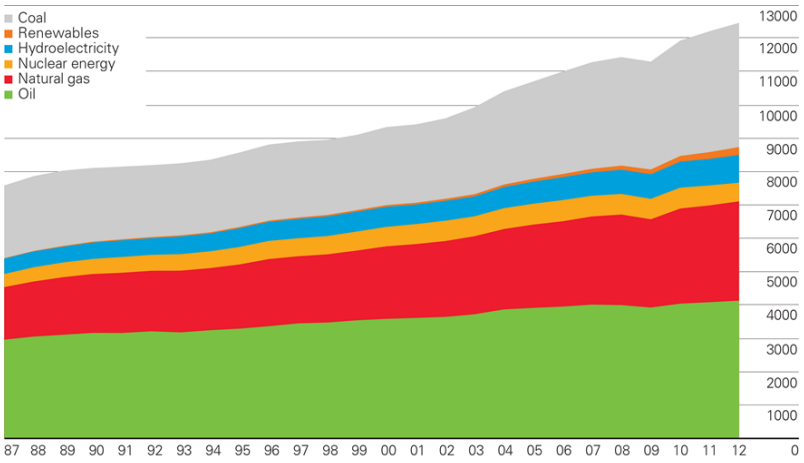

Figure 1.1: The global energy consumption since 1987. The figure is captured from [1]

From the graph it is further seen that a major part for the global energy consumption is supplied by fossil fuels. The figure tells that oil, natural gas and coal accounted for almost 75% of total energy use in 2012. The consumption of nuclear energy and hydropower is constant throughout the period. Renewable energy has gone from being non-existing to play a small role in the total consumption.
The renewable energy portion can mainly be attributed to wind and solar power. These two sources are problematic as they are intermittent; the wind power can only be harvested when the wind blows, and solar power can only be harvested during day time. This problem with intermittency is further complicated by the fact that these energy sources are used to generate electricity, which is difficult to store. This means that wind and solar power only can be deployed in the area where it is harvested, and not at times when the energy is required. This makes the current renewable energy sources inconvenient for many purposes, and they therefore cannot be relied upon as the sole energy sources.
Fossil fuels have grown to be an essential part of society. Everything from households to transportation and industry relies on having fuel and energy available at any time. Fossil fuels are extremely difficult to beat in measures of energy density, and are in general a superior and more convenient energy carrier. Oil, gas and coal have been available in large reserves which have been easy to harvest, and also easy to store. We need energy sources that combine the renewable sources of wind and solar power, with the convenience of use of fossil fuels for implementation to be realistic.

1.2 Energy crisis

The ongoing increase in the global energy consumptions have left the world with one of the biggest challenges ever faced. The living standard in most parts of the world has increased throughout the years and with this the energy consumption has followed. In fig. 1.2 an estimation of how long the fossil fuel resources will last is seen. The estimation is based on the size of reserves and the rate of the production. There exist a number of different predictions of the lifetime of the remaining reservoirs. However, most estimations are in the same order. The predictions from BP estimate that the non-OECD countries have in the order of 80 years left of both oil, natural gas and coal whereas the western world is estimated to have less than 50 years of consumption of oil and natural gas left but more than 100 years of coal. The OECD countries include Denmark, UK and the US among 34 member nations whereas nations as China, Russia and India are not members.

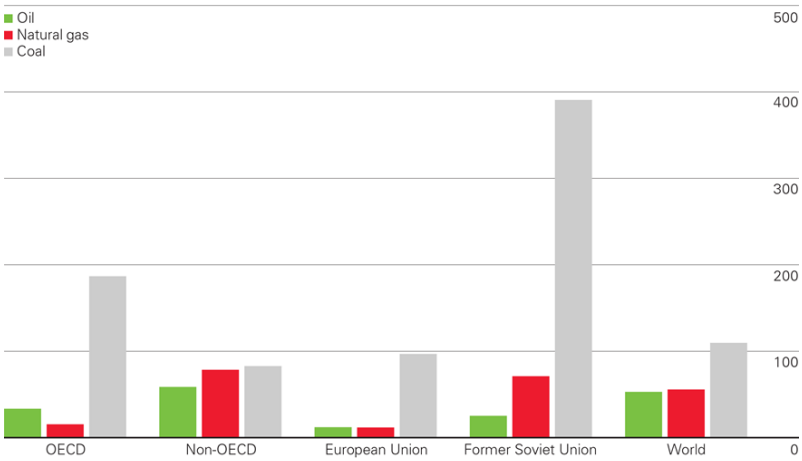

Figure 1.2: The prediction made by BP on the reserve of the different energy sources. The estimation is made on the ratio between reserves and production. Captured from [1].

As the fossil fuel reservoirs are running low, a major concern is raised. The alternatives for fossil fuels are not fully developed and this means that the world is heading towards a point where energy demand can no longer be met by supply. If alternatives to fossil fuels are not found the way society runs will have to be re-worked. Living standards in most parts of the world have increased substantially the last decades, and with this so have people's expectations and demands. However, if alternatives are not found to the current usage of fossil fuel, people's way of life will have to change substantially. As mentioned previously a major problem with the current state of renewable energy is that it cannot be stored. Imagining a society where electricity is only available when the sun shines or the wind blows is a horrific picture for most. However, this could be one of the consequences if we run out of fossil fuels and have no alternative solution ready.
One likely solution is to find a way of storing energy harvested from renewable sources

as chemical energy - ideally in a form similar to the fossil fuels currently used. However, with the current state of the art, the penalty for converting electricity into chemical energy and back to electricity costs on the order of 1/3 of the energy in each step. With the low efficiency of solar cells much effort is needed also in the process of generating and harvesting the energy. Action needs to be taken to improve the conversion steps as the alternatives to fossil fuel will take time to implement.

1.3 Sustainable Energy

The most widespread solution to the forthcoming energy crisis is to figure out how to store the wind and solar energy. The sun itself supplies 5000 times more energy than human mankind use per year and is therefore probably the best solution for the future [2]. The primary idea is to store the renewable energy as chemical energy in various forms. In fig. 1.3 the primary routes for the solution to the energy crisis are shown. Many initiatives have been taken to find materials for energy storage. Among the candidates of attention especially hydrogen and hydrogen containing materials have received notice, such as alcohols, ammonia and higher hydrocarbons. The main challenge in the work for forming fuels and energy from the sun lies in catalysis. The formation of the new energy carriers are all catalytic processes which unfortunately rely on scarce and expensive materials. For solar energy to be the main source in the future, new and better catalysts need to be found, as the current losses are in the order of 30% for each of the catalytic steps.

Hydrogen as an energy carrier has received much attention due to it having an image of being a "green energy". Hydrogen is primarily produced by reforming of fossil fuels to form synthesis gas (a gas mixture of CO and H_2) or by electrolysis of water. Even though hydrogen is receiving much attention, hydrogen as energy carrier suffers from drawbacks. The storage of hydrogen is associated with danger. Due to a low energy density, to have useful amounts of energy hydrogen must be liquefied and held at high pressure, which is ultimately dangerous in the event of an accident. The volumetric energy density of liquid hydrogen is only in the order of 1/3 of the gasoline.
One of the best candidates as a future energy carrier is methanol. Methanol has many advantages besides having a relative high energy density on the order of half of that of gasoline. Methanol only needs CO_2 and hydrogen to be produced, and it can be used to synthesize higher hydrocarbons. Also, its storage and safety considerations are much the same as gasoline. Methanol can be produced from various feedstock's ranging from coal and natural gas to potentially water and reused CO_2 from industrial waste or biomass. The synthesis conditions for methanol are relatively mild for large scale production (220°C and 70 bar) and is primarily made from direct oxidation of methane or syn-gas from fossil fuels. The dream is to produce methanol from carbon dioxide separated from the atmosphere and hydrogen provided to electrolysis of seawater.

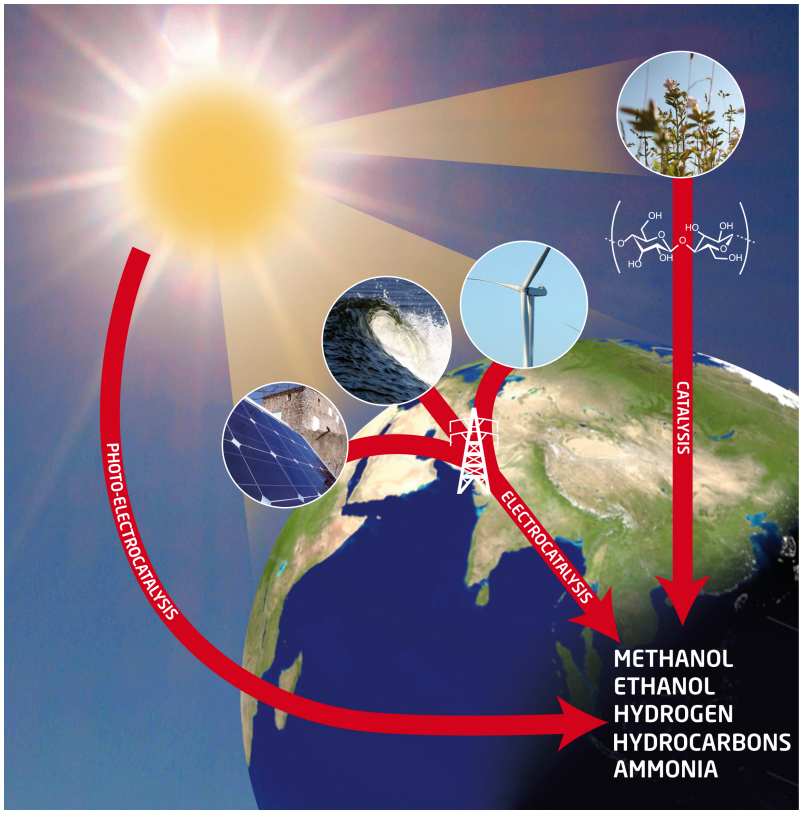

Figure 1.3: The drawing shows the main ideas of capturing renewable energy and conversion into chemical energy in different forms. Reproduced from [3].

Professor G. Olah has shared his view on the role of methanol as an important factor in the future of energy [4][5]. He suggests an environmental cycle using Carbon Capture and Recycling (CCR). In CCR methanol will be used as a convenient carbon neutral energy-storage material. It will acts as a synthetic fuel and a feedstock to synthesize hydrocarbons and their products. The dream is to form on-site production of small scale facilities as methanol as a key advantage can be produced anywhere.
Methanol stands as one the most practical and sensible approaches to eventually replace fossil fuels. The advantages of methanol make it a feasible and safe way to store energy. Methanol can potentially be an easy available and convenient liquid fuel. It can assure an unlimited source of hydrocarbons from CCR, while at the same time reducing the dangers of global warming caused by the greenhouse effect of carbon dioxide.

To break the coming energy crisis many initiatives can be taken. Limiting the energy consumption seems like the obvious way to prolong the lifetime of the fossil fuels reserves and thereby postponing the energy crisis. However, the increasing world population and the demand for higher standard of living make this scenario appear unrealistic. Therefore optimization within the area of catalysis is important. For catalysis to become a viable

way of storing renewable energy, better and cheaper materials are needed. Many state of the art catalysts contain platinum however the energy crisis will not be solved if all future catalysts rely on platinum. In such a case, the amount of platinum would quickly become a limiting factor. It is therefore also important when searching for the solution to the energy crisis to search in a broad spectrum of ideas.

The scope of the thesis will be to present three studies of cases of catalysts optimized for their specific use. The techniques needed to fulfill the task will be explained to gain insight to the principles and understand further discussion on the topic of optimizing catalysis. The three cases presented all fall within the field of heterogeneous catalysis but with aims for different applications. The presented work is mostly fundamental research but with different purposes. The first project involves finding the active site for CO splitting on ruthenium. The second project is a fundamental research of optimizing a catalyst and deploying the knowledge to a real catalyst on a high surface area support. The third and last project deals with characterization of a real working industrial catalyst.

1.4 Heterogeneous Catalysis

The definition of a catalyst is a compound which accelerates a chemical reaction without being consumed in the reaction. The basic principle of a catalyst is shown in fig. 1.4(a) where two reactants, A and B, approach a catalyst and bind to the surface. On the surface the two reactants react and form the product P which then desorbs from the catalyst leaving the surface free for the next reaction. The principle of a catalyst is further elaborated in fig. 1.4(b) where a schematic drawing shows the potential energy of a reaction for the different reaction coordinates with and without a catalyst. The Gibbs free energy in fig. 1.4(b) is the key to understand why the catalyst accelerates the chemical reaction of forming reactant A and B into the product P. The figure shows the change in Gibbs free energy for a reaction path with and without a catalyst. The path of the reaction with the catalyst is more complex with many steps compared to the non-catalytic path. The key point is smaller energy barriers for each of the steps compared to the non-catalyzed reaction.

Another important consequence of the catalyst is the reverse reaction is unfortunately also catalyzed. Here it is important to state that a catalyst never beats thermodynamics and that a certain reaction never will occur if it is energetically unfavorable. A catalyst only accelerates the reaction. This means that the equilibrium cannot be changed but only the rate to reach it.
Catalysis can in general be divided into two groups, homo- and heterogeneous catalysis. The type of catalysis is determined by the phase of the reactants, product of the reaction and the catalyst. In this work only heterogeneous catalysis has been investigated which means the reactants and the products usually are in gas or liquid phase whereas the cata-

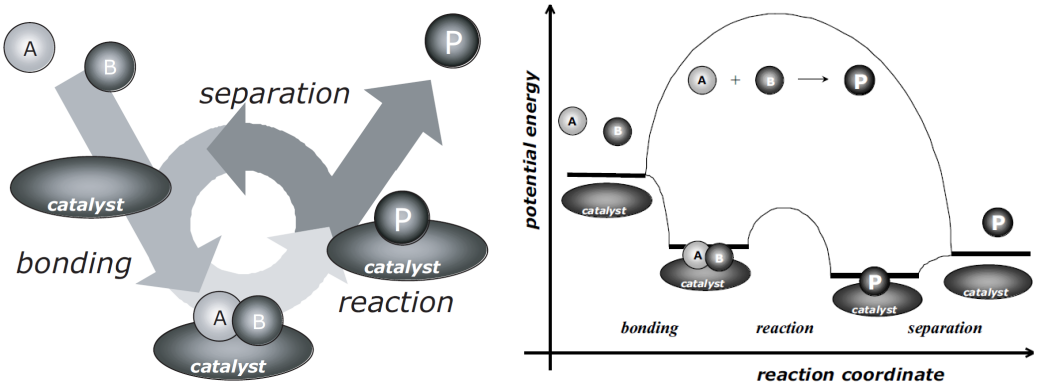

(a) (b)

Figure 1.4: The figure shows the basic principle of a catalyst working in cycles of reactants, reaction and product. The principle is further elaborated in figure b where the potential energy of the separate reaction coordinates with and without a catalyst is seen. Both figures are adapted from [6].

lyst is a solid.
Producing the optimal catalyst for a given reaction is not trivial. The interaction between the catalyst, reactants and the product is a difficult task to optimize. If the binding between the reactant and the catalyst is too strong or too weak the effect of the catalyst may not be sufficient. A too strong binding of the reactant to the catalyst surface will make the system too stable and prevent the reactants to react with each other. A too weak binding between reactants and catalyst will on the other hand limit the formation of the product. The optimal catalyst therefore binds the reactant not too strong nor to weak. This dilemma is known as Sabatiers principle, dictating that there exists an optimum binding strength of a given catalyst. This leads to a volcano shaped curve in the reaction activity as a function of the binding energy of rate limiting step. The rate limiting step is used as a descriptor since this parameter is dictating the speed of the reaction.

Catalysis is a surface phenomenon with the reactants only having an interaction with the surface. When designing a real catalyst the dispersion of the material is therefore extremely important. As mention earlier, most catalysts are made of scarce metals. Since it is the surface that serves as catalyst, it is extremely important to maximize the surface area per weight of metal. Industrial catalysts are therefore often dispersed on high surface area supports as nanoparticles to optimize the specific surface area.

1.4.1 Reactivity of transition metals

The reactivity of a catalyst is a measure of how strong intermediates interact with the surface. The right reactivity of the material is crucial for the catalyst. The reactivity of a catalyst can in more detail be explained by the electronic structure of the surface of the catalyst and the density of states. The Density Of States (DOS) for a transition metal around the fermi-level consist of a partially filled broad sp-band and a narrow d-band. With respect to the sp-band the metals behave like a free electron metal whereas many properties of the metal are linked to the filling of the d-band. The reactivity of the metal can be described by the Newns-Anderson model. The model utilizes the tightbinding model to describe how the hybridization energy changes as an adsorbate approaches a surface. By use of the model it is possible to describe trends in reactivity for transition metals across the periodic table [7].
The fundamental principles of the Newns-Anderson model can be explained from fig. 1.5 which illustrates the physics of a molecule approaching a metal surface. The left hand side of the illustration represents a transition metal with a broad sp-band and a d-band localized at the fermi level. The right hand side illustrates a molecule and its bonding and anti-bonding orbital. When a molecule approaches the surface, the molecule feels a weak attractive Van der Waals force interaction. As the molecule gets closer to the metal surface it interacts with the sp-band and the orbitals split up into broader molecular levels making the molecule bind to the surface. The d-band interaction splits the electronic levels of the molecule in a bonding and anti-bonding state. The interaction makes the bonding orbital shift upwards whereas the antibonding orbital shift down in energy. The fermi level of the metal surface levels out to the adsorbate and fills the bonding and antibonding orbital fully or partially. The degree of filling of the anti-bonding level weakens the internal bond of the adsorbate and at a certain point the adsorbate might dissociate while strengthening the binding of the dissociated product to the surface [8].
The Newns-Anderson model describes how a catalyst facilitates the dissociation of a molecule. The important conclusion is the interaction between the molecule and the sp-band primarily contributes to the bonding of the adsorbate to the surface. The interaction between the metals d-band and anti-bonding molecular orbital determines whether the adsorbed molecule dissociates. The center of the d-band determines the filling degree of the anti-bonding molecular level and hereby the reactivity of a transition metal surface. The position of the d-band center is therefore the crucial parameter for understanding the variations in reactivity through the transition metals.

The importance of the d-band filling and position is seen in fig. 1.6 where the activity towards ammonia synthesis is plotted as function of the d-band filling for a number of transition metals. The figure shows a beautiful example of Sabatier's principle with an optimum for a specific d-band filling and thereby a specific binding strength of N_2. The metals positioned left of the optimum is able to dissociate the N_2 but the molecular nitrogen is bound too strongly to the surface making the metals less active. The metal to the right is unable to dissociate the N_2 and is therefore also less active than the optimal

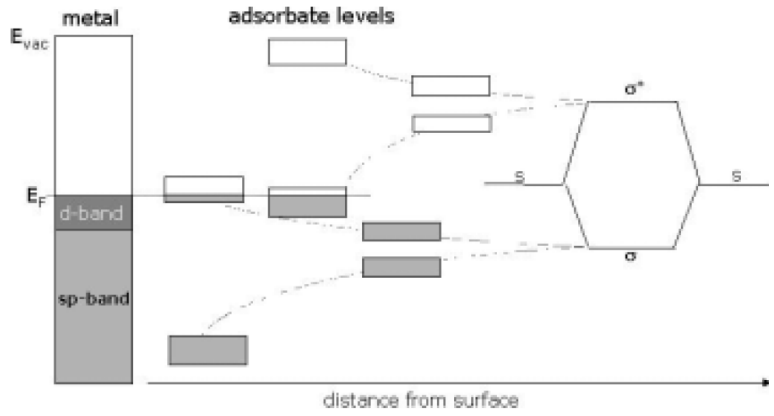

Figure 1.5: Illustration of a molecule with a bonding and antibonding orbital approaching a transition metal surface. As the molecule approaches the surface the molecular levels of the adsorbate broaden. The figure is adapted from [6]

catalyst. Sabatier's principle gives an indication of how to find the optimal catalyst for a given reaction. The optimal catalyst for a given reaction is therefore always subjected to a compromise between a low activation barrier and intermediate bonding of adsorbates.

For many reactions scarce metals are placed on top of the volcano, such as platinum, rhodium and iridium. This means the prices are sky high and the metals are only available in limited amounts. This makes the tasks for tailoring the reactivity of a catalyst harder as cheaper and abundant materials are less favorable in terms of catalytic activity. In the end, when tailoring catalyst it is often the activity per price that matters.

1.4.2 Pseudomorphic Overlayers: Stress and Strain

The importance of choosing the right catalyst has been pointed out and it shall now be discussed how the reactivity can be tuned by manipulating the position of the d-band. The d-band is crucial for the reactivity of a catalyst surface. So far only pure metals and their d-band have been addressed when discussing the tuning of reactivity for a given reaction. Another way to tune the reactivity of the catalyst surface is by forming a pseudomorphic overlayer. The definition of a pseudomorphic overlayer is an overlayer which follows the lattice structure of the underlying substrate hereby either straining or compressing the lattice of the overlayer. The stress introduced to the overlayer will change the overlap of the electron orbitals hereby narrowing or broadening the d-band. As the fermi level is unaffected by this procedure, the center of the d-band will as a consequence shift either up or down in order to keep a constant d-band filling. The change is d-band position ultimately changes the binding properties of the surface.
The principle is schematically shown in fig. 1.7 for an overlayer of smaller lattice constant.

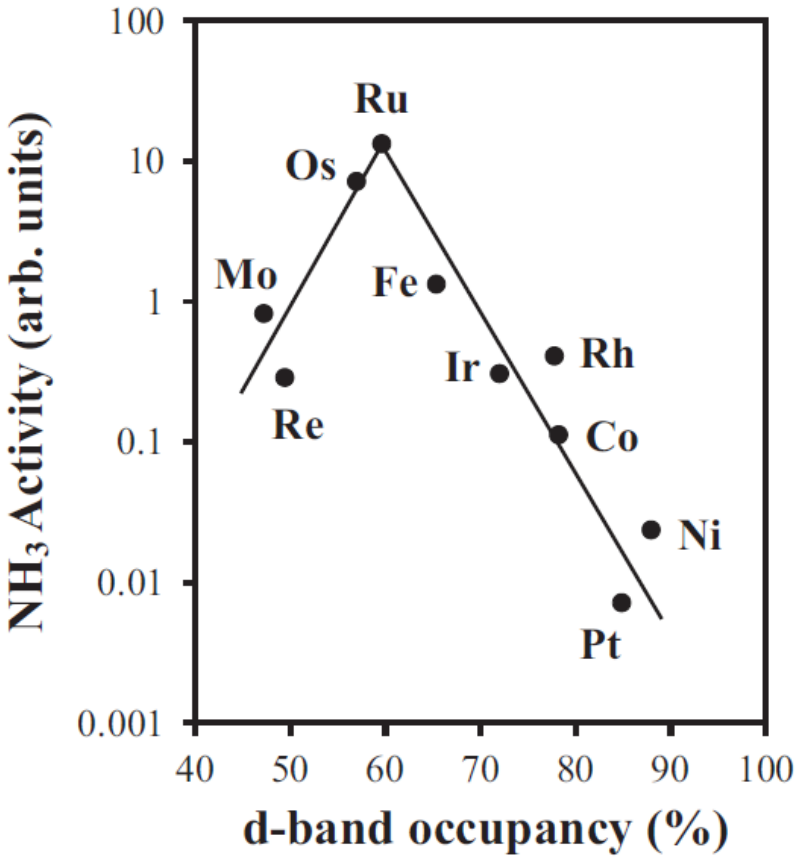

Figure 1.6: The figure shows the activity for ammonia synthesis for different transition metals as function of the d-band filling. The figure is adapted from [6] and is originally from [9].

As the overlayer follows the structure of the underlying substrate, the lattice of the pseudomorphic overlayer is strained. As a consequence of the straining the d-band becomes narrower and to keep the same filling degree of the d-band the center is shifted upwards.

The trends in reactivity of pseudomorphic overlayers have been calculated by DFT in a large study by Ruban *et al.*. In fig. 1.7, a table showing the shift in d-band center for pseudomorphic overlayers on a number of transition metals is seen. The diagonal represents the position of the d-band for a pure transition metal surface. The table shows how it is theoretically possible to tailor the reactivity of the surface, making the surface either less or more reactive, by adding an overlayer. Equally to pseudomorphic overlayers, the surface reactivity can be changed by making a surface alloy replacing surface atoms with smaller or larger atoms. This effect also causes a strain or compression of the surface layer of the catalyst and thereby changes the reactivity of the catalyst. This phenomena has been thoroughly investigated for the electrochemical Oxygen Reduction Reaction. In this study,

Overlayer	Fe	Co	Ni	Cu	Ru	Rh	Pd	Ag	Ir	Pt	Au
Substrate											
Fe	**-0.92**	0.24	-0.04	-0.05	-0.73	-0.72	-1.32	-1.25	-0.95	-1.48	-2.19
Co	-0.01	**-1.17**	-0.20	-0.06	-0.70	-0.95	-1.65	-1.36	-1.09	-1.89	-2.39
Ni	0.96	0.11	**-1.29**	0.12	-0.63	-0.74	-1.32	-1.14	-0.86	-1.53	-2.10
Cu	0.25	0.38	0.18	**-2.67**	-0.22	-0.27	-1.04	-1.21	-0.32	-1.15	-1.96
Ru	0.30	0.37	0.29	0.30	**-1.41**	-0.12	-0.47	-0.40	-0.13	-0.61	-0.86
Rh	0.31	0.41	0.34	0.22	0.03	**-1.73**	-0.39	-0.08	0.03	-0.45	-0.57
Pd	0.36	0.54	0.54	0.80	-0.11	0.25	**-1.83**	0.15	0.31	0.04	-0.14
Ag	0.55	0.74	0.68	0.62	0.50	0.67	0.27	**-4.30**	0.80	0.37	-0.21
Ir	0.33	0.40	0.33	0.56	-0.01	-0.03	-0.42	-0.09	**-2.11**	-0.49	-0.59
Pt	0.35	0.53	0.54	0.78	0.12	0.24	0.02	0.19	0.29	**-2.25**	-0.08
Au	0.53	0.74	0.71	0.70	0.47	0.67	0.35	0.12	0.79	0.43	**-3.56**

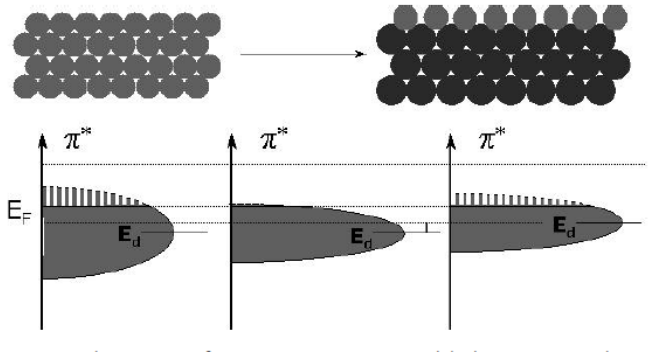

Figure 1.7: The table shows the trends in reactivity for a pseudomorphic overlayer on a substrate. The diagonal represents the position of the d-band for a pure transition metal whereas the off-diagonal represents the shift in d-band. The figure below shows the basic principle of a pseudomorphic overlayer of smaller lattice constant deposited on a substrate of larger lattice. Furthermore, the shift in d-band center is seen as consequence of a narrowing of the d-band. The table is adapted from [10] and the figure from [6].

a small shift in d-band center for a platinum catalyst was induced by alloying with other transition metals greatly increasing the activity [11].
The stability and segregation of the overlayers is discussed and calculated by Ruban *et al.* [12]. The DFT screening study gives an excellent starting point to manipulate the position of the d-band for a specific reaction.
Tuning the reactivity of a catalyst for a specific purpose is scientifically a very elegant way of optimizing a catalyst. Furthermore, it makes it possible to find cheaper and better alternatives to the noble and expensive metals as the composition of overlayers or alloys allows for several new combinations of catalysts. This aspect is crucial for producing new catalysts as it can both optimize good catalysts but also enable the use of cheaper and more abundant materials.

Chapter 2

Experimental setup and methods

In this chapter the experimental setup used for the study will be described. The single techniques and methods used will be explained shortly and the typical procedure for experiments shown.

2.1 The Parallel Screening Setup

The experimental setup is in familiar terms known as the Parallel Screening setup (PS). The name is given on behalf of the setups main strength, i.e. testing a series of catalyst in parallel. A schematic drawing of the setup is shown in fig. 2.1. The setup operates in Ultra High Vacuum and is mainly pumped by a molecular turbo pump and ion pump. Furthermore, differential pumping of specific techniques is applied. The base pressure of the setup is 10^{-10} Torr.
The setup consists of three larger chambers, referred to as the preparation chamber, analysis chamber and the High Pressure Cell (HPC). During experiments, the HPC can be filled to 1 bar of reactant gas, while a UHV lock ensures that UHV is not broken in the main chamber during experiments. The sample can be moved between all three chambers by a custom made manipulator with power and C-type thermocouple feedthroughs.
The chamber in the right side of fig. 2.1 is the preparation chamber. The preparation chamber has three main components which are a sputter gun, an Oxford Applied Research H-PEB4 electron beam evaporator and a Quartz Crystal Microbalance. Here the sample can be cleaned before experiments, and the rates of the evaporator can be measured and the deposition of metal catalyst can be done.
The center chamber of the setup is the analysis chamber. Here a number of techniques are available for characterization of the catalyst before and after high pressure testing. The analysis chamber has two main characterization techniques available, namely ion scattering spectroscopy (ISS) and x-ray photoelectron spectroscopy (XPS). Both techniques are measured with a SPECS HSA Plus hemispherical analyzer.

During this work a mass spectrometer was equipped on the Parallel Screening setup. The mass spectrometer is attached to a linear motion and a copper sniffer with a 1 mm opening.

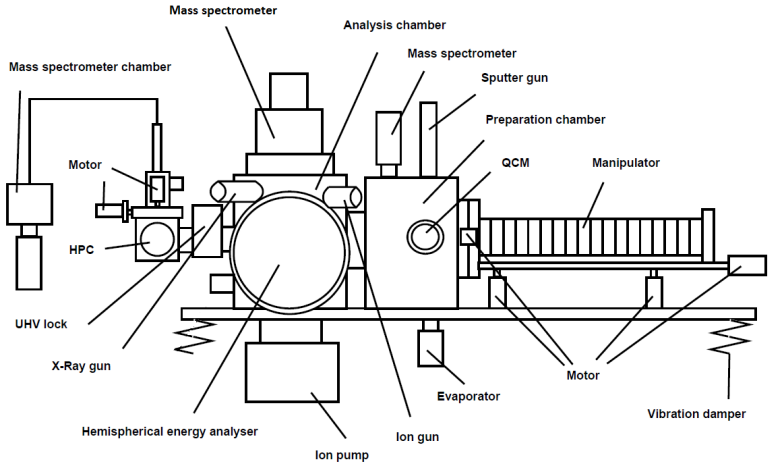

Figure 2.1: The figure shows a schematic drawing of the Parallel Screening setup.

This makes it possible to approach the surface under investigation and to do temperature programmed desorption experiments. The mass spectrometer is differentially pumped with a turbo pump and can also be bypassed for leak testing.
The last chamber on the setup is the high pressure cell seen on the left hand side of fig. 2.1. The HPC is equipped with a special gas inlet and outlet device which will be explained in detail in sec. 2.3.1. The device serves as inlet for the reactant gases and as a sniffer which samples a fraction of the gas with the attached mass spectrometer. The pressure in the high pressure cell is controlled with a pressure controller which is pumped through a roughing line.

2.1.1 The substrate - TiO_2

The substrate used in this study is a square piece of a rutile (110) TiO_2 single crystal. The TiO_2 is cut in a square of 10x10 mm^2 with a thickness of 1 mm and polished on one side. The small piece of TiO_2 is attached on a graphite disk together with the thermocouple. In fig. 2.2 a schematic drawing of the sample, sample holder and thermocouple is shown. The TiO_2 is attached using carbon glue. The glue has a thermal expansion coefficient in the same order of range as both the graphite disk and the TiO_2 and therefore can sustain its grip during heating. The graphite disk is suspended on two tungsten wires which also work as filaments. On the side of the TiO_2 disk the C-type thermocouple is attached.

The TiO_2 crystal is cleaned by Ar^+ sputtering and annealing to 1000 K in vacuum. This leaves the crystal surface in a reconstructed TiO_2 (110)-(1x1) structure [13]. This structure is maintained at high temperatures in both reducing and oxidizing conditions. Before a new series of experiments is started, the cleanliness of the sample is always checked with ISS after cleaning to ensure all metal residuals have been removed. Normally the crystal

is clean after 24 h of sputtering.

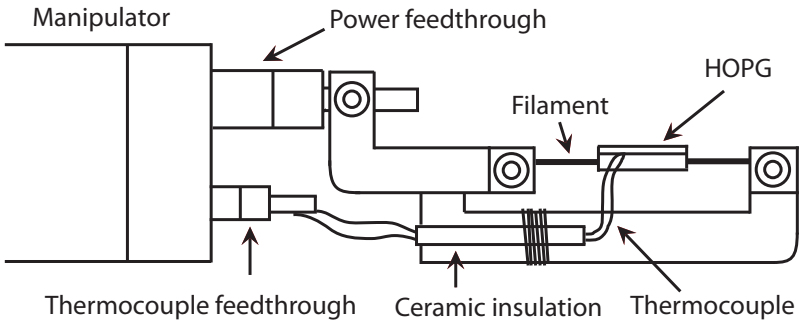

Figure 2.2: The figure shows a schematic drawing of the sample and the sample holder. The filaments suspend the graphite disk on which the TiO_2 is attached. The thermocouple is placed on the side of the TiO_2.

TiO_2 was chosen as the substrate for the experiments presented in this thesis, as it was deemed superior for various reasons to a number of other candidates, e.g. carbon and SiO_2. TiO_2 is a very well-studied, both theoretically and experimentally [13]. When choosing a suitable substrate for the setup, one needs to determine the requirements for the specific project. To use the two characterization techniques XPS and ISS, the sample needs to be conducting to avoid charging effects from negatively charged electron and positively charge ions respectively. In this case mainly two properties of the substrate are important, namely the conductivity of the substrate, and the ability with which it can be regenerated. TiO_2 is a good option in both these regards, as it is conducting and the original structure can easily be re-obtained by annealing. It is important to have the same starting point of the substrate for every experiment to make sure that it is the freshly deposited metal that is investigated, not the materials from prior experiments. Changing the substrate for each experiment is not an efficient option. Furthermore, when cleaning the sample the catalytic spots are removed by destructive sputtering. During sputtering, the top layers are removed, and for TiO_2 the original configuration of the surface can easily be returned by annealing.
However, using TiO_2 also has some disadvantages. TiO_2 is known to have a Strong Metal Support Interaction (SMSI) with a number of transition metals, including Fe, Co, Rh, Ir, Ni, Pd and Pt [13]. This is an effect clearly seen when TiO_2 is reduced and the Ti becomes mobile and creeps on top of the metals. The Ti creeping up on the metals completely deactivate the catalyst, and therefore this group of metals cannot be study with TiO_2 as substrate.

It is very unfortunate that such a large group of metals are excluded. However, for our purposes TiO_2 is still considered to be the best alternative. Other options could be graphite or other carbon substrates, however carbon poisoning is often seen, even though it matches the requirements for conductivity and reconstruction.

Other typical substrates in catalysis are different kinds of oxides, e.g. SiO_2/Si, Al_2O_3/Al, MgO/Mg. These substrates are conducting and are used in many studies for XPS, ISS and scanning tunneling microscopy. The problem with thin oxides, e.g. 10-100 nm, is that the underlying structure has great alloying power which is also the reason for the likelihood of oxidizing. This means that only a small defect in the oxide can ruin the deposited catalyst. Furthermore, when cleaning the substrate and removing the deposited catalyst the destructive sputtering will remove the oxide layer which then need to be reformed. Attempts to do this in vacuum were not successful by previous operators of the setup.
Bulk oxides, i.e. SiO_2, Al_2O_3, MgO, do not alloy with the deposited metal, but unfortunately as they are very good insulators, they are unsuitable for our investigations.

2.1.2 Custom made sample holder for powder catalysts

For investigations of powder catalysts in UHV a custom made sample holder is designed. The sample holder is made for catalyst powder made into pellet disks of 6 mm diameter. The holder is made in stainless steel and is suspended on the two tungsten wires which also heat the holder. The sample holder is carved like a cup with a small recess with room for the pellet. The cup is sealed with a lid with a 4 mm circular hole whereby the catalyst can be exposed to surface sensitive methods. A C-type thermocouple is fixated between the sample holder lid and the catalyst pellet. The sample holder is seen in fig. 2.3.

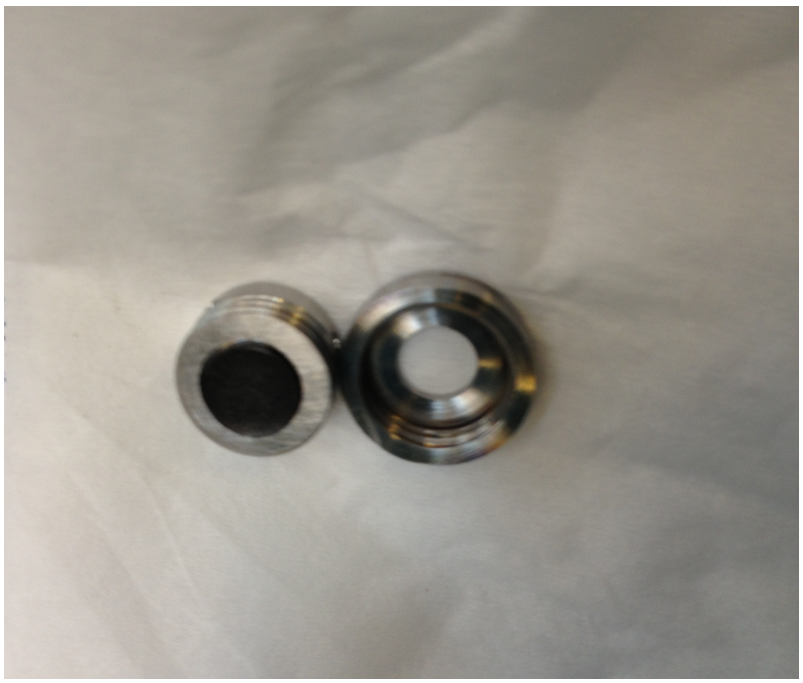

Figure 2.3: The picture shows the sample holder for investigations of powder catalysts.

2.2 Deposition and characterization in ultra high vacuum

This section will introduce the formation of the catalysts and techniques used in the study for characterization before and after high pressure testing. The techniques will only be briefly explained whereas further discussion will be elaborated in analysis of data.

2.2.1 Deposition - the evaporator

The catalysts prepared on the Parallel Screening Setup are deposited by Physical Vapor Deposition. An Oxford Applied Research H-PEB4 electron beam evaporator is used for this purpose. The evaporator can hold up to four metals at time, each placed in separate pockets in small crucibles made of Mo, C or W depending on the metal evaporated. The pockets works as separate evaporation sources but can also be operated in parallel. The E-beam evaporator works by applying a high voltage potential of 2 kV on the crucible. Electrons are accelerated to the metal and crucible from a hot filament placed in line of sight.
The rate of deposition is determined by a Quartz Crystal Microbalance (QCM) which is placed in front of the evaporator before and after deposition. Changes in the rate during evaporation will throughout the thesis be denoted with error bars. The size of the catalytic spots deposited on the TiO_2 single crystal are controlled by three different sized of circular masks which is placed in front of the evaporator instead of the QCM. The sizes of the masks are 1, 2 and 3 mm. A shutter is placed in between the evaporator and the mask. The shutter blocks the deposition of metal until a steady deposition rate is achieved.
Figure 2.4 shows the sequence of a typical experiment on the parallel screening setup. The manipulator is moved after each deposition and several catalytic spots are evaporated onto the TiO_2 substrate. The spots are afterwards characterized before being transferred to the high pressure cell where the catalytic spots are tested at high pressure of reactant gas.

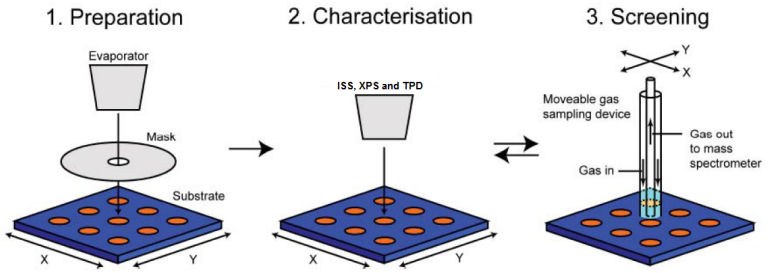

Figure 2.4: The figure shows the sequence of a typical experiment on the parallel screening setup. Catalytic spots are evaporated on the clean TiO_2 substrate before being characterized and transferred to the high pressure cell for catalytic testing.

2.2.2 Characterization - Temperature Programmed Desorption

Temperature Programmed Desorption (TPD) is a quick and powerful surface sensitive tool to probe adsorption and desorption from surfaces. The method is quite simple: a molecule is adsorbed on the surface of the metal which is then heated in a linear ramp, often 2 K/s, while tracing the molecule with a mass spectrometer. The temperature of desorption is correlated to how strong the binding between the molecule and surface is.
If re-adsorption is ignored and infinite pumping speed assumed, the relative rate, r, of first order desorption can be expressed as the change in adsorbed coverage (θ) per time:

$$r = -\frac{\mathrm{d}\theta}{\mathrm{dt}} = \nu(\theta)\theta \exp\left[-\frac{E_{\mathrm{des}}(\theta)}{RT}\right] \quad (2.1)$$

$$T = T_0 + \beta t \quad (2.2)$$

where θ is the coverage, t is the time, ν is a pre-exponential factor depending on the coverage, E_{des} is the activation energy of desorption, T is the temperature, T_0 is starting temperature and t is the time.
Though the TPD experiment is a relatively simple and quick experiment, it is a strong and powerful tool. Changing parameters in the experiment and in combination with other surface sensitive techniques, much knowledge on the surface can be gained. Some of the basic techniques in the TPD experiments used in the different projects during the Ph.D. project will be briefly discussed.

Gas
The choice of gas is very important for the TPD experiment depending on what is probed. Dissociation and scrambling can be measured by dosing labeled gasses.
Low doses
For first order desorption useful information can be gained by dosing lower coverage's than a full monolayer, combined with other techniques such as STM or LEED which might reveal exact locations of the adsorbed molecules.
Cooling
For specific cases desorption occurs at temperatures lower than room temperature. A cooling stage is required to measure H_2 and CO desorption from for example copper surfaces.

The linear motion allows the mass spectrometer to go very close to the surface, calibrated by a tracing the argon signal at constant argon pressure. The heating ramp is controlled by a PID and calibrated to a heating ramp of 2 K/s.

2.2.3 Characterization - X-ray Photoelectron Spectroscopy

X-ray Photoelectron Spectroscopy (XPS) is based on the photoelectric effect. When a surface is bombarded with photons an electron can absorb the energy and leave the atom if the kinetic energy is sufficient to overcome the vacuum level. The kinetic energy of the escaped electron will reflect the photon energy and the binding energy of the electron in surface. In experiments the HSA is used to measure the kinetic energy of the photoelectron. The relation between the incoming photon and the photoelectron can be expressed by:

$$E_{kin} = h\nu - E_{binding} - \phi, \tag{2.3}$$

where $h\nu$ is the photon energy given by Plancks constant and the frequency ν. $E_{binding}$ is the binding energy of the electron and ϕ is workfunction of the analyzer. The principle of the photoelectric process is shown in fig. 2.5(a). As the electron escapes the surface a vacancy is left in the core level from the excited electron. A secondary process can then occur where an electron relaxes into this now unoccupied state, which gives rise for an electron to be excited to above the vacuum level, which is known as the Auger process, fig. 2.5(b).

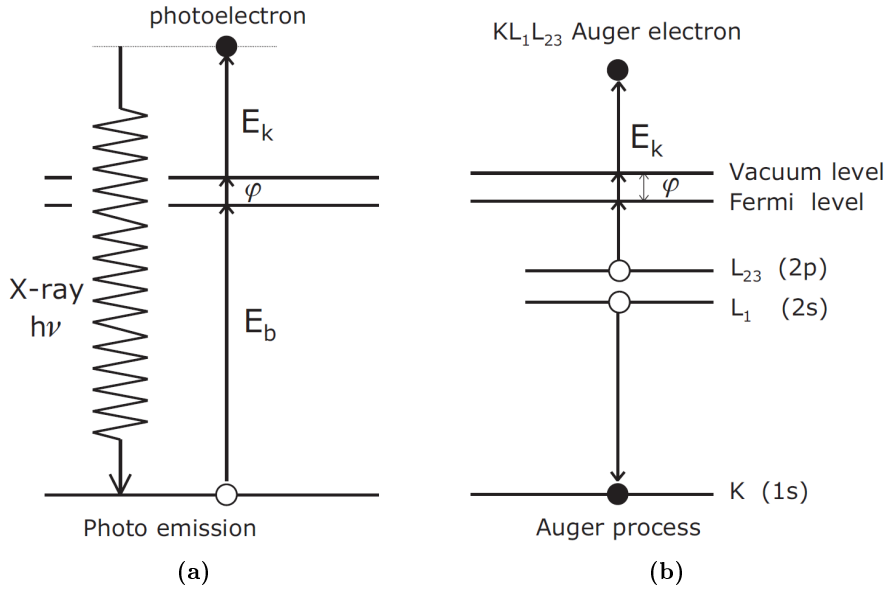

Figure 2.5: Fig. A: The principle of the photoelectric effect. The electron is excited by the incoming photon and kinetic energy of the electron is measured. Fig. B: The principle of the Auger process. The Auger electron is excited by the relaxation process of filling an initially created hole. Adapted from [6].

The surface sensitivity of XPS is determined by the travel length of the electrons in a solid. Photons penetrate deep, in the order of microns, into the surface and excite the photoelectron. However, the travel length of the electron is much shorter, in the order of 0.1-10 nm. The short travel length of electrons is primarily due to four loss mechanism, namely plasmons, phonons, ionization and excitons. In fig. 2.6(a) the travel length is plotted against the electron energy. In typical XPS spectrum the energy of the photoelectron is in the range 50-1000 eV which means only up to the first 20 Å in the surface is probed.

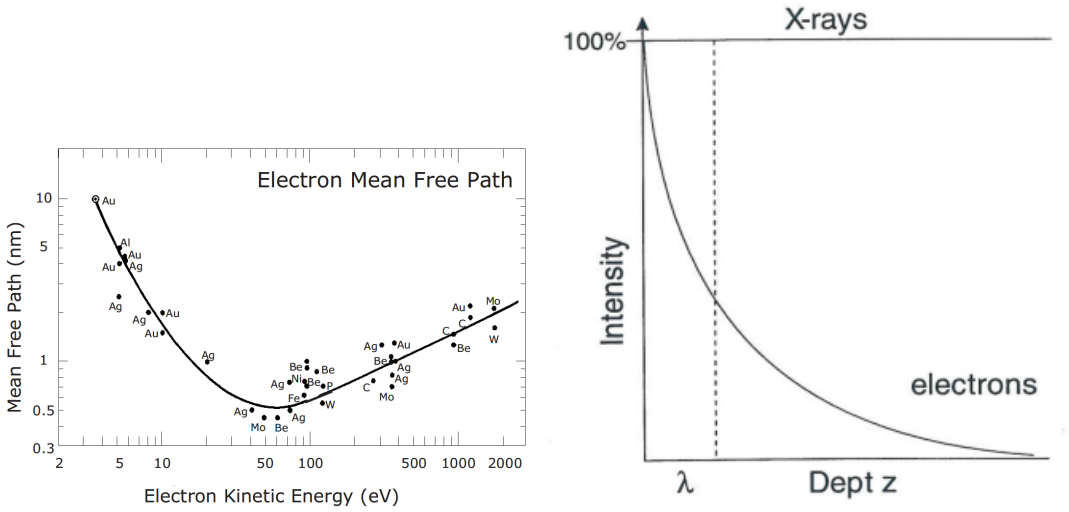

(a) (b)

Figure 2.6: Fig. A: The universal curve showing the mean free path of an electron in a metal as function of the kinetic energy. Adapted from [14]. Fig. B: A schematic of the travel length of a x-ray and an electron. Adapted from [15].

On the Parallel Screening setup the photons are made in a dual anode x-ray source of Al and Mg. The two sources can provide characteristic k_α lines of 1486.3 eV and 1253.6 eV photon energy respectively. The electrons emitted from the sample surface are measured by a hemispherical analyzer (HSA). The HSA measures the kinetic energy of the electrons from both the photoelectric effect but also from the Auger process. The two types of peaks in a typical XPS spectrum can be distinguished by switching between the two sources. The binding energy of the measured electrons from the photoelectric effect are independent of the photon energy while the kinetic energy of the Auger electrons from the Auger process are independent on the photon energy.
Furthermore, special features such as ghost peaks which originate from contamination of the anode and satellite peaks from other x-ray lines will be found in the XPS spectra. These features have however not played an important role in any analysis.
The spatial resolution in the XPS measurements is set by the lens mode of the analyzer. The lens mode and slits are optimized for each experiment, assuring only the catalyst is probed.

2.2.4 Characterization - Ion Scattering Spectroscopy

Ion Scattering Spectroscopy (ISS) is an extremely surface sensitive method which relies on inelastic scattering of ions on a surface. An inert atom, He, Ne or Ar is ionized and accelerated into the surface of investigation. The ion will scatter on the surface and the energy of the ion can be measured by a hemispherical analyzer. The principle is seen in fig. 2.7.

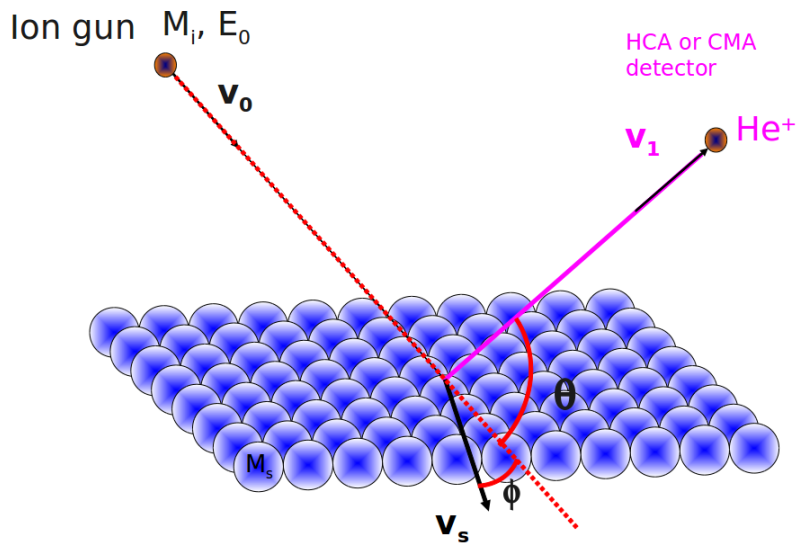

Figure 2.7: The image shows a drawing of the principle of ISS. An incoming ion is scattered on the surface and loses energy depending on the atom hit. Adapted from [15].

The scattering between ion and surface is a binary collision with conservation of energy and momentum. Knowing the mass and energy of the incoming ion and as well as the angle between ion gun and analyzer and measuring the energy of the scattered ion, simple math leads to the mass of the surface atom in the collision.
The energy ratio between the incoming ion, E_0, and scattered ion, E_1, if the mass of the incoming ion is much smaller than the mass of the surface atom $M_i << M_s$, is given by:

$$\frac{E_1}{E_0} = \left(\frac{\sqrt{M_s^2 - M_i^2 \sin^2(\theta)} + M_i \cos(\theta)}{M_s + M_i} \right)^2 , \tag{2.4}$$

where θ is the scattering angle. The technique is in principle light sputtering of the surface and one needs always to be careful how destructive ISS is to the surface. The destructiveness of ISS depends primarily on the mass of the incoming ion and is minimized when using He^+ ions. Equally, heavier atoms can be used for depth profiling as it is more destructive. ISS also has limitations as elements with Z numbers close to each other can be difficult to distinguish.

On the Parallel Screening setup normal operation is 2×10^{-8} Torr He with 1 keV energy ions and an angle of 50^o between ion gun and analyzer.

2.3 Catalytic testing in high pressure

The High Pressure Cell is a nickel free steel cube with three ports and windows. The sample is locked in the high pressure cell with a thick copper gasket for multiple usages. The HPC further has a complex gas sample device which acts as both gas inlet and gas sampling device. The HPC can withstand pressures up to 1 bar and is connected to a gas manifold with up to four different gases. The outlet of the HPC is connected to a roughing line.

2.3.1 Gas sampling device

The name of the setup, the Parallel Screening, comes from the special designed gas sampling device. The reactant gas is flowed into the HPC through the gas inlet seen in fig. 2.8. Inside the gas inlet tube a pyrex capillary is fixated with a narrow opening leaking gas to a QMS. The opening which reduces the pressure by a factor 10^{-6} is made by melting the pyrex, and directly couples the HPC to a QMS which measures a fraction of the gas in the high pressure cell. The QMS is differentially pumped by a dedicated turbo pump. The pressure in the HPC is controlled by a pressure controller pumped by a forepump. In the end of the gas inlet tube a nozzle of pure aluminum is attached with a T-shaped cross section. The gas inlet tube and pyrex capillary is mounted on a motion control device that through step motors can be controlled in both the x, y and z-direction in steps of 0.1 mm.

The aluminum nozzle is perfectly aligned with the substrate ensuring the distance between the nozzle and the TiO_2 is equal all over the TiO_2 surface. The nozzle can be moved from spot to spot, and because of the small aperture measures the catalytic activity of each individual spot without spillover from neighboring spots. The flow of the inlet gas and the distance between the nozzle and the surface makes a gas pocket without spillover from neighboring spots. In fig. 2.9 a model of the flow is seen for the gas sampling device.
The model is made with Computational Fluid Dynamic (CFD) for the H-D exchange reaction. In the upper figure the calculated gas flow is seen whereas the middle figure shows the H-D pressure and bottom figure shows the D_2 pressure. The model uses a surface temperature of 100^oC and a spot size of 1 mm and the temperature of the nozzle are set to 72.5^oC. The gas composition is 1% D_2 in H_2 with a gas flow of 100 ml/min and the distance between the aluminum nozzle and the surface is 0.2 mm in the calculation. Experimentally the distance between the surface and the aluminum nozzle is determined by bringing the two in electrical contact and retracting the nozzle 0.2 mm controlled by stepper motors. Furthermore, the argon signal is traced while retracting the nozzle which gives an indication of the leak through the capillary.

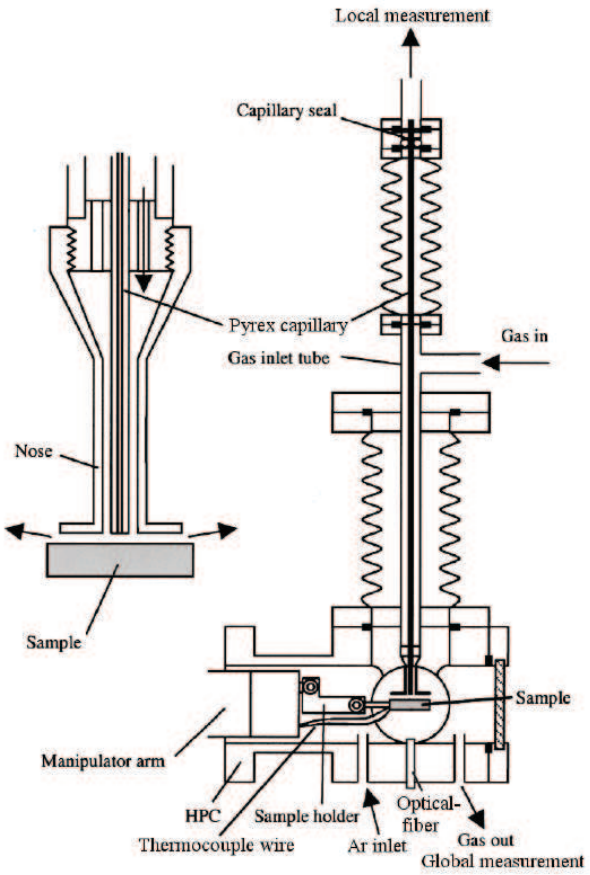

Figure 2.8: The figure shows a drawing of a gas sampling device similar to the parallel screening. A zoom of the aluminum nozzle and capillary tube is further seen.

The calculations in the three figures in fig. 2.9 show how the spillover effect is not present in the catalytic testing in the high pressure cell. The gas flows away from the catalytic spots and H-D exchange reaction only occurs underneath the capillary as the H-D is higher and D_2 pressure is lower. The working distance between the aluminum nozzle and the sample surface ensures a uniform circular flow of high velocity around the catalytic spots exceeding 2 m/s. The uniform flow works as a barrier inhibiting back diffusion of reaction products from neighboring spots and the capillary therefore only measures the gas composition of the desired spot.

When the sample is heated, the pressure in the tube decreases, and consequently the signal in the QMS also decreases. Two effects are present when the temperature is increased namely the diffusion and density of the gas. As the pocket of gas between the nozzle

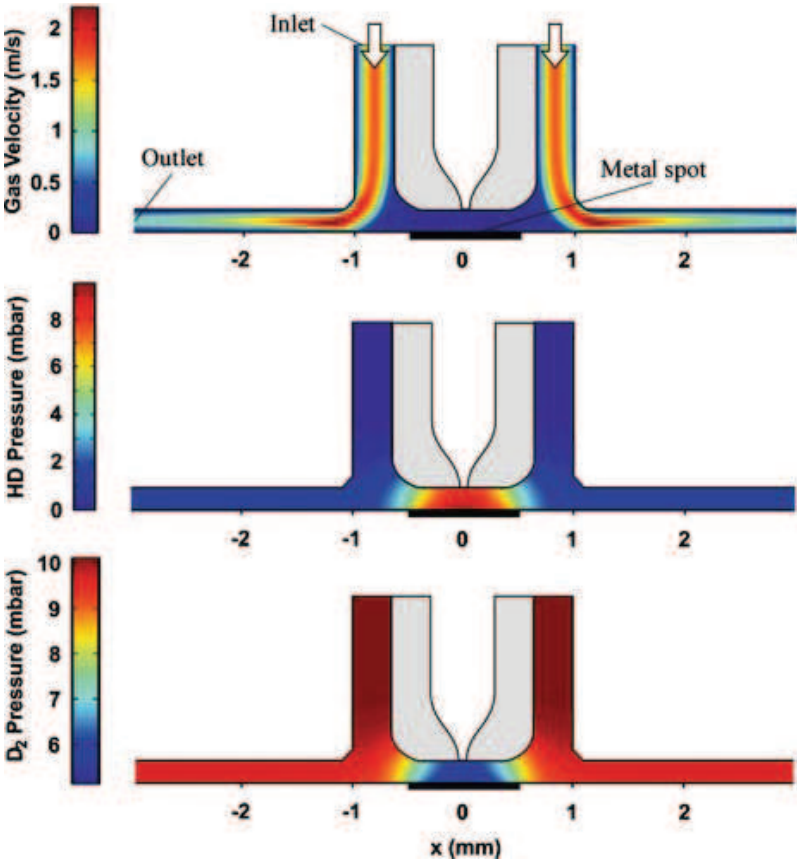

Figure 2.9: The figure shows a simulation made on the flow between the sniffer and sample. Alignment ensures a uniform flow and no spillover from neighboring spots. Adapted from [16][17]

and the sample is heated the diffusion speed of the gas increases which should increase the pressure and hereby the QMS signal. At the same time the density of the gas in the pocket decreases as consequence of increased temperature. To account for these effects the QMS signals are always normalized to the argon signal which is always present in the gas mixtures used in the high pressure experiments.

2.3.2 Gas supply system

The Parallel Screening setup has a dedicated gas system. The gas system supplies argon for the sputter gun, argon and helium for the ion gun, and CO and O_2 for leak valves. Furthermore, the gas system is equipped with four flow controllers for reactant gases for experiments in the high pressure cell. Here, CO, CO/He, He, O_2/Ar, NH_3/Ar and H_2 are the primary gases used, all of 6.0 purity except CO which is 4.7. The gas system has separate roughing- and turbo pumps for evacuation.

2.4 Heating the sample

For all catalytic testing the temperature of the catalyst is crucial. A rule of thumb is the activity of a catalyst increases exponentially as function of temperature. Therefore it is of highest importance that there are no heating gradients across the TiO_2 sample if the desire is to compare different catalysts. This is precisely the strength of the parallel screening setup, testing multiple catalytic spots in the same experiment and comparing them relative to each other.
To make sure the heat is evenly distributed in the TiO_2 crystal, two different tests are made. In the first test the gas sampling device is removed from the HPC. Instead a 2 inch germanium wafer is placed on top of the HPC and sealed with a rubber gasket, seen in fig. 2.10(b).

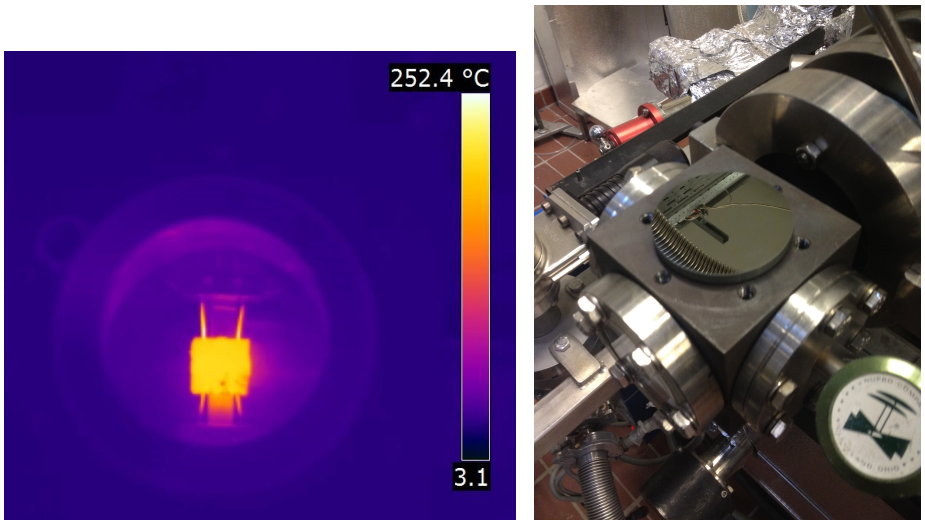

(a) (b)

Figure 2.10: Figure a: The figure shows a thermographic image of the sample heated to 600 K. The scale bar is not calibrated. Figure b: The picture shows the HPC with the germanium wafer placed on top. Notice the wafer is not transparent to visible light.

The germanium wafer is transparent to IR but not visible light. This makes it possible to record thermographic image measuring the heat radiation from the sample. The HPC is filled with 0.9 bar Ar to mimic the testing conditions and the temperature of sample increased. In fig. 2.10(a) a thermographic image of the sample heated to 600 K is seen. The absolute temperature of the camera is not calibrated and this is only an indication of the heat distribution of the sample.
The heat distribution of the sample appears quiet even. However, a closer look of the image in high resolution reveals that the bottom part of the sample is slightly warmer. Furthermore, the W-filaments suspending the samples appears to saturate on the un-

calibrated scale bar indicating they are warmer than the sample. However, the pictures are not conclusive and should only be seen as an indication of the heat distribution of the sample visually.

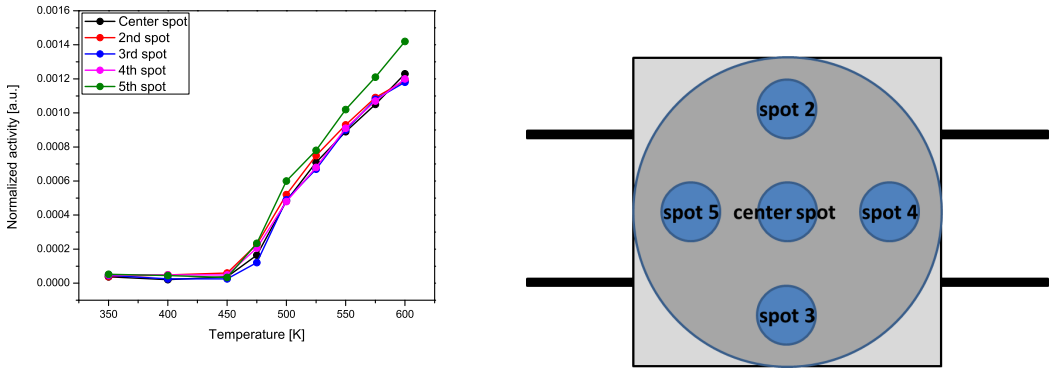

(a) (b)

Figure 2.11: Fig. a shows the activity of five identical 50 Å Pt spots as function of temperature towards ammonia oxidation. Fig. b shows a drawing of the position of the five spots on the TiO_2 crystal.

The second experiment that is performed in order to determine the heat dispersion on the TiO_2 is a catalytic experiment where five identical spots are evaporated in a cross, see fig. 2.11(b). A catalytic measurement of ammonia oxidation is made in the HPC at 1 bar. For each of the spots the temperature is increased and the measured evolution in N_2 is taken as a sign of catalytic activity. If the temperature is evenly dispersed on the sample, the catalytic activity is expected to be equal on all spots. However, as seen in fig. 2.11(a) only four of the spots seem to have the same tendency, indicating spot 5 having a higher temperature than the rest.
This coincides with the fact that this spot appeared warmer in the thermographic images. Throughout the work this particular spot is not used in experiments and the temperature is assumed to be similar in all the positions used for experiments.

2.5 Automation of the setup

During the Ph.D. project much time was spent optimizing, maintaining and improving the setup. The mass spectrometer in the analysis chamber has been added to the setup on a linear motion with a copper sniffer. Furthermore, the temperature is changed from being controlled by a Eurotherm to being controlled and logged by a LabView program. The temperature data of the sample is directly saved in the CINF database accessible for employees with internet connection. The combination of data logging of the temperature and QMS data enables the setup of doing TPD measurements.

The pressure of the setup is also logged on the CINF database so the pressure can be monitored during bakeouts etc.
The mass spectrometer measuring on the HPC has been linked with the movement of the gas sampling device which means the QMS traces the gases as well as the sniffer position and temperature of the sample. Furthermore, a new substrate has been implemented. Finally, a new sample holder for XPS measurements on powder catalysts has been designed. The many improvements made to the setup has cost a lot of time. However, the operation time of the setup has been increased. Many of the function of the setup can furthermore be controlled by any computer with internet connection if allowed access. This means many of the measurements have been conducted in the evening and night, controlled with a laptop from home.

Chapter 3

CO desorption from single crystal and nanoparticulate Ru

In this chapter the project involving CO desorption from ruthenium surfaces will be presented. Especially the influence of the structure on the catalytic abilities will be discussed. Model systems of single crystal ruthenium and ruthenium nanoparticles are investigated by probing the correlation between the systems for CO dissociation and desorption. The project was part of a collaboration between three UHV setups at CINF each providing results for the study.
The chapter will contain an introduction to the field of CO adsorption on ruthenium covering a motivation of the study followed by a summary of literature on the subject. Then the experimental results obtain at CINF will be presented and the importance of the structure of ruthenium for reactivity will be discussed.

3.1 Introduction

CO desorption from transition metal surfaces is studied thoroughly throughout literature. CO is an excellent molecule for testing surfaces through adsorption and desorption due to the size, stability and chemistry. Furthermore, CO is an industrial important molecule for synthesizing hydrocarbons as in the Fischer-Tropsch process. The dissociation of CO, eq. 3.1, is a very simple reaction but of highest importance as it is the rate limiting step in important industrial catalytic reactions as the Fischer-Tropsch process (eq. 3.2) and the methanation reaction (eq. 3.3).

$$\mathrm{CO} \rightarrow \mathrm{C} + \mathrm{O} \tag{3.1}$$

$$(2n+1)\mathrm{H_2} + n\mathrm{CO} = \rightarrow \mathrm{C}_n\mathrm{H}_{2n+2} + n\mathrm{H_2O} \tag{3.2}$$

$$\mathrm{CO} + 3\mathrm{H_2} \rightarrow \mathrm{CH_4} + \mathrm{H_2O} \tag{3.3}$$

The Fischer-Tropsch process involves the formation of higher hydrocarbons for fuels such as gasoline and diesel and can be formed from lighter hydrocarbons such as methane through steam reforming or from gasification of coal. The production of synthetic fuels may play an important role in the future as the fossil fuels are running low, sec. 1.2. Synthetic fuels have the potential of becoming an important factor in the transportation sector in the near future [18].
Studying CO dissociation is not only interesting because of the importance for industrial relevant reactions but also from a fundamental research point of view. The simple nature of the CO molecule makes it ideal for finding the nature of the reactivity. Ruthenium which is studied in this chapter is a too expensive and to scarce material for large scale implementation for any of these catalytic reactions. However, ruthenium is one of the most active catalysts for dissociation of CO. Hopefully, by studying the mechanism and structure dependence of CO dissociation on ruthenium it is possible to develop new and better catalysts from cheaper materials.
The relevance of probing the CO dissociation on ruthenium and the structure of CO adsorbed on ruthenium surfaces has been studied extensively in literature and the next section will serve as an summary of this.

3.1.1 The structure of ruthenium and CO

Ruthenium has a closed packed hpc structure with the (0001) facet as the most stable surface. CO adsorbs in different structures on the Ru(0001) surface with CO binding through the carbon atom perpendicular to the surface. CO forms a $(\sqrt{3} \times \sqrt{3})$R30° structure for surface coverage up to 1/3 ML on a top site on the (0001) facet [19–21]. For coverage extending 1/3 of a monolayer the CO binds weakly to the surface and forms a distorted overlayer on the $(\sqrt{3} \times \sqrt{3})$R30° structure with large repulsion in between the CO molecules. This structure is formed until the ruthenium surface is saturated with CO at a coverage of 0.58 ML for the (0001) surface [19][21]. The $(\sqrt{3} \times \sqrt{3})$R30° structure has primarily been observed with LEED and STM [22][23]. For a CO coverage extending 1/3 ML the structure is difficult to resolve due to the weak interaction between CO and the surface.
The importance of the structure of ruthenium for the catalytic performance has been much debated. The core of the discussion lies within whether a reaction such as the methanation process is structure sensitive or insensitive. Measurements of the activity for methane production per surface site for nickel single crystals of different orientations concluded the methanation reaction to be structure insensitive [24][25]. The study was further expanded to ruthenium concluding the methanation reaction being structure insensitive on ruthenium as well.
Combined theoretical and experimental studies later contradictory proved the methanation reaction to be structure sensitive on nickel [26]. By deliberately poisoning the steps sites of the nickel single crystal with sulfur the dissociation of CO was completely suppressed and hereby also the activity. This raised the question whether the methanation reaction

was structure sensitive contradictory to the findings of Goodman *et al.* A thorough investigation by Zubkov *et al.* reported a study of the CO dissociation on a stepped Ru(1 0 9) single crystal. In fig. 3.1(a) various CO TPDs are seen for different CO coverage on a Ru(1 0 9) single crystal. In the figure it is seen that CO preferentially adsorbs in the two high temperature features denoted by α and β. The saturation coverage of the single crystal is 0.54 ML slightly lower than the 0.58 ML for the atomically flat Ru(0001) surface. As the α and β features reach the saturation limit CO is adsorbed in a new site resulting in a shoulder feature at lower desorption temperature.

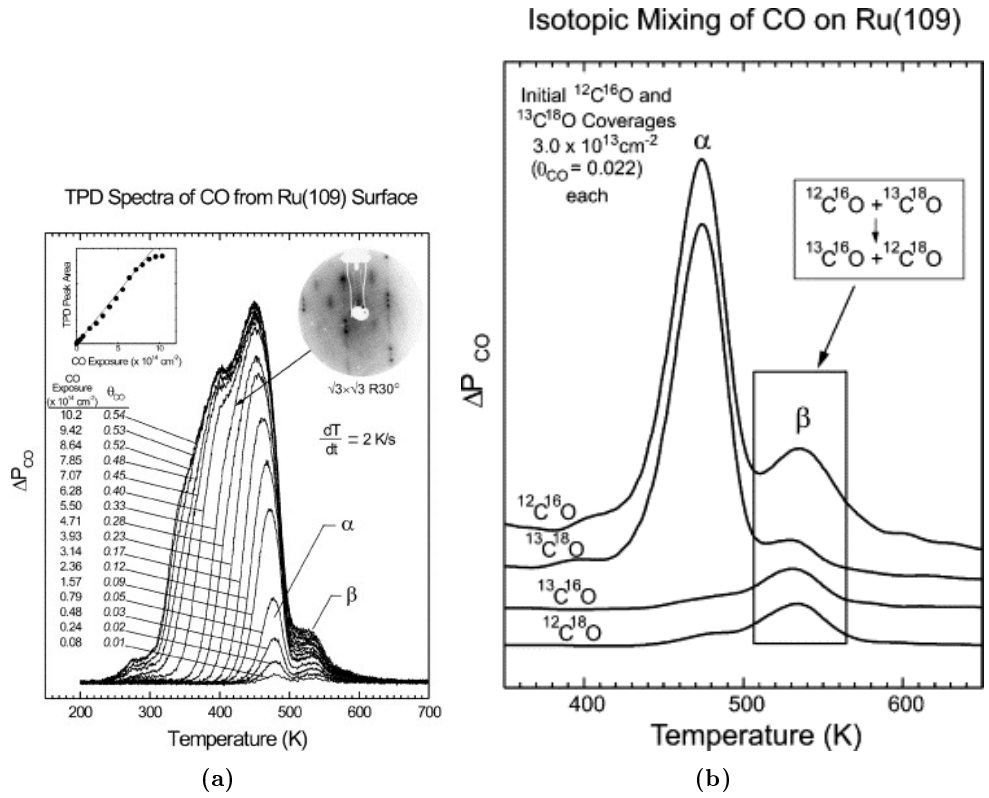

Figure 3.1: Figure A shows several CO TPDs for varying CO coverage on a Ru(1 0 9) single crystal and figure B a isotopic labeled CO scrambling experiment on the same single crystal. The figures are adapted from [27].

Zubkov *et al.* conducted a scrambling experiment by adsorbing isotopic labeled CO of mass 28 and mass 31 corresponding to $C^{12}O^{16}$ and $C^{13}O^{18}$. In fig. 3.1(b) the measured signals of atomic mass unit 28, 29, 30 and 31 are seen. It is important to notice that scrambling only occurs at temperature corresponding to the β peak of the TPD. Since the β peak originates from CO desorption from the step sites it is concluded that CO dissociation occurs on the step sites of the ruthenium single crystal. It has further been shown that the dissociation can be blocked by decomposition of ethylene to form carbon on the step

sites.
The conflict whether CO dissociation on ruthenium is structure sensitive or insensitive is not completely clarified. It is suggested that the undercoordinated steps sites are so reactive and superior that if they are present they will completely dominate the activity and make the surface appear as structure insensitive [26][28][29]. Ruthenium has shown to be extremely structure sensitive for other reactions than for dissociating CO. S. Dahl *et al.* demonstrated that the step sites are more than nine orders of magnitude more active for N_2 dissociation, recombination and desorption than the terrace sites on a Ru(001) single crystal. DFT calculations have revealed that a special site, referred to as the B5 site, exhibits significantly higher activity than the terrace sites [30].
The purpose of this study is to investigate the desorption from a ruthenium single crystal containing 4% step in terms of primarily CO TPDs. Indications of the importance of the steps for dissociation of CO are given. Furthermore, the single crystal experiments will be compared to experiments of size selected nanoparticles.

3.2 CO desorption from single crystal Ru(0 1 54)

In this section CO desorption from single crystal ruthenium will be presented. The model system used for investigation of CO desorption from ruthenium is a single crystal cut in the (0 1 54) direction. The single crystal is provided my Mateck GmbH, and consists of closed packed terraces of (0001) facets and 4 % steps sites which appear in two alternating types, A and B. The terraces are in average 27 atoms long ($\sim$ 6.3 nm) separated by mono-atomic steps. The undercoordinated step sites are characterized by having either a 3- or 4 fold symmetry as indicated in fig. 3.2 where a ball model of the used Ru(0 1 54) single crystal is shown.

STM images of an identical ruthenium single crystal have shown the average width of the terraces to be between 4 and 10 nm [23]. The STM study further concludes that the crystal in fact only contains monoatomic steps and that the steps do not reconstruct as reported for ruthenium single crystals with a higher step density [22].

3.2.1 Cleaning the ruthenium single crystal

Due to the reactivity of ruthenium, cleaning the surface is not trivial. To ensure a clean surface before experiments the following procedure has been tested and optimized [31]. The ruthenium crystal is first sputtered with 1 keV argon ions at 10^{-5} Torr for 30 minutes at 800 K to remove surface contaminants such as nickel or sulfur depending on previous experiments. The surface is then oxidized with 10^{-7} Torr for 10 minutes at 1100 K to burn residual carbon of the surface. Due to current limitations of the feedthrough the remaining oxygen is reacted off the surface by introducing 10^{-6} Torr hydrogen at 500 K

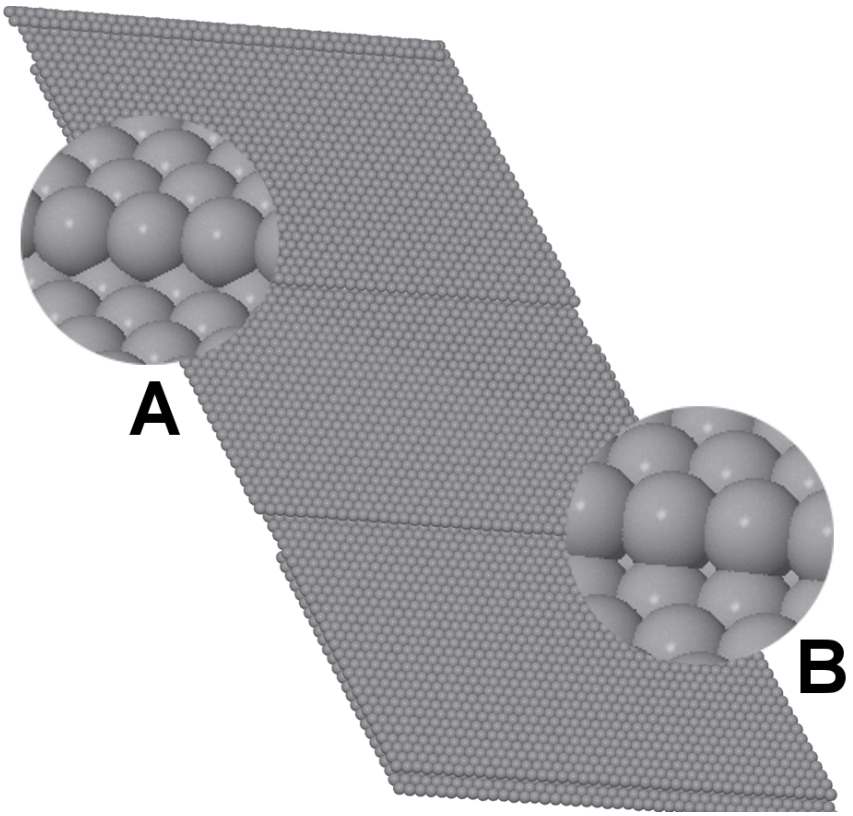

Figure 3.2: The figure shows a ball model of the Ru(0 1 54) single crystal surface. The terraces consist large (0001) facets and the steps switch from having a three or four fold symmetry. The figure is adapted from [23]

for 30 minutes as oxygen desorbs from ruthenium between 1100 K and 1700 K which is above the maximum temperature [32]. Finally, the ruthenium crystal is flash annealed to 1200 K for 1 minute.
The ruthenium surface is afterwards checked with AES for contaminants and CO-TPD resembles studies from literature of clean surfaces [27][33]. The experiments confirm that the ruthenium surface is in fact clean.

3.2.2 CO desorption

As seen in the introduction, CO desorption from ruthenium surface is widely studied in the literature. A CO TPD from the ruthenium (1 0 54) single crystal is obtained by dosing 10 L of CO in UHV to ensure a full coverage of the ruthenium surface corresponding to a 100 sec dose at $p_{CO}=10^{-7}$ Torr. In fig. 3.3 a typical CO TPD is seen from the Ru(1 0 54) single crystal heated by 2 K/sec. The CO-TPD has three distinct features marked by α and β. The β-peak positioned at 500-550 K corresponds to CO desorbing from step

sites whereas the high temperature α-peak at 460 K is related to CO desorption from the (0001) terraces and the low temperature α-peak corresponds to CO squeezed in the CO terraces decoration. The CO binds to the terraces in an upright position binding to the surface through the carbon atom and forms a beautiful $(\sqrt{3} \times \sqrt{3})$R30° structure observed by both LEED and STM [22][23].

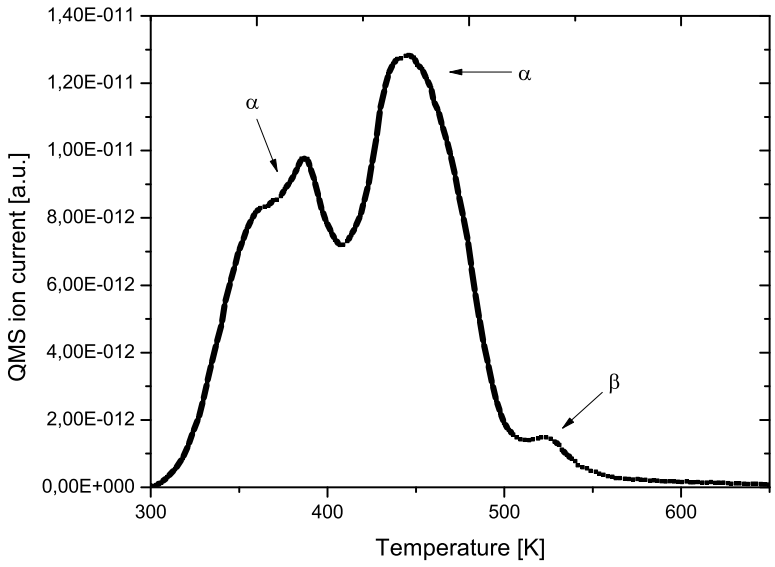

Figure 3.3: CO TPD from a Ru(1 0 54) surface. The CO TPD has three distinct features, a high and low temperature α-peak and high temperature shoulder feature referred to as the β-peak.

The size of the β-peak and hereby the amount of steps can be quantified by subtracting an exponentially decaying background to the right side of the high temperature α-peak. For a cleaned single crystal the area of the β-peak corresponds to the expected 4% of the surface.
The CO TPD shown in fig. 3.3 has similarities to the CO TPD reported on the Ru(1 0 9) single crystal by Zubkov *et al.* in fig. 3.1(a). The positions of the high temperature α-peak and the β-peak are the same. The position and form of the high temperature α-peak indicates that the $(\sqrt{3} \times \sqrt{3})$R30° CO structure is present on the Ru(1 0 54) single crystal as well. The low temperature α-peak is not as pronounced on the Ru(1 0 9) single crystal due to the higher step density. The average size of the terraces is narrower on the Ru (1 0 9) single crystal reducing the weak overlayer squeezing for CO on the $(\sqrt{3} \times \sqrt{3})$R30° structure.

In fig. 3.4 CO TPD experiments for varying coverage are seen. The surface saturates at a

coverage corresponding to 0.54 ML determined by [22]. For low coverage the CO desorbs partially from the high temperature α peak and the β-peak corresponding to the terrace and step sites on the ruthenium single crystal. As the coverage increases the terraces and step sites are fully covered and a $(\sqrt{3} \times \sqrt{3})$R30° structure is obtain at around 0.31 ML. The structure is distorted by the low temperature α peak where CO is squeezed into the CO structure on the terraces.

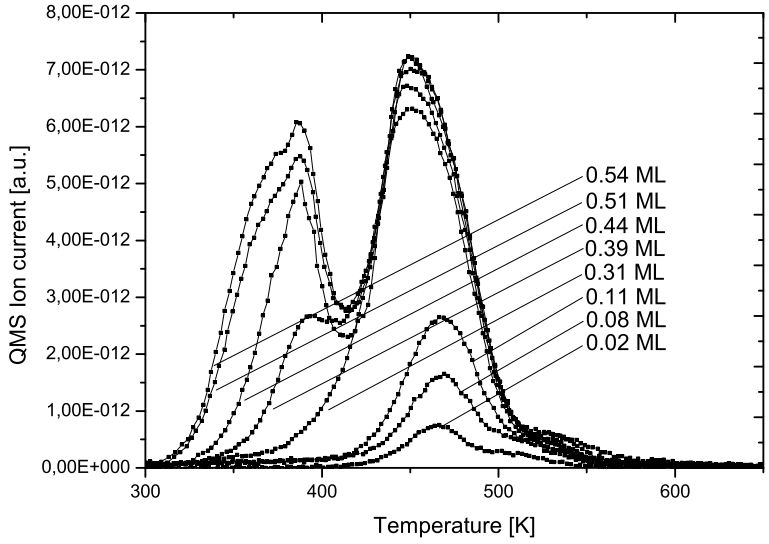

Figure 3.4: CO desorption from a single crystal ruthenium surface ranging from 0.02 ML to full coverage corresponding to 0.54 ML. The figure clearly shows CO is adsorbed at the terraces and step sites before finally squeezing CO in $(\sqrt{3} \times \sqrt{3})$R30° structure on the terraces.

The low CO coverage on the Ru(1 0 54) single crystal follows the same trends as reported by [22] in fig. 3.1(a).

The single crystal surface is further investigated by sputtering of the surface prior to CO adsorption. In fig. 3.5 a CO TPD from a sputtered ruthenium single crystal is shown. The characteristic features of CO desorbing from the (0001) terraces is significantly changed by sputtering the surface prior to CO adsorption. The sputtered surface only exhibits a single desorption peak at approximately 430 K and a much larger shoulder. The sputtering of the single crystal is expected to induce defects to the surface increasing the number of undercoordinated sites.

From the CO TPD on the clean ruthenium surface it is known that the low temperature

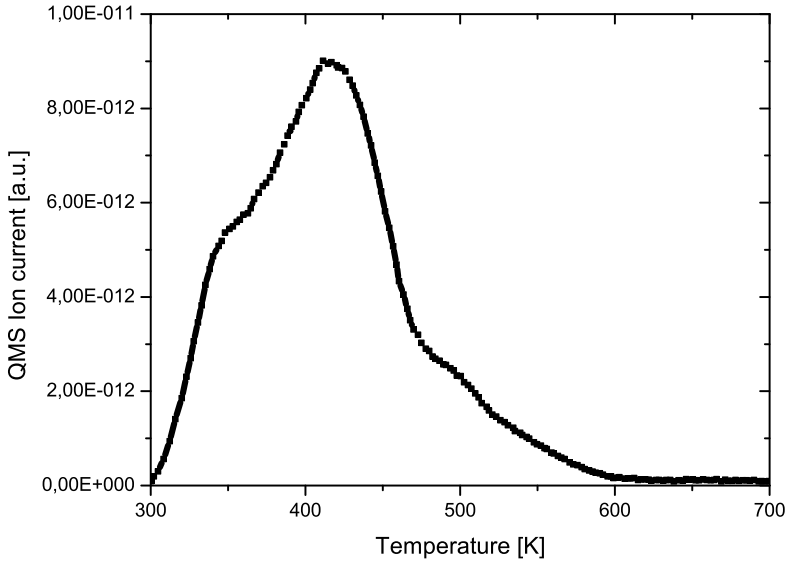

Figure 3.5: CO TPD from a sputtered surface Ru single crystal.

α peak originates from CO squeezing in between CO on the flat terraces. As defects are induced to the terraces the same periodic structure is not obtained and hence a double peak in the TPD spectra is not expected. If the sputtered single crystal is annealed after the CO TPD and a new CO TPD is performed directly after the annealing the CO TPD is similar to a CO TPD of a (0001) surface.
Comparing the area under the curve of the TPD of the clean ruthenium surface to area under the curve of the defect induced sputtered surface, the area of the sputter surface is substantially smaller. This is counterintuitive as a flat surface should have the lowest possible specific surface area. However, CO is bound to the step on upright position. If CO binds in a tilted configuration on the undercoordinated sites CO can block some sites with the dipole moment causing less CO to adsorb. Another scenario is that sites where CO adsorbs and desorbs below room temperature are induced by sputtering. These sites are therefore not probed with the TPD experiments in the current configuration.

3.2.3 Step sites and defects of CO dissociation

The step sites have proven to be superior compared to the terraces site for dissociation of CO and N_2. The performance of the steps and the sputtered surface are investigated compared to the clean and atomically flat surface. In fig. 3.6 an experiment conducted by S. Vendelbo is shown. The deposition of carbon on the surface is measured as function of dose time in both UHV and at high pressure where CO is dosed at 10^{-5} Torr and 0.1 bar

respectively. The CO is dosed at 550 K which is known to be the dissociation temperature. After dosing CO, a CO TPD is performed and the carbon deposited on the surface is measured by oxygen titration.

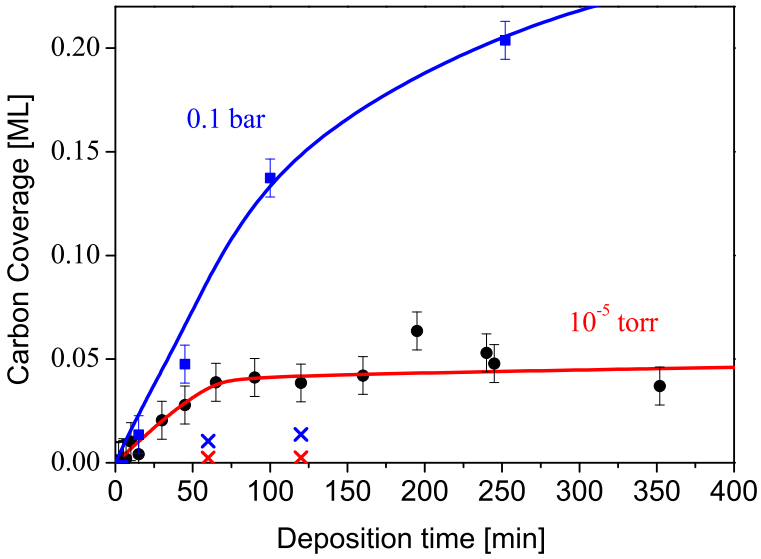

Figure 3.6: The carbon uptake measured by oxygen titration as function of deposition time. CO is dosed at 10^{-5} Torr in UHV (red line) and 0.1 bar in the HPC (blue line) at 550 K. The figure is adapted from [34]. Four points are further added and represents an experiment where the step site are blocked by sulfur prior to dosing CO.

In fig. 3.6 the red line represents dosing CO in UHV and the blue line corresponds to dosing CO in the HPC. The deposition of carbon, measured by oxygen titration, on the surface is a measure of the dissociated CO. When CO dissociates the mobile oxygen atom is able to migrate from the step onto the terrace and react with another adsorbed CO molecule and form CO_2 which immediately desorbs at 550 K. The dissociated carbon atom is left bound to the step, blocking the step site for any further CO dissociation. The CO deposited in UHV increases to roughly 0.04 ML where the carbon deposition saturates. The blue curve corresponds to 0.1 bar CO, and is seen to increase without saturating within the time scale. Furthermore, the experiment is repeated where 0.04 ML sulfur is deposited on the single crystal prior to the CO dosage. Data from these experiments are marked by crosses in fig. 3.6. In literature low coverage of sulfur on ruthenium is reported to migrate to defect sites [35]. For the low pressure CO dosing the carbon deposition is completely suppressed whereas for the high pressure dosing the carbon deposition is drastically but not completely suppressed. The figure tells that carbon blocks the steps from further CO dissociation at a temperature of 550 K for low pressures CO dosing, while at higher pressures carbon

continues to form and covers the terrace. The experiment indicates the importance of the step for dissociating CO. As the steps are covered by carbon any further dissociation is suppressed and no further carbon is deposited.
For all experiments involving high pressure of CO the surface is always investigated for contamination of nickel.

S. Vendelbo further investigated the importance of the step sites for methane production. The clean Ru(1 0 54) single crystal is covered with varying amounts of sulfur and subsequent exposed to 1:100 CO:H_2 at 1 bar in the HPC. The amount of sulfur added is calibrated with AES. In fig. 3.7 the methane production as function of sulfur coverage is seen. A data point is added to the work of S. Vendelbo, namely the methane production of the ruthenium single crystal sputtered for 5 min corresponding to the treatment in fig. 3.5. The added point is marked by a blue cross in the figure. The sputtering of the single crystal is expected to induce defect sites to the surface.

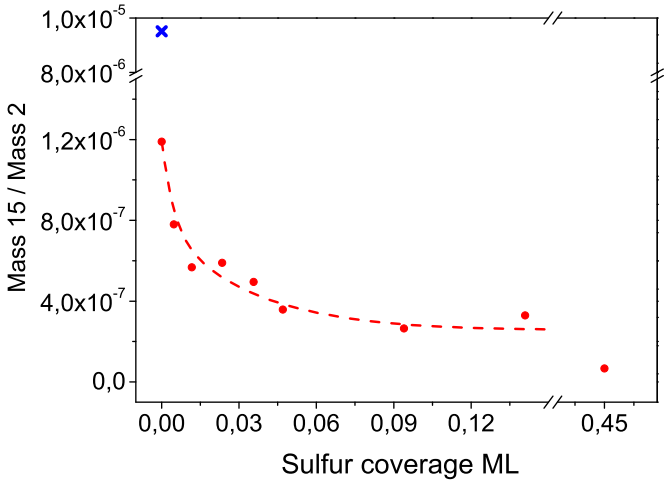

Figure 3.7: The figure shows the methane production of the Ru(1 0 54) single crystal. Increasing amount of sulfur is added to the step sites suppressing the methane production. The figure is adapted from [28] with a single point added marked by a blue cross.

The methane production on the ruthenium single crystal is clearly suppressed by adding sulfur to the step sites. The minimum value of the methane production is reached by adding just 0.4 ML of sulfur to the surface. Contrarily, the activity towards the methane production becomes 8 times higher by sputtering the single crystal prior to the experiment. The fact that sulfur suppresses the methane production indicates that the rate limiting

step for CO dissociation is the undercoordinated site. Equally, the sputtered surface is expected to contain a number of undercoordinated defect sites. The sputtered surface exhibits higher activity indicating a structure sensitivity of the methanation reaction.

3.3 CO desorption from nanoparticle Ru

The second model studied for CO desorption on ruthenium is size selected nanoparticles. Industrial catalysts are typically more complex in nature than the single crystal surfaces encountered in many surface science studies. A better representation of the industrial catalyst can be obtained by studying an ensemble of nanoparticles supported on a well-defined planar substrate. The CO desorption experiments on ruthenium nanoparticles are conducted by C. Strebel *et al.* at CINF. In fig. 3.8 CO TPD on four different sizes of size selected ruthenium nanoparticles are shown. The nanoparticles are produced from a magnetron sputter source and sized selected by a Quadropole Mass Filter (QMF) before deposited onto a HOPG substrates at room temperature. The size of the nanoparticles in fig. 3.8 is determined by Transmission Electron Microscopy to be 2.8, 5.9, 11.0 and 15.2 nm with a standard deviation of 0.5, 0.8, 1.0 and 2.0 nm respectively. The TPD signal is divided into molecular and dissociative desorption as labeled CO is used for the experiment. For the experiment $C^{13}O^{16}$ and $C^{12}O^{18}$ are dosed which means that if scrambling occurs four products can be measured namely, CO with atomic mass unit of 28, 29, 30 and 31. Assuming an equal probability of scrambling into all four products, the scrambling measured as the amount of desorbed $C^{13}O^{18}$ is assigned to 1/4 of the total scrambling. The total amount of the scrambled signal and representing the dissociative desorption in fig. 3.8 is therefore 4 times the measured signal of $C^{13}O^{18}$. The same principle counts for $C^{12}O^{16}$ but is not used due to a high background in the mass spectrometer.

All four CO TPDs are to some degree similar. However, the amount of CO scrambling and hereby dissociation is different for the four sizes of nanoparticles. The maximum scrambling is measured for the 11.0 nm nanoparticles where the scrambled signal accounts for 25% of the total desorbed CO. The CO scrambling experiments presented in fig. 3.8 demonstrate that the molecular adsorbed CO desorb in a temperature range from 300 K to 450 K. This is similar to the sputtered ruthenium single crystal fig. 3.8. The CO dissociates at several types of under-coordinated surface sites followed by recombination and desorption at temperatures between 400 K and 600 K, as seen by the green line.
DFT calculations suggest the optimal size of the nanoparticles for N_2 dissociation in their equilibrium shape to be 3 nm [37] contrary to fig. 3.8. The reason for the deviation in the optimal size of the nanoparticles is presumable that the nanoparticles are not in equilibrium shape when deposited on the support. This suggests that if such undercoordinated sites can be made stable, highly active catalysts can be made by tailoring nanoparticles with highly undercoordinated sites for reactions involving CO and N_2 dissociation.

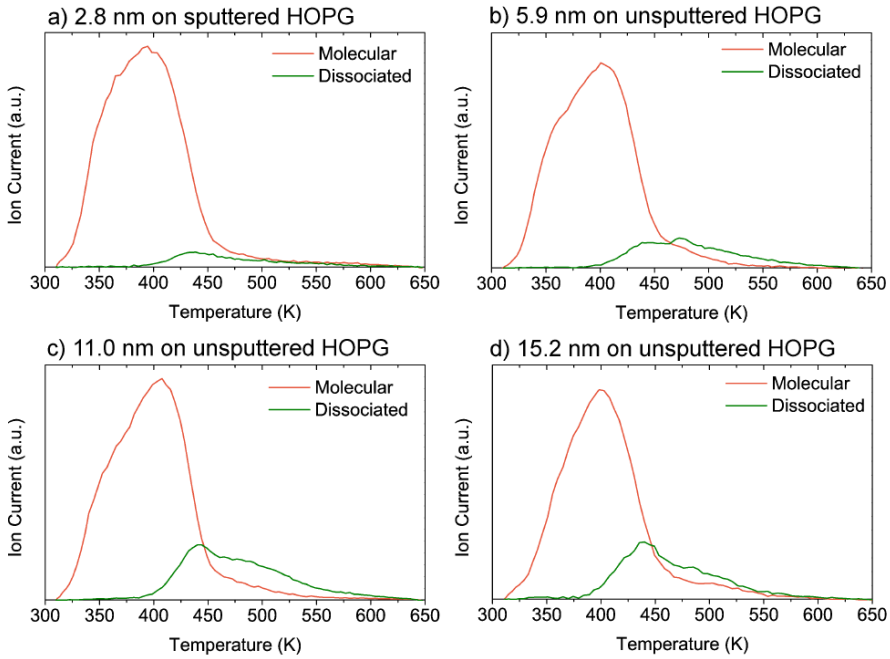

Figure 3.8: The figure shows the CO TPD from four different sizes of size selected ruthenium nanoparticles supported on sputtered HOPG. The figure is adapted from [36].

3.4 Crossover in CO desorption from single crystal to nanoparticles

CO desorption from a ruthenium single crystal and from size selected nanoparticles have in the previous sections been presented. In an effort to investigate the gap between single crystals and supported nanoparticles, the CO desorption properties of the HOPG supported Ru nanoparticles will be compared to that of a Ru single crystal previously presented. CO desorption is used to follow the gradual change from single crystal like behavior to nanoparticle like behavior and vice versa.

In fig. 3.9 STM images of a clean ruthenium single crystal surface and a single crystal ruthenium surface sputtered for 5 min are seen. Furthermore, the TPD profiles for the two cases are shown in fig. 3.9C together with intermediate structures for sputter time in between the two STM images. The non-sputtered ruthenium surface is characterized by terraces with a width varying between 4 nm and 10 nm as expected from fig. 3.2 with an average terrace width of 6.5 nm corresponding to 27 atoms. The terraces are separated by straight monatomic steps with a measured height comparable to the theoretical distance between the (0001) planes.
In contradiction, the sputtered ruthenium single crystal displays a surface with a high

degree of roughness where small islands are evident on the terraces. The small islands are expected to be formed as a consequence of a surface restructuring due to the sputtering process.

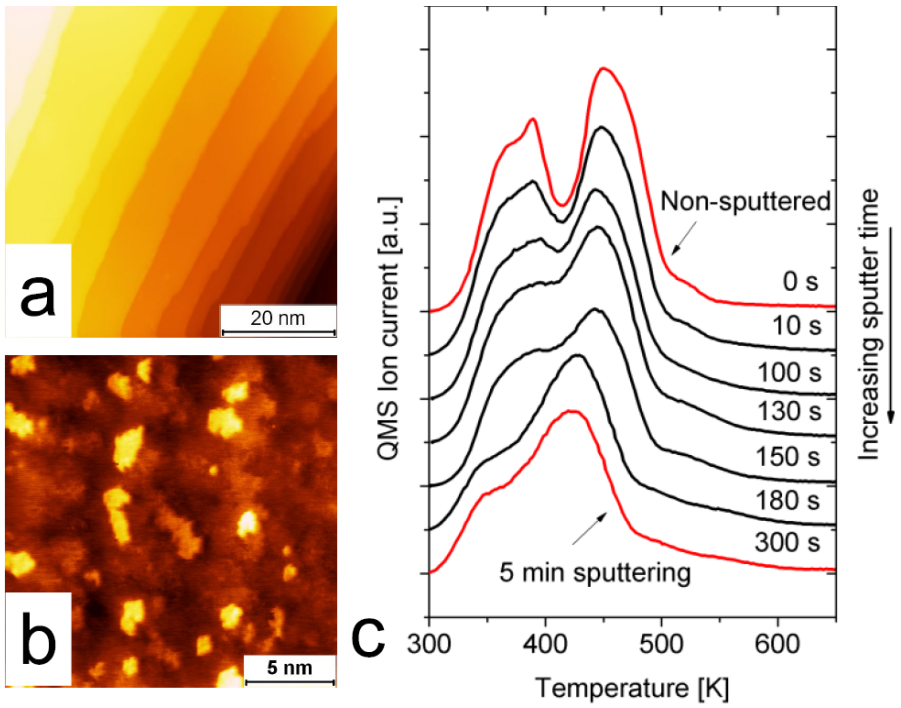

Figure 3.9: Figure A shows an STM image of a clean non sputtered ruthenium single crystal surface. Figure B is a STM image of the sputtered ruthenium surface while figure C shows CO-TPDs varying from a clean single crystal to a sputtered surface. The STM images is made by Y. Tison and the figure is adapted from [38]

A sequence of CO desorption spectra are obtained from the Ru(0 1 54) surface after different periods of sputtering with 1 keV Ar^+ ions at room temperature. The CO desorption spectra are seen in fig. 3.9C for the non-sputtered surface to the 5 min sputtered surface. The non-sputtered surface exhibits two clear distinctive desorption peaks located at 390 K and 460 K that are characteristic of CO desorption from (0001) terraces corresponding to the α-peaks in fig. 3.3. Furthermore, a desorption feature is seen at 535 K corresponding to the dissociative adsorption at step sites. However, with increased surface sputtering a gradual transition is observed between the double-peak spectrum towards a single broad feature centered around 420 K. The desorption feature seen at 390 K on the non-sputtered surface gradually disappears with increased sputtering time until it is no more than a shoulder on the low-temperature side of the main desorption feature seen for the 5 min sputtered surface. In addition, the peak at 460 K on the non-sputtered surface gradually shifts down in temperature with increased sputtering time until the feature is located around 420 K. It should be pointed out that the STM and TPD data of the Ru(0

1 54) surface presented here are obtained in two different UHV systems. In both cases the cleanliness of the surface before and after sputtering is confirmed by XPS in the case of the STM measurements, and by AES and oxygen titration measurements in the case of the TPD experiments. This ensures that a contamination level below 1% is obtained. CO TPD measurements are also performed in the STM system and yields qualitatively similar results to those presented here.

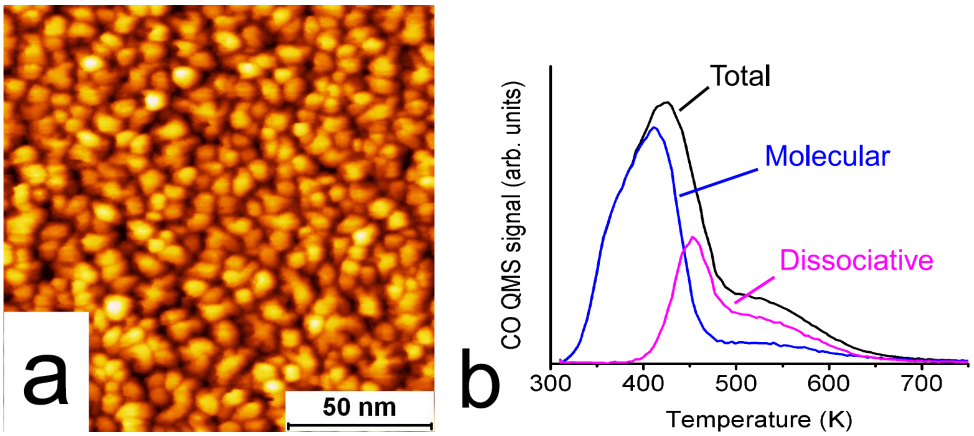

(a) (b)

Figure 3.10: Figure A is a STM image of the PVD nanoparticles as deposited. Figure B shows an isotopic labeled CO TPD experiment distinguishing the molecular and dissociative desorption.

In addition to the presented mass-selected nanoparticles in sec. 3.3 a film of 50 Å ruthenium is deposited by PVD on HOPG.
The morphology of the PVD nanoparticles is investigated for thinfilms of 0.5 Å to 2 Å of thickness. The nanoparticles deposited by PVD display a bimodal growth with small round nanoparticles decorating the substrate step edges whereas larger flat nanoparticles are formed on the terraces [39]. The mean diameter of the PVD nanoparticles varies between 3-5.5 nm and their mean height is approximately 1 nm. The standard deviation of the measured size distributions is of the order of 30% of the size of the particles. Room temperature deposition of Ru results in the formation of small round nanoparticles with a narrow size distribution.
The CO desorption behavior of the thick 50 Å PVD-grown Ru film has been investigated. In fig. 3.10(a) a STM image of 50 Å thick Ru film deposited on as-cleaved HOPG at room temperature is shown. The surface morphology of the film consists of nanoparticles with a mean diameter of 6±2 nm. The substrate cannot be seen with STM as the film is several layers thick. The CO TPD corresponding to the nanoparticle thinfilm is seen in fig. 3.10(b) and exhibits a single broad desorption feature centered at 420 K and a broader shoulder from 500-600 K.

In fig. 3.11(a) a STM image of the PVD 50 Å film of ruthenium nanoparticles annealed to 900 K for 10 min is shown. The STM image is significantly different from the STM images of the as the deposited nanoparticles. The annealed film of nanoparticles appears to be polycrystalline with plateaus of flat terraces separated by monoatomic steps.
In fig. 3.11(b) the CO TPD representing the annealed film of ruthenium nanoparticles is shown. The CO TPD has two characteristic desorption peaks at 390 and 450 K and a smaller desorption feature at 530 K. The CO desorption is divided into molecular and dissociative desorption as explained in sec. 3.3. The profile of the CO TPD fits well with the typical desorption spectrum of a flat ruthenium (0001) facet similar to fig. 3.3. The two characteristic desorption peaks can be assigned to desorption of molecularly adsorbed CO from the terraces referred to as the α-peak, while the smaller desorption feature at 530 K can be assigned to the β-peak and hence the desorption of dissociatively adsorbed CO from step sites.

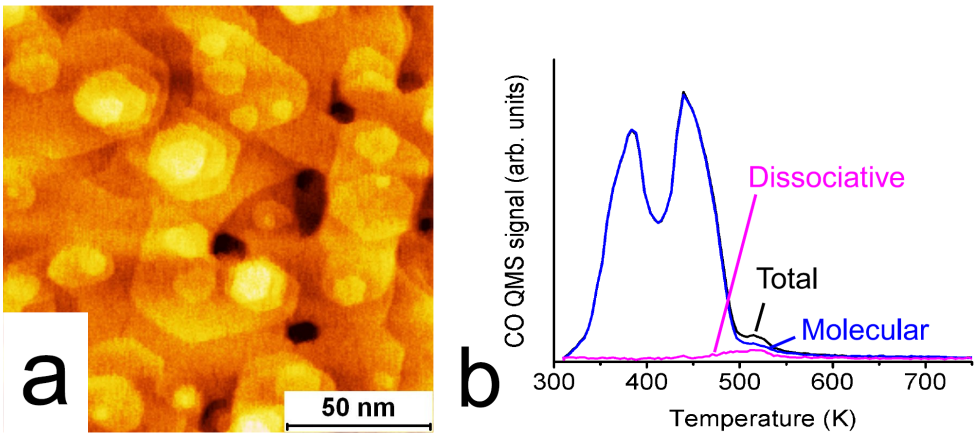

(a) (b)

Figure 3.11: Figure a is a STM image of the PVD nanoparticles annealed to 900 K. Figure b shows an isotopic labeled CO TPD experiment distinguishing the molecular and dissociative desorption.

3.5 Discussion

The gap in CO desorption from ruthenium nanoparticles and a ruthenium single has in this study been bridged by annealing a PVD-grown thin film of ruthenium to high temperatures. By demonstrating that dissociative CO adsorption is observed both before and after annealing in case of the PVD-film provides information that HOPG do not poison the undercoordinated ruthenium step sites which is proven to be responsible for CO dissociation [27][34]. The formation of the polycrystalline structure of the PVD-film in fig. 3.11(a) is caused by an epitaxial relationship between the deposited Ru particles and the HOPG

surface. The polycrystalline structure is not observed for the mass selected nanoparticles in fig. 3.8 upon annealing to 900 K which do not have the same characteristic epitaxial growth. The setup investigating the ruthenium nanoparticles cannot heat the nanoparticles to more than 900 K due to current limitations. It is expected that the polycrystalline structure with CO desorption similar to the single crystal could be obtained by annealing to higher temperature.
The reverse transition in desorption behavior between that of the Ru single crystal surface and that of Ru nanoparticles is demonstrated by sputtering a single crystal surface. The surface morphology is probed by CO TPD as function of the sputter time and clear evidence of changes in surface sites are seen in fig. 3.9C. The amount of step sites, i.e. the β-peak, correspond to the small shoulder at 510 K for the non-sputtered surface. The β-peak increases with more sputtering and changes into a broad feature ranging from below 500 K to at least 600 K for the surface sputtered for 5 min. The change in the β-peak feature indicates that sputtering introduces more undercoordinated sites than those present in the (0 1 54) surface. The broad feature implies different kinds of sites exist giving rise to different desorption temperatures of dissociatively adsorbed C and O. The molecular desorption feature at 390 K gradually disappears, while the desorption feature at 460 K, corresponding to more strongly bound molecular CO, shifts downwards in temperature with increased sputtering. The effect can be explained by having smaller average terrace sizes on the sputtered surface compared to the non-sputtered surface. The width of the terraces may be too small to accommodate the ordered $(\sqrt{3} \times \sqrt{3})$R30° CO overlayer structures found on extended (0001) facets mentioned in sec. 3.2. It has been suggested by Jakob *et al.* that the terrace region 1-2 nm from the step exhibits a compressed lattice compared to (0001) terrace, which would result in a weaker binding of CO [40][41]. With a higher abundance of terrace sites caused by sputtering and the closer proximity of steps, more weakly bonded CO is expected on the surface which is in excellent agreement with the CO TPDs presented.
In the presented work CO desorption from the sputtered surface starts immediately upon heating from room temperature, whereas the desorption from the non-sputtered surface is delayed to approximately 20 K above room temperature. The CO TPD spectra from the sputtered surfaces implies that CO is not probing all sites available on the surface contradictory to the TPD spectrum from the non-sputtered surface. Further experiments of CO desorption from below room temperature is needed to conclude why the total CO desorption area decreases with increased sputtering time in fig. 3.9C.

3.6 Summary

The desorption and dissociation from ruthenium surfaces have been investigated. The importance of the undercoordinated sites for CO dissociation has been clarified by suppressing the step sites with sulfur. Furthermore, sputtering of a single crystal ruthenium surface has indicated the same trend by inducing defect sites on the surface.
The CO desorption from a single crystal surface has been bridged with CO desorption from

ruthenium nanoparticles. Annealing the nanoparticles to 900 K made the grown thinfilm exhibit CO desorption spectra similar to the single crystal. Equally, sputtering the single crystal made the desorption spectra similar to the nanoparticles. The transition was found to be reversible for the single crystal.
The CO desorption experiments bridging single crystals and nanoparticles demonstrate the complementary nature of both model catalyst systems. The project has given validity of studying both systems in order to narrow the materials gap to more complex industrial catalysts.

Chapter 4

Ammonia oxidation on Cu/Ru thinfilms

In this chapter a study on optimizing catalysts for ammonia oxidation will be presented. The project is a collaborative work between the Parallel Screening setup and a plug flow reactor setup managed by Sine Olsen and Debasish Chakraborty. The project is an excellent example of how an UHV study of characterization, testing and optimization has led to an improved catalyst which afterwards is deployed to a high surface area support.

4.1 Introduction

Ammonia is one of the most important and produced industrial chemicals due to the wide range of applications. Large quantities of ammonia are produced for its use as fertilizer but ammonia is also used for removal of NOx in automotive exhaust, production of nitric acid through the Ostwald process. Finally, ammonia is used as a source and storage of hydrogen for fuel cells. The impact and perspectives of ammonia have led to an increase in interest within science.
Unfortunately, ammonia also has some drawbacks to its use. Namely the fact that ammonia and the NOx by-products act as hazardous compound to the environment and need to be avoided. Unused ammonia can be removed by Selective Catalytic Oxidation (SCO) into non-toxic nitrogen and water and can potentially limit the emission into nature while Selective Catalytic Reduction (SCR) uses ammonia to reduce NOx in automotive exhaust [42–47]. The high energy content of hydrogen of 142 MJ kg^{-1} makes hydrogen interesting as a future energy carrier [48]. Storing hydrogen in different complexes has received much attention and the high hydrogen content in ammonia can in perspective be useful as feedstock for the hydrogen fuel cell [49][50]. The hydrogen fuel cell has a very low tolerance towards ammonia. Excess ammonia needs to be removed in order to extend the life time of the fuel cell. In the ideal case a catalyst burns leftover ammonia in the environmental clean reaction:

$$2NH_3 + 1.5O_2 \rightarrow N_2 + 3H_2O \tag{4.1}$$

The removal of NOx as by-production of a chemical reaction is important for an environmental concern. The emission of NOx to nature needs to be limited and precautions made to meet the demands. The ammonia oxidation reaction is important for several applications for reducing the NOx emission. Ammonia oxidation is used for removing slip ammonia from the NH_3 SCR of diesel engine exhaust added to decompose the NOx formation [51]. The NOx generated from diesel engine is harmful for the human health and in order to follow the regulations, the exhaust of the diesel engines is treated for NOx removal. The ammonia oxidation reaction is further used to provide heat for the ammonia decomposition catalyst and for the removal for of ammonia traces in biogas which generates NOx if the burned gas contains NH_3 [52]. For all applications very low light off temperature for the ammonia oxidation catalyst is needed as well high selectivity to reduce the slip of NOx and NH_3 species to the environment. The state of the art catalyst for oxidizing ammonia consists for scares and expensive metals such as platinum and palladium and better alternatives are needed [53].
In the study presented in this chapter, a surface scientific approach is used to produce different model systems of transition metals. The systems react differently to the TiO_2 substrate with some showing a Strong Metal Support Interaction (SMSI). A model system containing Cu and Ru is found to stabilize in an overlayer structure with copper on top for ruthenium. The Cu/Ru system is characterized by XPS and ISS before and after being exposed to reaction conditions. The optimal structure of the catalyst is further applied to a high surface area alumina support. The catalyst is evidently performing better than both copper and ruthenium as in the case of the model system.

4.2 Fe, Ni and Pt thinfilms

In the first project, the strength of the experimental setup is in focus, namely the parallel screening. A number of systems are deposited for various applications. The first systems under investigation contain Fe, Ni and Pt. The Fe/Ni systems are extremely interesting because they are "cheap" catalysts for ammonia decomposition as opposed to Pt that is known as the state of the art within ammonia oxidation but also extremely scarce. However, as mentioned in sec. 2.1.1 the three metals all have shown to have a SMSI with TiO_2.
A series of 50 Å thick thinfilms are deposited as described in sec. 2.2.1. The size of the circular spots are 1 mm in diameter determine by a mask. The catalytic spots contain different combinations of nickel and iron, ranging from pure nickel to pure iron spots as well as co-evaporated spots of Ni:Fe ratios of 1:4, 1:1 and 4:1. The project is a further investigation of the study by Bredmose *et al.* on a series of Ni/Fe catalyst on a high surface area support [54]. The Ni/Fe catalysts have proven to be a relative high performing and synthesized of two abundant metals. The catalyst has further proven to be selective working in high H_2 to NH_3 ratio simulating the end of an ammonia decomposition plug flow reactor. In fig. 4.1 a XPS spectra is shown for a 50 Å thick thinfilm of evaporated Ni. The lens mode of the analyzer is set to High Magnification having a lateral resolution of 125 μm at

the best. The lateral resolution is further investigated by scanning across the sample while measuring a fixed photoelectron energy corresponding to Ni. By centering the sample at the highest count rate only the 1 mm spot is probed. The spectrum contains the measurement before and after the Ni system is exposed to 1 bar reactant gas of 5.000 ppm NH_3/Ar and is heated to 750 K.

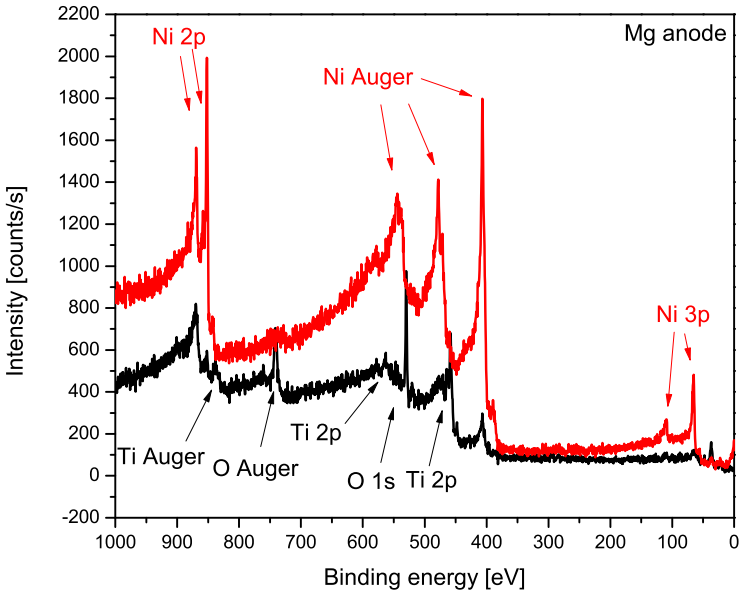

Figure 4.1: Overview XPS spectrum of a 50 Å thick 1:1 Ni:Fe thinfilm before and after being exposed to reaction conditions. The spectrum is obtained using the Mg anode.

The figure shows that the thinfilm as deposited before being exposed to reaction conditions only contains the deposited nickel. Under the ammonia decomposition reaction conditions, the Ni thinfilm did not exhibit any activity towards ammonia decomposition. Comparing the XPS spectra before and after high pressure experiment shows a drastic drop in the Ni signal while Ti and oxygen appears. The lack of activity towards ammonia decomposition was concluded to be cause by the mobile Ti creeping up on the catalytic spots covering the Ni thinfilms as an effect of the SMSI.

The SMSI is observed for all thinfilms produced involving Fe and Ni. In the case of Pt, the thinfilms exhibited high activity towards ammonia oxidation and low light-off temperature but also quickly deactivated. The films have proved to be partially covered by Ti after being exposed to reactions conditions. Further investigations of Fe, Ni and Pt thinfilms were therefore dropped due to the SMSI effect.

4.3 Cu and Ru thinfilms

The second screening study involves a Cu/Ru system for ammonia oxidation. In literature it is reported that the position of the d-band center determines the reactivity of transition metals. Changing the position of the d-band center is a way to tune the catalytic properties of transition metals. The formation of pseudomorphic overlayers can be used to manipulated the d-band position and hence the reactivity as described in sec. 1.4.2.
Several noble metals have been tested for ammonia oxidation [42][46][47][55][56]. Copper is a good catalyst for ammonia oxidation. The ammonia binds to the copper surface via the nitrogen with a lone pair [57]. Pre-adsorbed oxygen on the copper surface changes the reaction scheme and lowers the activation barrier for NH_2 dissociation with an overall heat of reaction of -611 kJ/mol [42][58]. For the ammonia decomposition reaction the rate limiting step is desorption of N_2 [59].
For Cu to form a phase separated overlayer structure, a few candidates in the form of Ru, Rh, Pd, Ag, Ir, Pt and Au were found. Looking into the surface segregation characteristics of the bimetallic combination of Cu and all the mentioned metals only the Cu-Ru combination resulted in very strong segregation of Cu on the surface [12]. The Cu-Rh combination gives a strong segregation tendency of Cu, so Rh can potentially also be a candidate as host metal. However, the bimetallic Cu-Ru system is selected in this study due to the strong segregation tendency of Cu hereby having a higher likelihood of a Cu overlayer formation. Cu is reported to form an overlayer on Ru in literature [60][61].
Screening studies of monolayer overlayers of transition metals suggest that a ML copper on ruthenium shifts the d-band 0.3-0.5 eV upwards thereby binding the oxygen stronger [8]. Theoretical studies further predict the Cu/Ru structure to be extremely stable [12].

The Cu/Ru system was studied in great detail in the late eighties for hydrogenation reactions of mainly ethane and methane [61]. The two metals were found to phase separate with copper having the lowest surface energy. Different model systems of copper and ruthenium have been studied thoroughly in literature. The Cu/Ru system exhibit interesting effects with copper and ruthenium being immiscible and do not alloy. Instead the two metals phase separate and with copper having the lowest surface energy it is favorable to segregate to the surface. The physics of the Cu/Ru system is interesting as the reactivity of the surface can be tailored and by strain of the copper overlayer according to d-band model sec. 1.4.
The only interaction between Cu and Ru is on the microscopic level in the interface between the two metals. Sinfelt *et al.* suggested a model of copper covering ruthenium as chemisorbed in a bimetallic cluster [62]. The most studied system is the Cu/Ru(0001) where copper of varying coverage is deposited on a Ru(0001) single crystal. Here copper is found to form two dimensional islands of pseudomorphic overlayers [60][61]. As more copper is deposited, 3-D islands of copper are grown before finally forming a full monolayer. Furthermore, Kim *et al.* have shown that it is not possible to apply the single crystal overlayer behavior to the Cu/Ru clusters as small size and a defected structure inhibits this aggregation of the two-dimensional islands [63]. The defect sites have been

suggested to block the migration of copper to the surface inhibit the epitaxial growth of copper on low defect annealed ruthenium (0001) surfaces [60][64]. Annealed ruthenium thinfilms have been studied by TPD and are comparable to the Ru(0001) surface [64]. For low copper coverage the desorption features of CO on ruthenium is still observed for in the TPD measurements [60][61]. It is predicted based on the CO TPD that Cu overlayers on Ru is electron rich compared to a surface of Cu atoms of bulk Cu [65].

In this study, a surface scientific investigation of Cu/Ru system has been conducted. Both co-evaporated structures and overlayer structures of Cu on top of Ru are studied. As the activity of Cu can be increased for ammonia oxidation reaction the system is impregnated to a high surface area catalyst which has been synthesized and tested.

4.3.1 Thinfilms of co-evaporated Cu/Ru

In this section the data from co-evaporated thinfilms of copper and ruthenium will be presented. The thinfilms are produced by the Oxford Applied Research H-PEB4 electron beam evaporator using physical vapor deposition as explained in sec. 2.2.1.
A series of thinfilm model systems of copper and ruthenium is produced varying the ratio between the two transition metals. The metallic thinfilms are evaporated in spots of 1 mm in diameter and the deposition of the metals is monitored by a QCM. Each of the spots are characterized by both XPS and ISS as deposited according to chap. 2. After characterization the sample is transferred to the HPC and exposed to reactant gases and elevated temperatures. Each of the metallic thinfilms are monitored for ammonia oxidation and other side reactions. After testing the temperature is decreased to room temperature and the HPC is evacuated. The sample is transferred back to the UHV analysis chamber and characterized by XPS and ISS.
In fig. 4.2 a typical XPS overview spectrum is shown of a 50 Å co-evaporated thinfilm of 1:3 Cu:Ru before and after catalytic testing in the HPC.

When the TiO_2 sample is transferred into the HPC and exposed to the reactant gases a scan of the catalytic activity at 600 K of the surface is made using the gas sampling device discussed in sec. 2.3.1. In fig. 4.3 the formation of nitrogen is shown for the TiO_2 with 4 spots deposited.

The figure clearly shows four distinct peaks originating from the four deposited spots. The difference in catalytic activity for the individual spots is clearly seen. The opposite trend is observed for the oxygen being consumed in the reaction. By rotating the figure it is furthermore obvious that there is no spillover in between the single spots as the measured signal reaches the background in between the spots.

The scan is used to calibrate the exact positions of the catalytic spots for the gas sam-

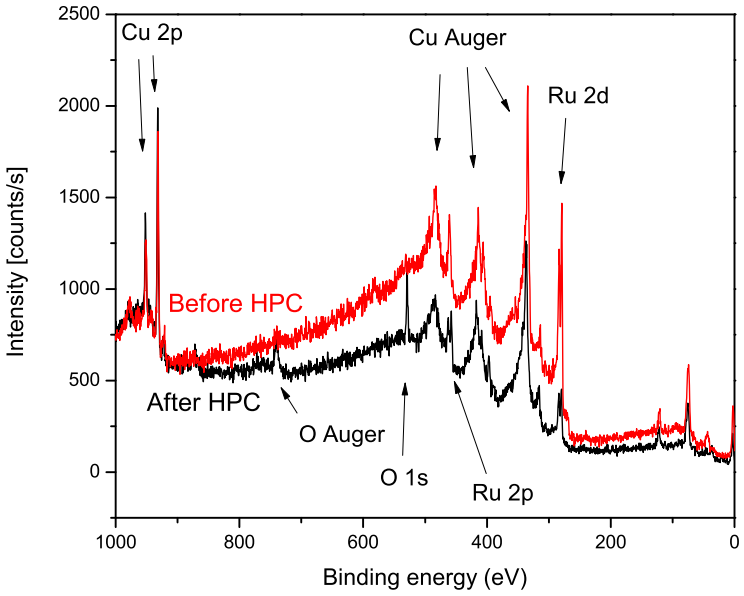

Figure 4.2: XPS overview spectrum of a co-evaporated Cu/Ru thinfilm of 1:3 Cu:Ru.

pling device. After the scan, the gas sampling device is moved a single spot where the distance between aluminum nozzle and sample is adjusted. The activity of the spots is then measured individually on the exact position of the spots. In fig. 4.4 the typical mass spectrometer data on a single catalytic spot is shown. The temperature is ramped up and down in steps of 25 K. In the figure the signals attributed to nitrogen (black) and oxygen (red) are shown as well as the temperature profile (blue). The signals are normalized to the argon signal as discussed in sec. 2.3.1, due to the leak through the glass capillary being temperature dependent.

The activity towards ammonia oxidation is measured as the increase in the 28 AMU signal, excluding the CO contribution. Equally the signal for 32 AMU decreases as a sign of the oxygen being consumed in the ammonia oxidation process. The ammonia level is measured on 17, 16 and 15 AMU and it drops as the temperature increases. The model system is 100% selective towards clean combustion as NOx is not observed for any of the catalytic Cu/Ru spots on TiO_2.
After the catalytic testing all spots on the TiO_2 are characterized by XPS and ISS. The sample is then cleaned by sputtering and annealed before the next series of experiments are conducted. A number of films are characterized and tested this way. The co-evaporated thinfilms are deposited to be 50 Å thick and ranges from pure copper to ruthenium and combinations of 9:1, 1:1, 1:3 and 1:9 of Cu:Ru ratio. In fig. 4.5 the ammonia oxidation activity of the co-evaporated thinfilms is seen.

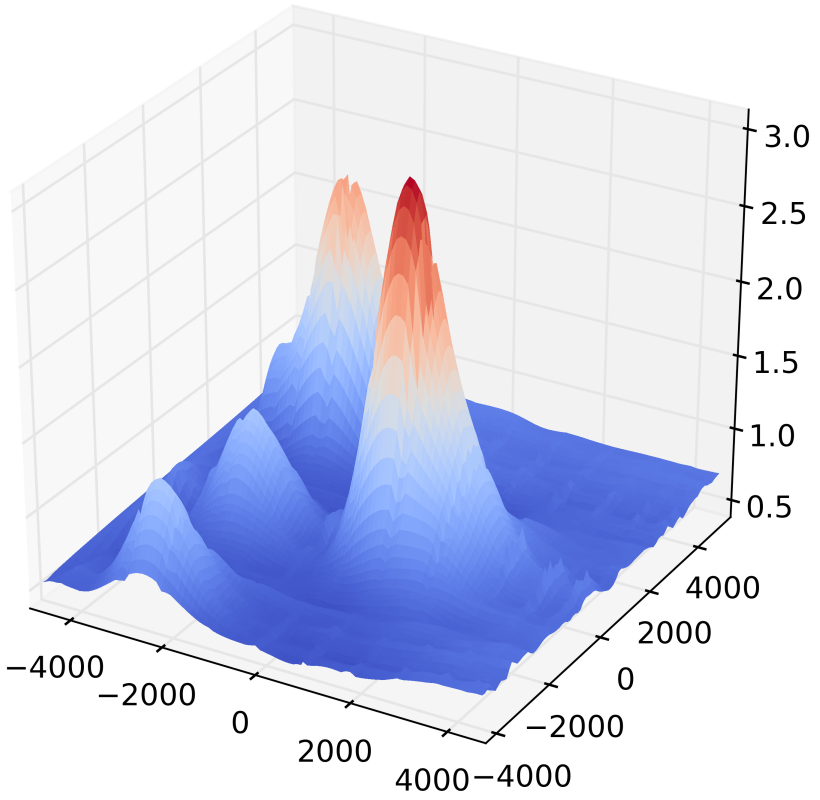

Figure 4.3: A scan of the TiO_2 surface at 600 K under reaction conditions in the HPC.

The figure shows that Cu is almost inactive under the reaction conditions whereas ruthenium exhibits much higher activity towards ammonia oxidation. Furthermore, by adding copper to the bulk of the ruthenium thinfilm do not have any beneficial effect on the catalytic performance.

As previously mentioned, XPS and ISS are performed before and after testing. In fig. 4.6 the XPS analysis of the co-evaporated thinfilms copper and ruthenium are seen before and after testing. The analysis is made on the Cu 2p peak and the Ru 3d peak subtracting a Shirley background and applying sensitivity factors.

The XPS data before and after exposing the co-evarporated thinfilms to high pressure of reactant gas suggest a clear segregation of Cu to the surface of the catalyst. This is

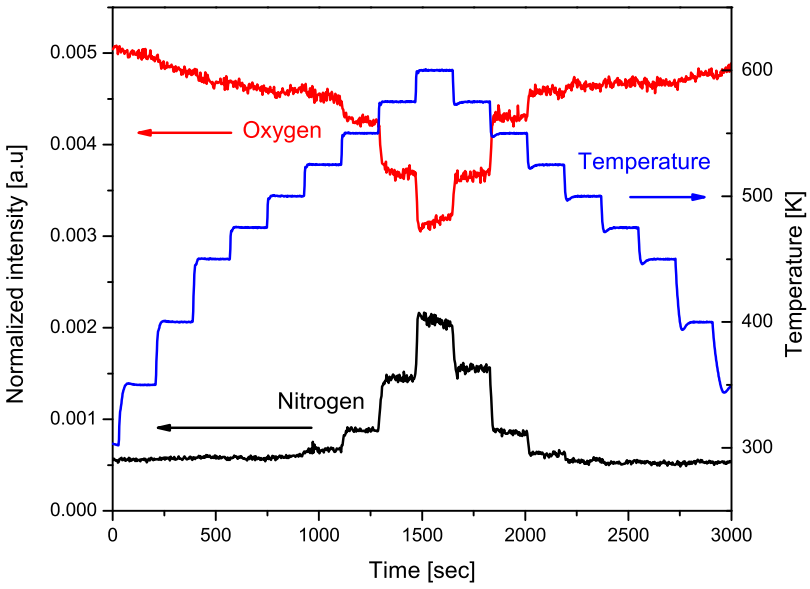

Figure 4.4: Mass spectrometer data from a typical ammonia oxidation experiment. In this case the thinfilm consists of 1:3 co-evaporated Cu and Ru. The sample is heated and cooled in steps while the nitrogen and oxygen signals are traced. The signals are normalized to the argon signal.

well-known from literature where X-ray diffractography and thermal analysis proves Ru and Cu not only to be immiscible in the solid phase but also in the liquid phase [66]. The tendency seen in fig. 4.6 with the Cu signal increasing during the testing phase is also observed for the more surface sensitive ISS spectrum. In fig. 4.7 the ISS peak area analysis of the co-evaporated thinfilms is seen before and after testing. It is clear that the Cu segregates to the surface of the thinfilm as expected from the phase diagram of Cu and Ru. In this study both ruthenium and copper is observed by ISS for low coverage of copper. The lower activity of the co-evaporated thinfilms can in the light of the ISS and XPS analysis be explained by not reaching the equilibrium structure during the testing phase.

Even though the surface concentration of copper increases during the high pressure testing, a full copper overlayer is not formed as ruthenium is observed by ISS. The segregation of copper to the surface of ruthenium, seen with both XPS and ISS, implies that a copper overlayer is the equilibrium structure of the Cu/Ru system.

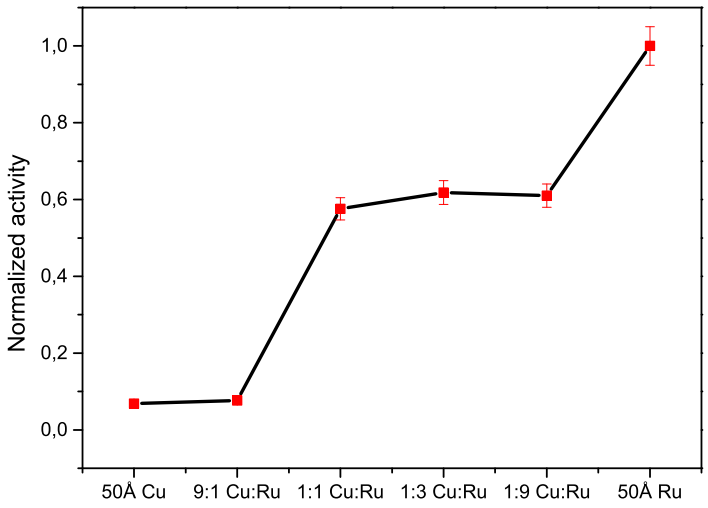

Figure 4.5: Ammonia oxidation activity of the co-evaporated thinfilms and for pure copper and ruthenium.

4.3.2 Thinfilms of Cu overlayers on Ru

The expected equilibrium structure of the Cu/Ru system with copper overlayers on ruthenium is further investigated. A number of Cu/Ru systems are evaporated on the TiO_2 substrate for varying overlayer thickness of copper on top a 50 Å Ru thinfilm. The catalytic 1 mm spots are characterized and transferred to the HPC where they are exposed to 1 bar of reactant gas. The spots are tested for their catalytic activities towards ammonia oxidation using the same procedure as for the co-evaporated thinfilms.
In fig. 4.8 the activity for the increasing thickness of the copper overlayer is shown. As seen from the figure, pure Ru (0 Å in the figure) exhibits high activity for ammonia oxidation whereas pure Cu (50 Å in the figure) spot is almost inactive. The Cu/Ru overlayer system exhibits higher activity towards ammonia combustion than both pure ruthenium and copper. A volcano curve is observed when plotting activity as function of the thickness of the copper overlayer. The optimal Cu thickness is 2 Å according to the experiments.

Adding a copper overlayer in the order of a monolayer to the ruthenium thinfilm improves the catalytic activity and the Cu/Ru system compared to the Ru catalyst is almost 100% better. The copper overlayer thickness in the figure is varied from 0.5-5Å with the system performing better for a copper overlayer in the range of 1-4 Å. The behavior of the Cu/Ru overlayer system is remarkable as it is counterintuitive to make a catalytic structure more active by stacking two less active materials. As for the co-evaporated films the selectivity

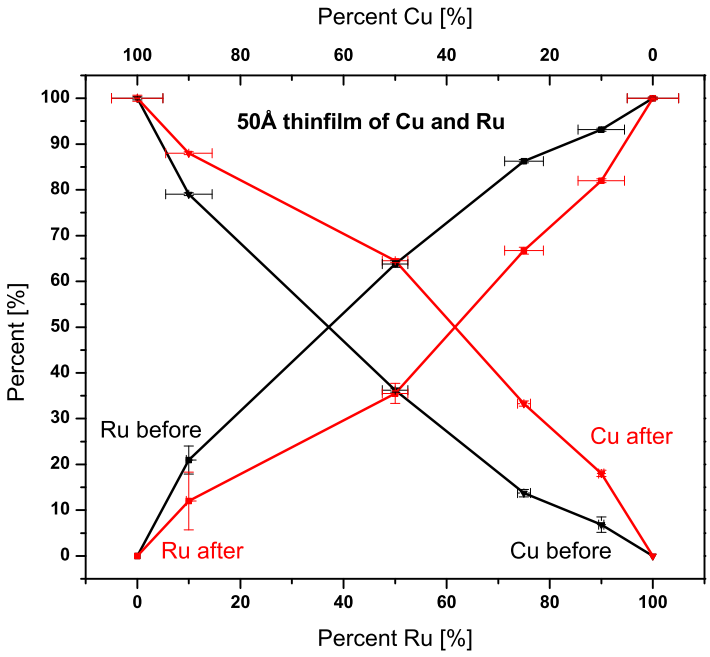

Figure 4.6: The ratio between the area of the copper 2p peak and ruthenium 3d peak for the different co-evaporated thinfilms before and after testing.

of the copper overlayer on ruthenium the selectivity is 100%, forming no NOx.
The atomic radius of Cu is 1.28 Å which means the optimal 2 Å overlayer corresponds to copper coverage of 0.78 ML. The activity measurements of the copper overlayers stand in clear contradiction to the activity measurements from the co-evaporated thinfilms. Where incorporating copper in the ruthenium bulk has a negative effect on the activity towards ammonia oxidation, adding just 2 Å copper on top of a ruthenium thinfilm made the thinfilm 100% better.

The structure of the Cu/Ru overlayer system is further investigated by XPS and ISS to gain insight to the origin of the improved catalytic performance. The XPS data is obtained from the Ru 3d and the Cu 2p peak. Shirley backgrounds are subtracted and sensitivity factors applied and the XPS data is presented in fig. 4.9. The horizontal error bar indicates the uncertainty on the deposition rate determined by the QCM whereas the vertical error bar indicates the uncertainty in the area measurement of XPS peaks.

The XPS data for the copper overlayer suggest the system to be stable as the system appear not to change drastically during catalytic testing as seen in fig. 4.9. A clear trend is seen of the copper signal increasing for thicker copper overlayers as expected. The XPS signal of the overlayer structure showing the highest activity towards ammonia oxidation is observed to consist of 95% ruthenium and 5% copper.

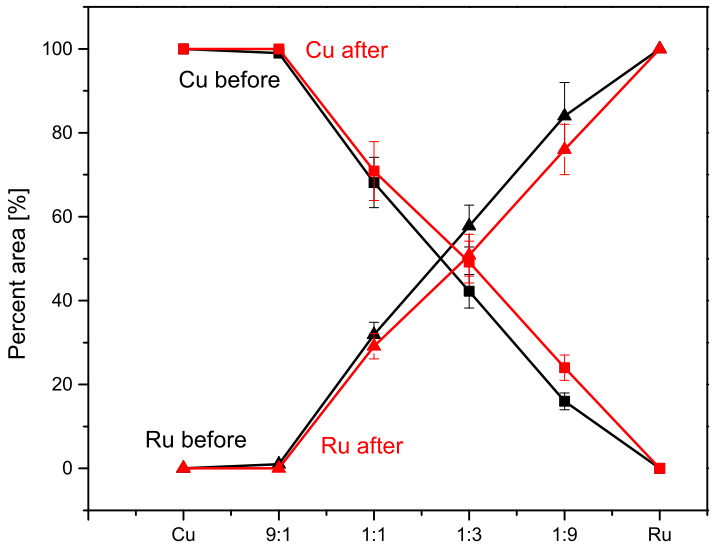

Figure 4.7: The ISS peak area analysis of the co-evaporated thinfilms before and after testing.

The catalytic performance of the Cu/Ru system is very sensitive to the thickness of the overlayer however with copper having an enhancing effect. For the overlayer structured catalyst, ISS is only performed after testing as the catalyst is very sensitive even to light sputtering due to the very thin overlayer. Even though mild conditions are used for ISS, the light sputtering is seen to affect the copper overlayer. ISS is therefore not performed before experiments for the overlayer structure. In fig. 4.10 the ISS data of the ruthenium and copper peak is collected after high pressure experiments.

The ISS analysis shows that both copper and ruthenium is present in the surface for both thin and thicker overlayers. The figure shows that the 2 Å copper overlayer, exhibiting the highest activity, has a 1:1 surface concentration of copper and ruthenium.

4.3.3 Cu/Ru on high surface area support

The Cu/Ru system is applied to a high surface area alumina support to synthesize a real catalyst. The work done on the high surface area support system is conducted by Sine Olsen and Debasish Chakraborty.

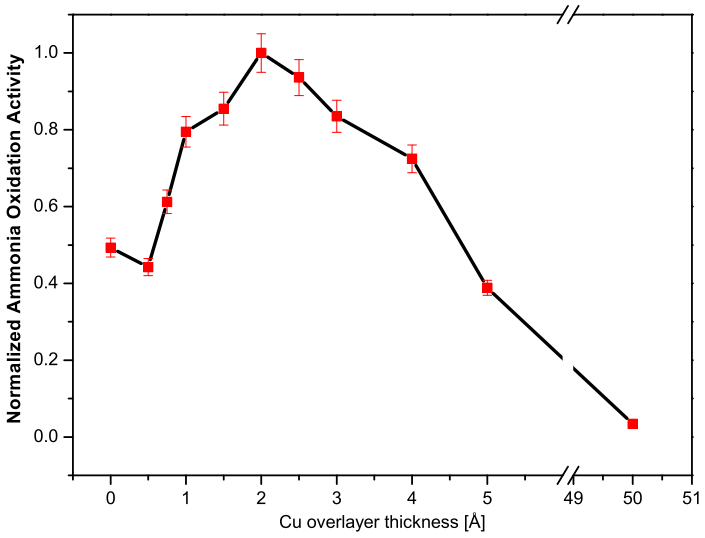

Figure 4.8: The activity of ruthenium thinfilms with varying thickness of Cu deposited on top towards ammonia oxidation.

The high surface area catalysts are prepared by incipient wetness impregnation. Hydrated $RuCl_3$ is dissolved in millipore water which is poured onto appropriate amounts depending on batch size of alumina powder (Puralox TH 100/150) provided by Sasol Germany GmbH. Standard metal concentration results in 1 weight percentage ruthenium on alumina. The catalyst is dried at RT at least overnight. The catalyst is then reduced at 500°C in an approximately 20 ml/min pure H_2 flow for 2 hours. Immediately after the reduction the catalyst is impregnated with very slight amounts of copper(II)nitrate from Merck corresponding to various fractions of Cu monolayers on the Ru particles. The catalyst is dried at room temperature overnight and reduced in-situ immediately before testing.

The high surface area catalysts are tested in a plug flow reactor setup. The catalyst is suspended in a glass tube embedded in quartz wool. The reactor is placed in an oven and the temperature of the catalyst and the oven is measured by a K-type thermocouple individually. The inlet of the reactor is connected to a gas manifold where the reactants are mixing and the composition is set by flow controllers. For experiments the flow is set at 10.75 ml/min of 5000 ppm NH_3 in argon, 4 ml/min of 1% O_2 in argon and 10 ml/min argon to keep stoichiometric conditions. The outlet of the reactor is measured by a FTIR spectrometer and the pressure is regulated to 1 bar by a pressure controller.

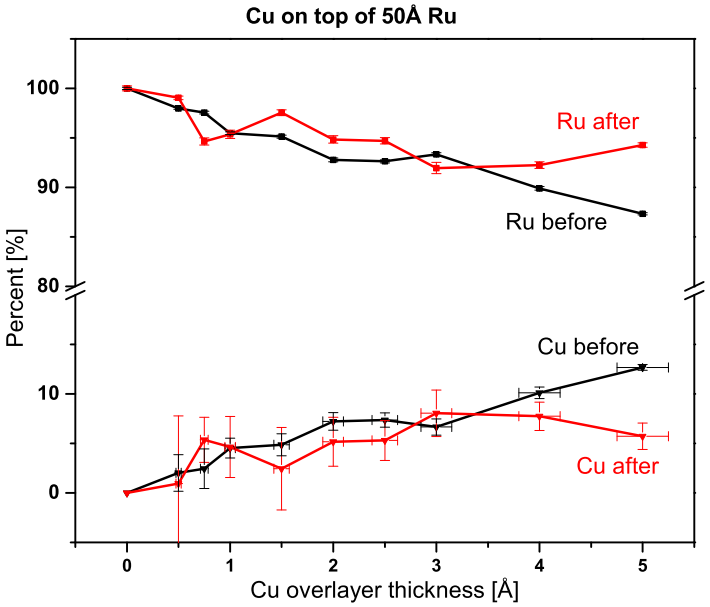

Figure 4.9: The XPS analysis of the Cu 2p and Ru 3d peaks before and after the catalytic spots are exposed to reactant gas a 1 bar and 600 K.

A series of Cu/Ru catalysts on the high surface area support are synthesized by incipient wetness impregnation of first ruthenium and then copper for varying weight percent of copper. In fig. 4.11 the activity towards ammonia oxidation of the real catalyst is seen under stoichiometric reaction conditions at 250°C.

The first point in the figure corresponds to the activity of pure ruthenium whereas the point most to the right corresponds to the activity of pure copper. The points in between represents copper added to the ruthenium. As for the thinfilms, it is possible to improve the catalytic activity towards ammonia oxidation compared both copper and ruthenium by adding copper to ruthenium. For the high surface area catalyst the optimum of copper added is 30 weigh percent.
In contradiction to the PVD thinfilms, the pure copper catalyst exhibits higher activity than the pure ruthenium catalyst. The high surface area catalyst is further synthesized by co-impregnation however the Cu/Ru particles exhibited low activity. This result fits with the co-evaporated thinfilms not improving the catalytic ability of copper and ruthenium. Kim *et al.* have shown that it is not possible to apply the model of the two-dimensional island of copper on ruthenium for smaller cluster meaning the segregation of copper changes with defects. For the Cu/Ru system to exhibit high activity towards ammonia oxidation, ruthenium and copper need to be impregnate successively.

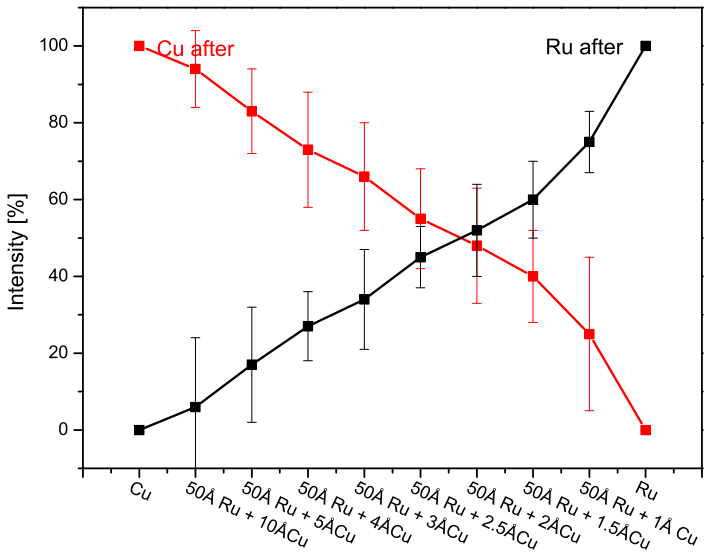

Figure 4.10: The figure shows collected ISS data for the Cu and Ru peak after high pressure testing.

A drawback of the real catalyst on the high surface area support is the selectivity which is shown in fig. 4.12. The plot shows, equally to the activity plot, the selectivity of Ru to the left and of Cu to the right. The different copper overlayers are plotted in between the two. The figure shows the amount of N_2 produced during the catalytic testing compared to the NOx by-products.

The selectivity of the catalyst is better than 90% for all configurations of the catalyst structure.

4.4 Discussion

The testing of the different types of the Cu/Ru catalysts has proved that adding 2 Å Cu on Ru thinfilms and 30 weight% of Cu compared to Ru on high surface area support enhance their catalytic performance. Meanwhile adding copper to an already deposited ruthenium catalyst had a beneficial catalytic effect, co-evaporation and co-incipient wetness impregnation proven the opposite. The contrast in behavior clearly proves the importance of copper being present on the surface of ruthenium.
The two spectroscopy methods applied to the thinfilms in this study, XPS and ISS have shown both copper and ruthenium to be present at the surface. The higher surface sensitivity of ISS compared to XPS provides the information of the copper measured with XPS is mostly concentrated in surface of the thinfilm. This information is intuitive understand-

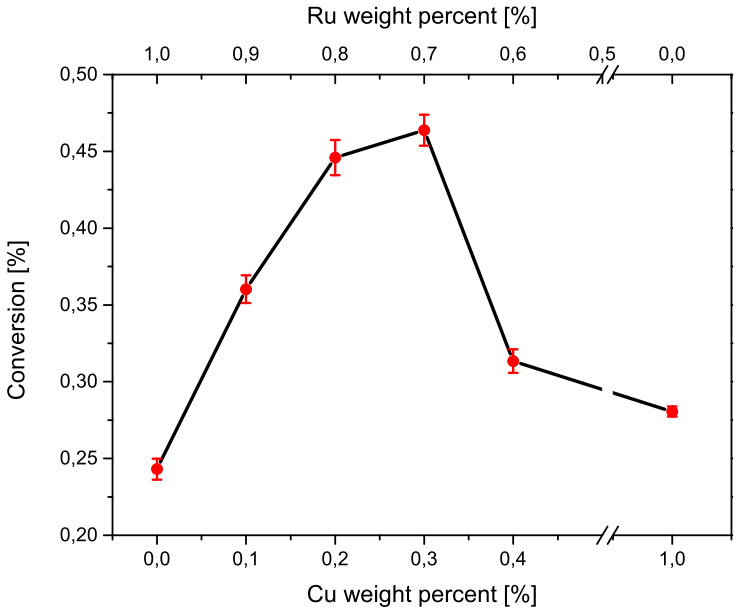

Figure 4.11: The activity of the co-incipient Cu/Ru catalyst deposited on a high surface area alumina support. The optimal structure is found to be 30 weight% of copper for the catalyst.

able as copper is deposited on top of ruthenium.
Literature reports that copper forms a pseudomorphic overlayer on ruthenium [60][61]. The pseudomorphic overlayer is found to grow in 2-D islands on ruthenium until a certain point where 3-D structures start forming. The exact copper coverage needed to see the transition between the 2-D and the 3-D islands is not unambiguous. The transition is found for a copper coverage extending 2 ML by the group of Goodman while the same transition observed at 0.6 ML by the group of Ertl.
The observed enhancement of the catalytic performance of copper overlayers on ruthenium fits well with literature. The formation of the high performing pseudomorphic copper overlayer can be explained by the d-band model presented in sec. 1.4.2. When copper is deposited on ruthenium the bi-metallic interface makes copper follow the lattice of ruthenium. The strain introduced to the copper lattice affects the overlap of the electronic orbitals of copper changing the position of the d-band. The change induced in the d-band explains the volcano shaped activity behavior observed in fig. 4.8.

For copper deposited up to 2 Å with a coverage of 0.78 ML determined by the QCM and experimentally found coverage of 0.5 ML by ISS the activity of the Cu/Ru system increases. For coverage extending this coverage the activity of the systems decreases. This can be explained by the 2-D pseudomorphic overlayer islands growing on the ruthenium surface. At the deposited 2 Å copper, the highest single layer coverage is reached and

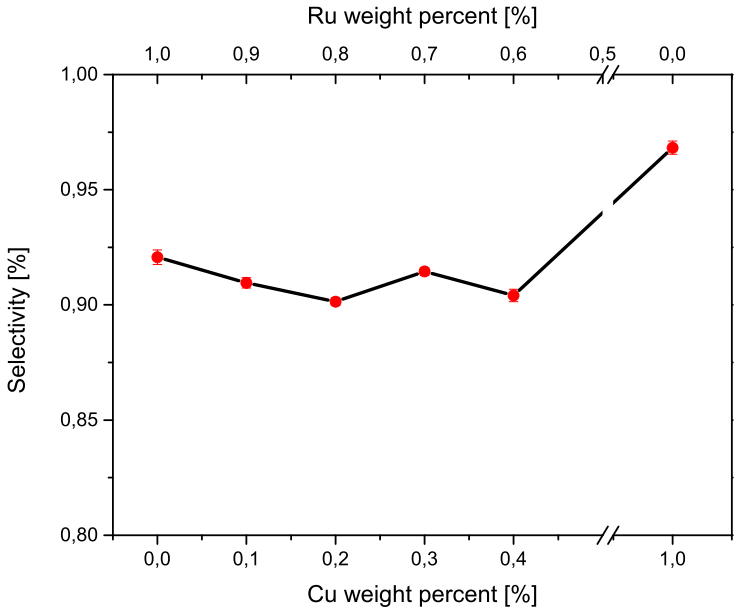

Figure 4.12: The selectivity of the Cu/Ru catalyst. All synthesized catalysts from pure copper and ruthenium to mixed catalysts are found to be 90% selective.

3-D islands start growing on ruthenium. The 3-D islands do not have the same strain of the lattice of the single layer and therefore not the same beneficial effect on the catalytic performance. The copper coverage expected from the QCM rate and the observed copper coverage by ISS agrees well with the findings of Ertl *et al.* of 0.6 ML within the error bars of the experiments.
The stretching of the copper lattice will as a consequence narrow the d-band of copper and shift the d-band center upwards. This behavior is suggested by DFT calculations in literature [58]. The island formation is a consequence of ruthenium annealing to a low defect (0001) structure. Annealed ruthenium thinfilms that have been studied by TPD and are comparable to the Ru(0001) surface [64]. For low copper coverage the ruthenium is still observed for in the ISS measurements as expected from literature [61]. The XPS and ISS analysis clear proves the immiscibly nature of copper and ruthenium with copper phase separating as surface layer on ruthenium. A copper and ruthenium system has previously been found to be active towards ammonia oxidation in a bimetallic mesoporous CuO/RuO_2 structure [67]. This enhanced effect of the catalytic performance by incorporating copper in the ruthenium lattice can however not be achieved by PVD as the metals phase separated under reaction conditions.
The change in the activity of Cu/Ru compared to Cu or Ru is suggested to be purely due to electronic modification of the Cu by Ru. The ensemble effect can be ruled out because Cu will preferentially sit on the undercoordinated sites of Ru, making Ru inactive. It has been shown by Chorkendorff *et al.* that the activity of Ru(0001) for N_2 dissociation is completely suppressed when less than 0.01 ML of Au is deposited on the surface because

of Au atoms blocking the step sites [30]. The volcano curve of Cu/Ru can be explained by considering the thickness of the 3-D Cu islands on Ru. Above 2 Å thickness, the islands start to become thicker and as a result the electronic structure of the surface atoms of the Cu islands are perturbed less and less by the Ru surface and eventually the Cu islands behave like pure Cu, loosing activity completely.
A comparison of all the thinfilms evaporated in UHV is shown in fig. 4.13. Furthermore, ball models are added to the figure to explain the described formation of the pseudomorphic copper overlayer on ruthenium. In the schematic, the army green balls represent ruthenium atoms and the grey balls represent copper atoms.

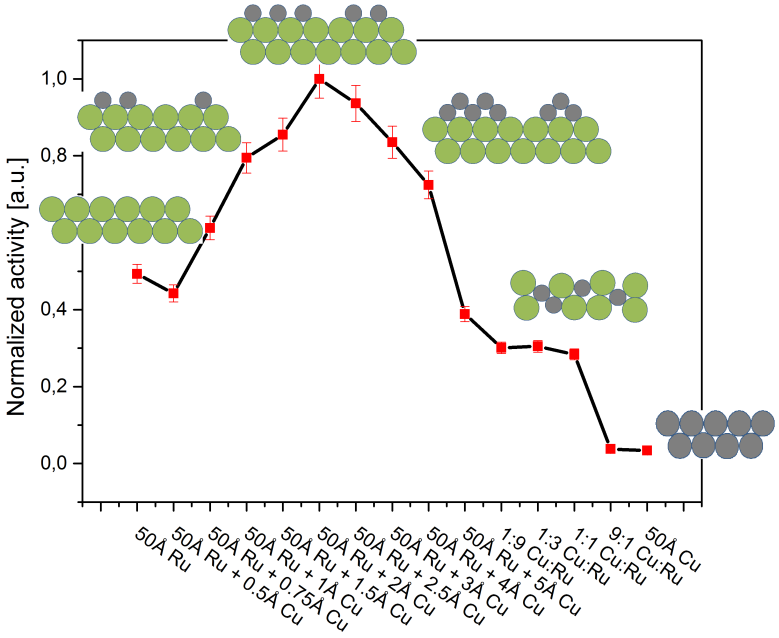

Figure 4.13: The figure shows the collected activity for the pure copper and ruthenium catalyst as well as the co-evaporated thin films and the overlayer Cu/Ru structure. Ball models are added to give insight to the expected copper overlayer structure for different coverage.

4.5 Conclusion

A Ru/Cu catalyst has been proven to be superior to both Ru and Cu catalysts for ammonia oxidation prepared in UHV on TiO_2 and synthesized on a high surface area support. In both cases the Cu/Ru catalyst showed almost a factor two higher activity. The catalyst prepared in UHV did not produce by-products whereas the catalysts prepared on a high surface area support showed a 90% selectivity to produce NO. Counterintuitive, the activity of the Cu overlayer structure exhibited higher activity than both copper and ruthenium.

Incorporating the copper in ruthenium thinfilm did not have the same beneficial effect for system, emphasizing the importance of the overlayer structure. The structures of the catalysts have been investigated by XPS and ISS and Cu clearly segregates to the surface forming a stable surface overlayer. The improved catalytic performance of the copper overlayer can be explained by a shift of the d-band center due to straining of the copper lattice.

Chapter 5

Reduction of industrial $Cu/ZnO/Al_2O_3$ catalyst

This chapter will present the results from a collaborative project between CINF and the industrial catalyst giant Haldor Topsoe. The Cu/ZnO methanol catalyst has been investigated since the fifties and is the state of the art within methanol production. Still, the exact reason for its high catalytic activity remains unknown.
In this chapter a study of the reduction of the industrial Cu/ZnO catalyst will be presented. A series of experiments involving H_2 Temperature Programmed Desorption (H_2-TPD) and N_2O Reactive Frontal Chromatography on the Cu/ZnO have conducted by Sebastian Kuld from Haldor Topsoe after reduction at different partial pressures of H_2. Similar reduction procedures have been made at CINF in a UHV facility where the Cu/ZnO catalyst surface is studied by XPS.

5.1 Introduction

The fossil fuel resources are running low and the need for a sustainable alternative is moving closer. As discussed in sec. 1.3 methanol has the potential to be a future energy carrier. Methanol is a colorless, volatile, flammable, odorless liquid readily miscible in water. Methanol has a high energy density around half of gasoline. There are many arguments for methanol as a future energy carrier and especially in the transport sector. It is a liquid fuel which can be blended with gasoline and ethanol and can be used with modern vehicle technology at minimal incremental costs. The toxicity of methanol is comparable to gasoline and it biodegrades quickly in case of a spill. Another advantage of methanol is the diversity in the feedstock for production. Besides industrial production from natural gas and coal, methanol can be produced from a variety of sources ranging from timber waste, landfill gas, trash, pulp mill black liquor, agricultural waste to CO_2. Finally, methanol has received renewed attention due to the potential of being a solar fuel produced from sea water and atmospheric CO_2.

In fig. 5.1 an illustration of the principle of the CCR cycle is shown. CO_2 is captured

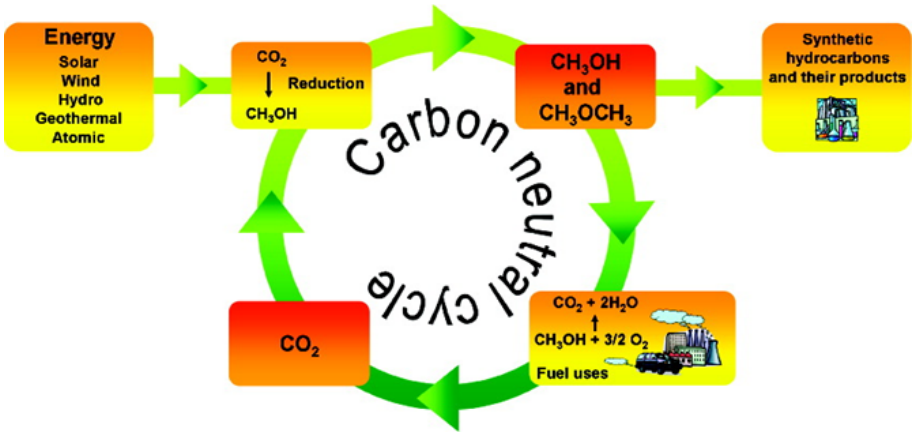

Figure 5.1: The illustration shows the carbon recycling cycle where renewable energy sources are used to produce methanol from unlimited resources from the sea water and reduction of CO_2 from the atmosphere. The figure is captured from [68].

from industry and the atmosphere and reused to form methanol. Currently methanol is industrially produced through the following reaction by converting syngas from fossil fuel by use of a $Cu/ZnO/Al_2O_3$ catalyst.

$$CO_2 + 3H_2 \rightleftharpoons CH_3OH + H_2O \tag{5.1}$$

$$CO + H_2O \rightleftharpoons CO_2 + H_2 \tag{5.2}$$

The Cu/ZnO catalyst exhibits high performance and selectivity for methanol production under reaction conditions. Methanol is produced under relative mild conditions in the order 70 bar and at a temperature around 220°C.

Methanol is an important chemical that is mainly used for production of formaldehyde, acetic acid, MTBE, MTO, Gasoline blending and DME. The use of methanol is growing especially as an energy carrier and synthetic substitute for conventional fuels [4][5]. Synthesis of methanol is carried out over a $Cu/ZnO/Al_2O_3$ methanol catalyst that is used industrially since the 1960's. In literature the nature of the active site for methanol production has been much debated. The importance of ZnO in the catalyst is widely accepted to enhance the performance. The exact role of the ZnO is however is not perfectly clear. At reaction conditions the presence of ZnO_x species have been identified on top of the copper particles as a result of Strong Metal Support Interaction (SMSI) [69–75]. DFT calculations of Zn incorporated into step sites on Cu(211) surface have proven beneficial for the methanol production due to increased adsorption strength of intermediate components and decrease of energy barriers [69].

In this study the SMSI between ZnO_x and Cu under reducing conditions is addressed for an industrial methanol catalyst. A systematic examination using several methods has shown significant dynamical changes in the state of the Cu surface as a consequence of an increasing partial pressure of hydrogen. This study elucidates the pitfalls in chemisorption methods for determination of the Cu surface area and offer a more accurate determination of the specific Cu surface area together with strong evidence that Zn is present in the metallic state in a Cu-Zn-surface-alloy.

The investigations have proven the importance of the copper of the reduction of ZnO into the metallic state. Clear evidence of Zn in the metallic state present on the copper catalyst as a surface decoration is presented. Surface area sensitive methods provide information that the specific copper area decreases with the increase in partial pressure of hydrogen during the pretreatment. This decrease is linear proportional to the increase in the formation of metallic zinc. N_2O-RFC and H_2-TPD combined with a pretreatment in a reducing atmosphere has previously been shown to greatly change the copper area with a transient maximum of methanol synthesis activity [76]. Equally, model systems of Cu/ZnO suggest the pretreatment to have an influence on the morphology of Cu nanoparticles, insinuating a presence of oxygen vacancies in the ZnO [77]. Ambient pressure XPS on Cu/ZnO catalysts of high Cu content has shown a surface decoration of ZnO_x species on the Cu nanoparticles at relative mild conditions [69][78].

5.2 Experimental procedure

The dynamical changes of the industrial $Cu/ZnO/Al_2O_3$ during a pretreatment in hydrogen are investigated using four different methods, namely H_2-Temperature Programmed Desorption, N_2O Reactive Frontal Chromatography, H_2-Transient Adsorption and X-ray Photoelectron Spectroscopy. The $Cu/ZnO/Al_2O_3$ catalyst is treated by two parallel experimental sequences in a fixed bed reactor system at Haldor Topsoe and in the combined High Pressure Cell and Ultra High Vacuum setup described in chap. 2. In fig. 5.2 the experimental procedure for pretreatment of the $Cu/ZnO/Al_2O_3$ catalyst is schematically illustrated.

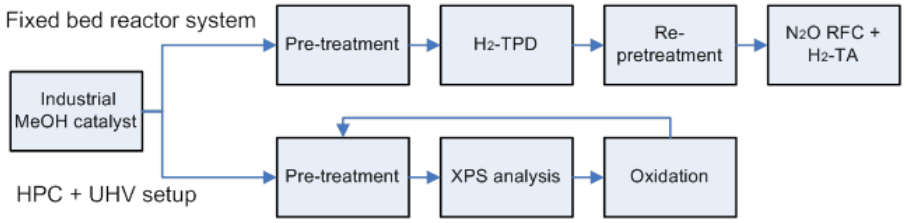

Figure 5.2: The illustration shows a schematic drawing of the pretreatments performed at CINF and at Haldor Topsoe on the industrial $Cu/ZnO/Al_2O_3$ catalyst.

Measurements of the specific Cu area are carried out in a plug flow reactor set-up described in [79] and equivalent to that discussed in [80]. Gases of high purity are used: He (99.9999%), H_2 (99.99909%), H_2/He (1% H_2, 99.9995%), N_2O/He (1% N_2O, 99.9995%). Fast online gas analysis is performed by a calibrated quadrupole mass spectrometer (Balzers GAM 445).

For each experiment, 200 mg of catalyst with a sieve fraction between 150-300 μm are loaded into a U-shaped quartz reactor with an inner diameter of 4 mm. The catalyst used for the present experiments is an industrial $Cu/ZnO/Al_2O_3$ catalyst (60:25:15) [mol%] made by co-precipitation [81]. The catalyst is activated by reduction at 220°C in 1% H_2 and the activity is tested for methanol activity at 220°C for 72 h.
Prior to each Cu surface measurement the catalysts are reduced in 140 ml/min of the H_2/He gas mixture by ramping the temperature by 2 K min^{-1} to 493 K. After the activation procedure, the sample is subjected to a pretreatment in different atmospheres containing increasing partial pressures of H_2. During the pretreatment the temperature is maintained at 493 K for 16 hours. Subsequently, the reactor is purged for 0.5 h with 100 ml/min of He and cooled down to the desired temperature to achieve an adsorbate-free reduced Cu surface.

A two-step series of experiments is applied for each set of different pretreatment conditions. The first step consists of Cu area determination by temperature programmed desorption of H_2 (H_2-TPD) subsequent to the pretreatment. The second step implies a re-reduction and pretreatment followed by a N_2O reactive frontal chromatography (N_2O-RFC) at 50°C [82]. The re-reduction and pretreatment is done in order to insure a clean Cu surface prior to the N_2O titration. After each experiment series, the catalyst sample is replaced. This is done in order to eliminate the possibility of irreversible changes to the Cu surface area caused by the N_2O chemisorption procedure [79].

5.2.1 Determining the specific copper area by H_2-TPD

The first method applied to determine the surface area of copper is H_2 Temperature Desorption. The method is explained in sec. 2.2.2 but uses hydrogen as the adsorption agent. The H_2-TPD experiment is carried out by the following procedure. At room temperature, the gas mixture is changed to pure H_2 from He after reduction and cooled in inert atmosphere. The reactor is then cooled down to the dosing temperature of 250 K by means of a cryogenic oven. At this temperature, the hydrogen is dosed at ambient pressure for 1.5 hour. After dosing of the H_2, the reactor is rapidly cooled down to 78 K and the gas flow is switched to pure He to flush the catalyst for 1 hour in order to remove residual hydrogen. The H_2-TPD profile is obtained by ramping the temperature from 78 K to 473 K with a heating rate of 6 K min^{-1}.
In fig. 5.3(a) a typical H_2-TPD is seen for the industrial $Cu/ZnO/Al_2O_3$ catalyst as func-

tion of time. Furthermore, the H_2-TPD is shown as function of temperature for different reduction pressure of H_2 in fig. 5.3(b). The area under each of the curves can be related to specific surface area of the copper particles in the catalyst.

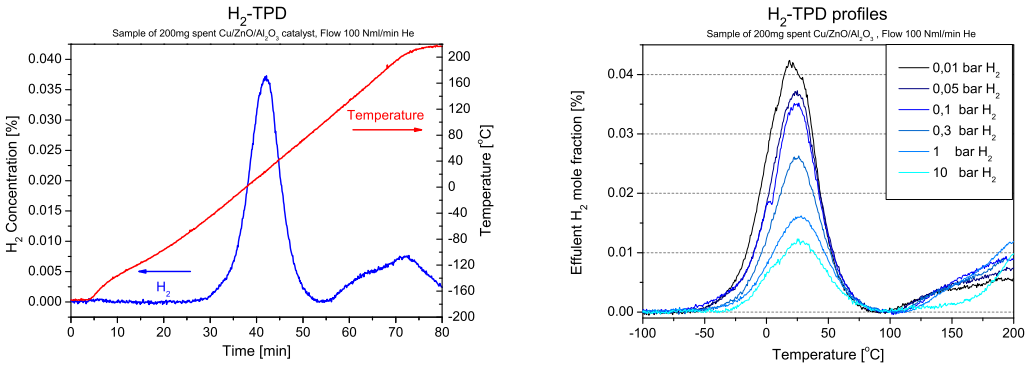

(a) **(b)**

Figure 5.3: Figure a: A typical H_2-TPD measurement. The blue curve represents the H_2 signal belonging to the left axis. The red curve is the linear heating ramp belonging to the right axis. Figure b: The measured H_2 as function of temperature for varying reduction pressure of H_2. The experiments and graphs are made by Sebastian Kuld, Haldor Topsoe.

Fig. 5.3(b) contains the typical spectra of the H_2 desorption profile. The spectrum is recorded after the pretreatment in 50 mbar of H_2. The most pronounced feature is the narrow symmetric H_2 peak centered about 300 K which unequivocally can be assigned to desorption of H_2 from metallic Cu surface sites [79]. The H_2 trace shows a slight increase in the base line towards the end of the temperature ramp associated with hydroxyl groups located on the support.
The specific Cu surface areas are obtained by integration of the left half of the symmetric peak and multiplying by two [80]. The H_2 recombination and desorption is a 2nd order reaction - thus the desorption peak is symmetric [79].

Based on previous TPD studies of hydrogen desorption from Cu single crystals [80], the saturation coverage of hydrogen on all low-index planes of Cu is reported to be half a monolayer (Θ_H=0.5 ML). However, at the applied experimental conditions it is possible to achieve an equilibrium coverage of 80% of the saturation coverage [79]. By considering that each hydrogen atom is blocking two Cu surface atoms [79], the corresponding equation for the dissociative adsorption of H_2 on the Cu surface is:

$$H_{2(g)} + 4Cu_{(S)} \rightarrow 2(Cu - H - Cu)_{(S)} \tag{5.3}$$

The Cu surface area is calculated assuming a molar stoichiometry of $Cu_{(s)}/H_2$=4, a saturation coverage fraction of 0.8, and a Cu atoms per unit area of surface of 1.46×10^{19}

copper atoms m^{-2} [83].

5.2.2 N_2O Reactive Frontal Chromatography

The second method used to determine the copper surface area on the industrial $Cu/ZnO/Al_2O_3$ catalyst is N_2O Reactive Frontal Chromatography. The method relies on measuring the surface oxidation by decomposition of N_2O to N_2. The copper surface area is equivalently determined by N_2O-RFC as reported in [82]. The temperature of the catalyst during the N_2O-RFC measurement is 323 K, which is chosen for selective chemisorption of N_2O while minimizing sub-surface oxidation.

During the titration of the catalyst by N_2O, a thin copper(I) oxide layer is formed according to the reaction:

$$2Cu_{(S)} + N_2O_{(g)} \rightarrow (Cu - O - Cu)_{(S)} + N_2(g) \tag{5.4}$$

Upon the contact with the catalyst the nitrous oxide is almost instantly decomposed and the oxygen atom is chemisorbed to the Cu surface. The formation of a Cu-O-Cu bond inhibits further decomposition. This creates a front of nitrous oxide propagating through the catalyst bed. The evolved gas composition at the exit of the reactor is monitored using the quadrupole mass spectrometer. The oxygen uptake of the catalyst sample from N_2O is quantified using the N_2O/He flow, composition and the time interval between the appearance of N_2 and the intersection between the N_2 and N_2O signals (i.e. the breakthrough of N_2O). A typical N_2O-RFC measurement is seen in fig. 5.4 where the N_2O front is observed as the catalyst is oxidized. The specific surface area of the Cu particles is calculated by assuming a molar stoichiometry of $Cu_{(s)}/O/N = 2$, and a Cu atoms per unit area of surface of 1.46×10^{19} copper atoms m^{-2}.

The characteristic shape of N_2 and N_2O monitored in the effluent gas during an N_2O-RFC experiment is displayed in fig. 5.4. The eluted N_2 formed by the decomposition of N_2O is recorded as a square shaped front starting from approximately min 2 lasting to 4 min. Even after the breakthrough of the N_2O signal the N_2 trace is seen to continue as a small decreasing tail. The square shape profile is attributed to surface oxidation, and the tail is ascribed to subsurface oxidation which is taking place simultaneously [84].

5.2.3 H_2 uptake - H_2-Transient Adsorption

The third method used to determine the copper surface area is the H_2-Transient Adsorption (H_2-TA) experiment. The method relies on reducing the surface oxide to form water. The amount of hydrogen consumed in the process can be coupled to the surface area of copper. The experiment follows directly after the N_2O titration process where the gas mixture is

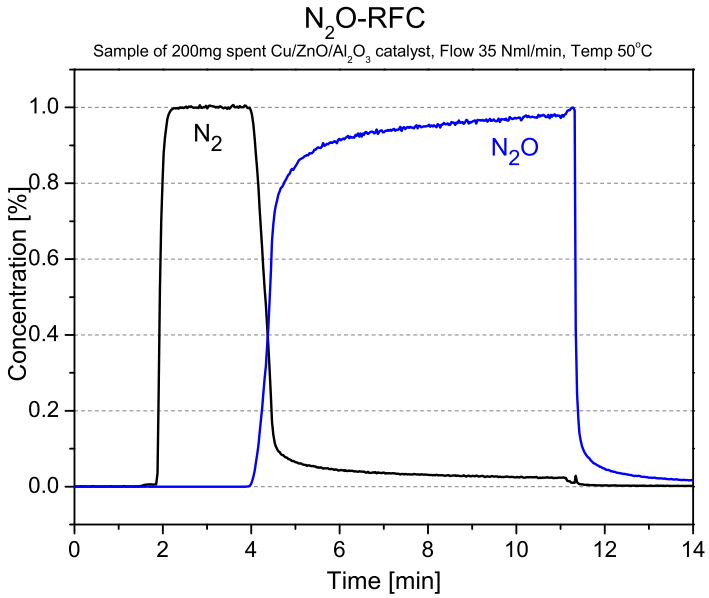

Figure 5.4: The figure shows a typical N_2O experiment. The N_2O at first oxidizes the catalyst and is observed as N_2 and when fully oxidized the N_2O breaks through and is measured. The experiment and graph is made by Sebastian Kuld, Haldor Topsoe.

changed to pure He and the temperature is lowered to ambient temperature. After purging the catalyst for a short period the gas mixture is changed to the dilute mixture of H_2/He. The catalyst is exposed to the H_2/He mixture for 1 hour while monitoring the downstream H_2 trace. This treatment results in a delayed consumption of hydrogen emerging after a few minutes exposure and lasting for around 10 min. The hydrogen uptake is a titration of the chemisorbed oxygen in the copper surface and is named here as Hydrogen Transient Adsorption (H_2-TA). The black line in fig. 5.5(a) shows a typical profile of the isothermal H_2 exposure experiment.

The consumption profile is seen to initiate slowly (∼5 min) and then accelerates to reach its maximum after ∼7 min. The catalyst reaches steady state after 40 min when no further change in the H_2 signal was observed. During the H_2-TA experiment water is not measured to desorb from the surface indicating that the H_2 uptake is adsorbed on the surface as water. In order to couple the H_2-uptake profile to the presence of the Cu_2O surface of the Cu particles of the catalyst, all three oxidation states of the Cu particles in the case of the $Cu/ZnO/Al_2O_3$ catalyst are subjected to the isothermal H_2 exposure experiment. The different oxidation states Cu(0), Cu(I) and Cu(II) of the Cu particles are achieved by testing the catalyst subsequent to calcination (Cu(II)), reduction (Cu(0)) and N_2O titration, i.e. Cu(I). The H_2 trace related to the CuO surface reach the maximum concentration within a few min, showing no signs of hydrogen consumption as seen in fig. 5.3(a). The H_2 trace related to the clean Cu surface (blue curve) is similar in shape to the trace from the CuO

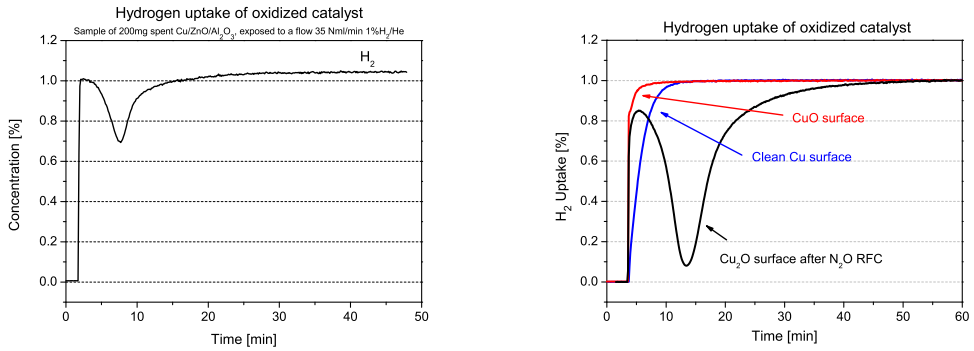

(a) **(b)**

Figure 5.5: Fig. a: The typical H_2 profile for the isothermal H_2 exposure experiment with a surface oxidized $Cu/ZnO/Al_2O_3$ catalyst. Reaction conditions: T=25°C, p=1 bar, Q=35 Nml/min, 1% H_2/He, m_{cat}=200 mg. Fig. b: The profile of the uptake of H_2 for an experiment for three different surface state, Cu (blue), CuO (red) and Cu_2O (black). The experiment is made by Sebastian Kuld, Haldor Topsoe.

(red curve) surface but takes several minutes to reach steady state. This delay is attributed to the establishment of the equilibrium coverage of adsorbed hydrogen on the Cu surface which happens instantaneously upon contact with the hydrogen.
The H_2 signal from the Cu_2O surface initially follows the profile from the CuO surface for a few seconds indicating the presence of no or few active sites. However, the signal quickly bends off to reach a local maximum before dropping again to form the characteristic uptake profile. The distinct drop in the hydrogen concentration suggests that the H_2 is consumed mainly by the reduction of:

$$H_2 + O^* \rightarrow H_2O + ^* \tag{5.5}$$

The reduction kinetics of a $Cu_2O/Cu(111)$ system on the atomic level, using CO, are studied by Fan Yang *et al.* The principle for H_2-TA experiment is described by Fan Yang *et al.* in a combined STM, XPS and DFT study and is explained as an autocatalytic reduction of the Cu_2O surface [85]. A temperature programmed adsorption of H_2 (H_2-TPA) study of the reaction with surface oxygen for $Cu/ZnO/Al_2O_3$ catalyst system [83], shows reduction is possible already at low temperatures (340 K). Compared with these reported experiments the consumption feature of H_2 is related to a transient titration of the chemisorbed oxygen in the Cu_2O surface described in eq. 5.5.
The consumption of H_2 is initially governed by the removal of surface oxygen; however concurrently with a decrease in surface oxygen coverage an equilibrium coverage of hydrogen is established on the Cu surface. The equilibrium hydrogen coverage can be calculated

from a single Langemuirian model with coverage independent Arrhenius parameters [86]:

$$\frac{d\theta_{\mathrm{H}}}{d\mathrm{t}} = 0 \rightarrow k_{\mathrm{ads}} p_{\mathrm{H2}} (1 - \theta_{\mathrm{H}})^2 = k_{\mathrm{des}} \theta_{\mathrm{H}}^2 \tag{5.6}$$

Applying the experimental conditions result in a $\theta_H = 0.04$ ML. By correcting hydrogen consumption measured during the H_2-TA experiment, the method can be utilized for determining the Cu surface area subsequent to oxidation by N_2O.

5.3 X-ray Photoelectron Spectroscopy after reduction

The fourth and last method to determine the surface composition is X-ray Photoelectron spectroscopy as described in sec. 2.2.3. The XPS measurements are performed in the UHV setup described in sec. 2.1 with a base pressure of 10^{-10} Torr. The catalyst can be transferred to a HPC for pretreatment. The pressure in the HPC is controlled by a pressure controller to 1 bar and the gas flow of He and H_2 or oxygen is controlled by mass flow controllers. For the XPS measurements the x-rays are generated from a dual anode x-ray source from SPECS using AlK_α radiation with photon energy of 1486.3 eV while the photoelectrons are measured with a Phoibos Hemispherical Energy Analyzer.
The powder of the industrial $Cu/ZnO/Al_2O_3$ catalyst is pressed to a pellet and mounted in the sample holder described in sec. 2.4. The sample is transferred to UHV where the catalyst is heated to 393 K to remove water from the porous structure. Using the Al anode, the catalyst is characterized with XPS before being transferred to the HPC where it is reduced at 1 bar H_2/He at 493 K for 16 hours. The industrial catalyst is then investigated before and after a series of reduction steps at different partial pressures of hydrogen.
In fig. 5.6 an overview spectrum of the $Cu/ZnO/Al_2O_3$ catalyst is shown. The lens mode of the analyzer is set to Medium Area, optimizing the count rate without observing the sample holder in the XPS spectrum. The lateral resolution is 8 mm in the operating mode but is reduced by the entrance slit. The elements in the catalyst are seen to be copper, zinc, oxygen and carbon. The carbon is used as lubricant when pressing the pellets. Besides the 2p lines of copper and zinc, the Auger peaks also appear.

The reduction of ZnO to Zn is not trivial to detect by XPS. The Zn $2p_{3/2}$ lines for Zn and ZnO are positioned at 1021.4 eV and 1021.7 eV, respectively [87]. The change in valence state for Zn(II) to Zn(0) is observed as a more pronounced 3 eV downward shift in binding energy of the $L_3M_{4,5}M_{4,5}$ Auger peak as seen in fig. 5.7(b).
The XPS characterization subsequent to the pretreatment is conducted to examine the extent to which metallic Zn is present in the surface of the catalyst. The single peak fig. 5.7(a) is resolved during acquisition of XPS data and originates from the Zn $L_3M_{4,5}M_{4,5}$ Auger peak for the industrial $Cu/ZnO/Al_2O_3$ catalyst. The Auger peak is seen for different pre-

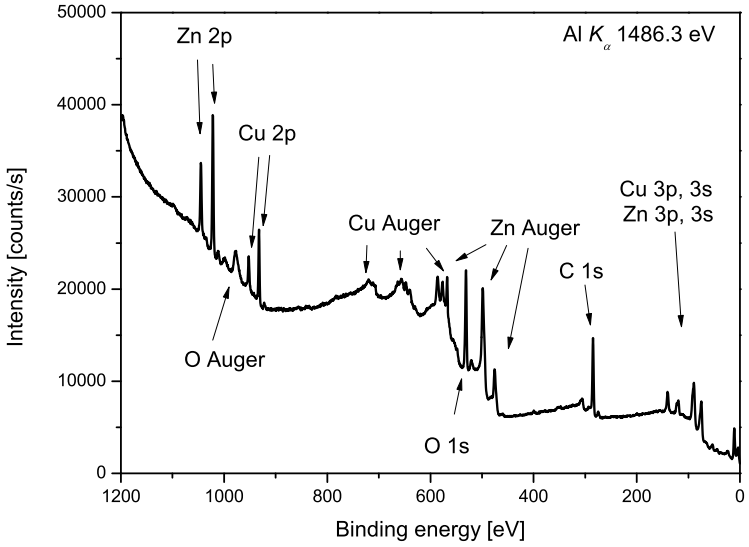

Figure 5.6: The figure shows XPS overview spectrum of the $Cu/ZnO/Al_2O_3$ catalyst reduced at 0.3 bar H_2 for 16 h. The spectrum is obtained using Alk_α x-rays.

treatment pressures of hydrogen.

The positions of all auger peaks are aligned by the C 1s peak. A Shirley background is subtracted from the $L_3M_{4,5}M_{4,5}$ Auger peak and the peak is normalized to the peak height of the ZnO feature. The lowest lying black curve represents the oxidized catalyst with increasing partial pressure of hydrogen in the pretreatment moving upwards in the curves. The Auger peak for ZnO and metallic Zn is separated by 3 eV according to the Wagner Plot captured from NIST seen in fig. 5.7(b). The Wagner Plot shows the relationship between the $2p_{3/2}$ XPS peak and the kinetic energy of the Zn and ZnO $L_3M_{4,5}M_{4,5}$ auger electron. The Wagner Plot further displays the Modified Auger Parameter which is the sum of kinetic energy of the auger electron and binding energy of photoelectron. In fig. 5.7(a) a shoulder feature is present at approximately 495 eV for the reduced catalyst and becomes more pronounced for higher hydrogen pressure. The shoulder feature appearing as a consequence of the pretreatment in fig. 5.7(a) is assigned to originate from metallic Zn in the catalyst.

To ensure the zinc in the $Cu/ZnO/Al_2O_3$ catalyst is fully oxidized, the catalyst is compared to ZnO reference. The reference sample is made from a 100 % pure ZnO powder which is pressed into a pellet and mounted the sample holder in the HPC. The ZnO pellet is transferred to vacuum and annealed to 120°C to remove water. After being cooled to

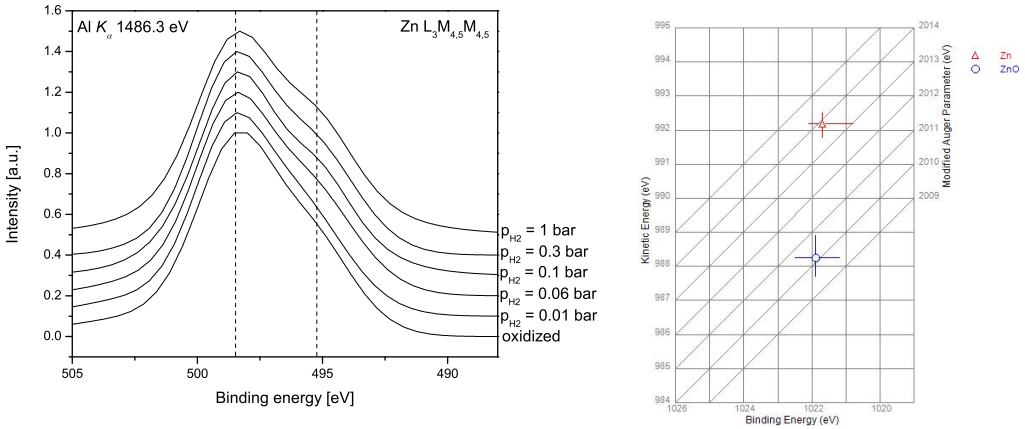

(a) (b)

Figure 5.7: Fig. a shows the auger Zn $L_3M_{4,5}M_{4,5}$ peak for the industrial $Cu/ZnO/Al_2O_3$ catalyst for increasing hydrogen reduction pressure. The black curve represents the non-reduced oxidized catalyst. Fig. b shows the Wagner Plot for Zn and ZnO obtained from NIST. The plot shows that a 3 eV separation between the Zn and ZnO should be observed.

room temperature the ZnO sample is analyzed by XPS. The sample is then transferred back to the HPC and reduced at 1 bar hydrogen for 16 h at 220°C. In fig. 5.8 the ZnO_x Auger peak is shown for the ZnO powder and for the $Cu/ZnO/Al_2O_3$ catalyst before and after reduction.

The figure compares the ZnO to the $Cu/ZnO/Al_2O_3$ catalyst exposed to the same pretreatment. The shape and position of the Auger peak from ZnO and the oxidized industrial $Cu/ZnO/Al_2O_3$ catalyst appear to be similar, indicating that the zinc in the industrial catalyst is fully oxidized (red and green dashed line). Furthermore, no change in the Auger peak for the ZnO pellet is observed before and after reduction, providing clear evidence of the importance of copper for the reduction of ZnO to metallic Zn. In contrast, a clear change is seen for the industrial $Cu/ZnO/Al_2O_3$ catalyst for a pretreatment in 1 bar hydrogen.

The amount of metallic Zn on the reduced $Cu/ZnO/Al_2O_3$ catalyst is quantified by fitting of the $L_3M_{4,5}M_{4,5}$ Auger peak. The reference ZnO peak is used in a linear combination as:

$$\text{Fit} = C_1 \cdot \text{ZnO} + C_2 \cdot \text{ZnO}_{-3\text{eV}} \tag{5.7}$$

where C_1 and C_2 is the factor multiplied to the peak to obtain the best fit. In fig. 5.9 the zinc Auger peak for the $Cu/ZnO/Al_2O_3$ catalyst reduced at 1 bar hydrogen (red dots) for

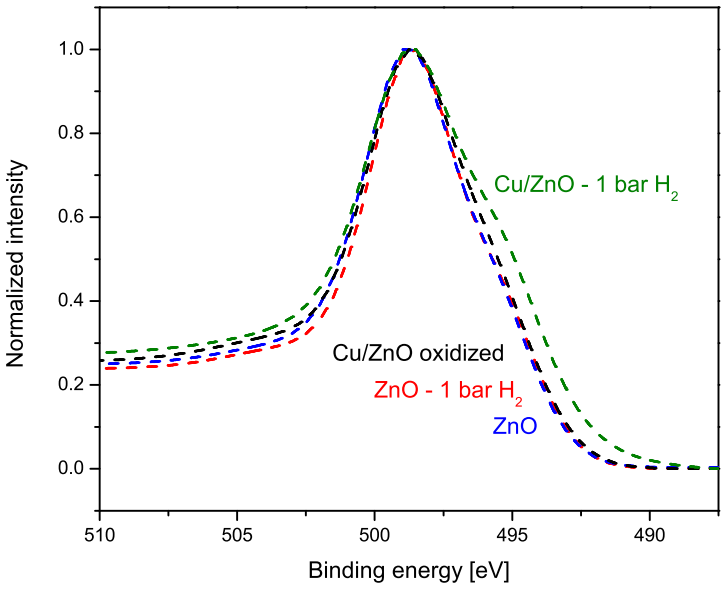

Figure 5.8: The figure shows the ZnO_x auger peak from: A: a 100 % ZnO powder, B: a 100 % ZnO powder reduced at 1 bar H_2 for 16 h, C: The oxidized $Cu/ZnO/Al_2O_3$ catalyst and D: The $Cu/ZnO/Al_2O_3$ catalyst reduced at 1 bar H_2 for 16 h.

16 h is shown together with the linear combination (grey and light grey curve) and the fit (black dots). The fit is an addition of the two filled curves and is solved until the best fit of the reduced catalyst is obtained. This procedure is executed on the measured Auger peak for all reduced catalysts in fig. 5.7(a) and the areas of each of the curves are quantified.

The Auger peaks are fitted as a linear combination of the oxidized Auger peak and the oxidized Auger peak shifted 3 eV downwards in binding energy. A deconvolution of the fit allows for a quantification of the peak areas assigned to metallic Zn and ZnO and thereby determine the extent of metallic Zn in the surface layers of the catalyst. In fig. 5.10 the change in area of the Zn and ZnO is shown for different pretreatment conditions for both the $Cu/ZnO/Al_2O_3$ catalyst and the pure ZnO reference. The change in Zn and ZnO signals are measured as the relative change in area compared to the as received oxidized sample. Figure 5.10 shows a gradual enrichment of metallic Zn for the $Cu/ZnO/Al_2O_3$ catalyst, up to 10% depending on the pressure of hydrogen in the pretreatment. A reference ZnO sample is exposed to 1 bar of H_2 and no metallic Zn was measured. These measurements demonstrate the importance of copper for catalyzing the reduction of ZnO.

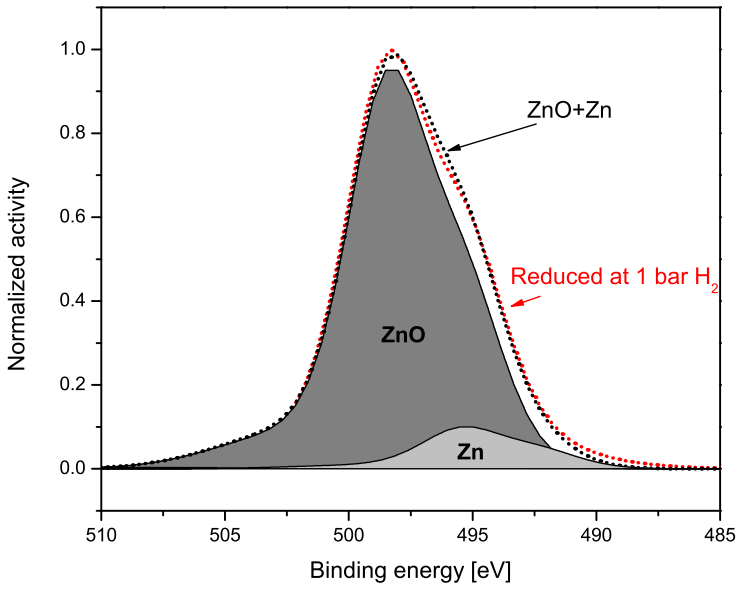

Figure 5.9: The figure shows the fitting of the reduced ZnO_x auger peak. The fitting is a linear combination of the oxidized auger peak and oxidized auger peak shifted 3 eV downwards in binding energy. The area of the two peaks is quantified.

Together with the reduction of ZnO, the reduction of Cu was also investigated. In fig. 5.11(a) the L_3VV Auger line for Cu is presented for the oxidized $Cu/ZnO/Al_2O_3$ catalyst and for the catalyst reduced under varying hydrogen pressures. In fig. 5.11(b) the Cu2p peak and the L_3VV Auger peak for the three oxidation states of copper are shown. The Cu2p peak changes drastically for CuO to metallic Cu and Cu_2O by having a large shake up feature for both the $Cu2p_{3/2}$ and $Cu2p_{5/2}$ at 945.5 eV and 970.9 eV respectively. For an analysis of the Cu2p solely the Cu_2O peak and the metallic Cu can be difficult to distinguish. The Auger peaks of the three Cu oxidation states are from fig. 5.11(b) are separated making them easier to distinguish.

The $Cu/ZnO/Al_2O_3$ catalyst is reduced to metallic Cu already at the first pretreatment step in 0.01 bar hydrogen. Fig. 5.11(a) provides clear evidence that only relative mild reduction conditions are needed to obtain copper in the metallic state. For higher hydrogen pressure the copper Auger line do not change position or shape. The position of the Auger peak for the oxidized $Cu/ZnO/Al_2O_3$ catalyst do not fit perfectly with either the CuO or Cu_2O shift reported in [88], indicating that the oxidized catalyst surface contains both CuO and Cu_2O. This statement is further supported by an analysis of the Cu2p peak.

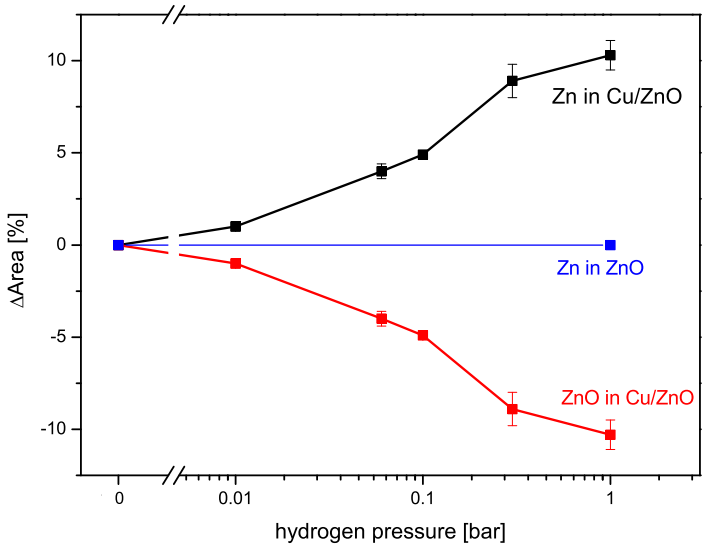

Figure 5.10: The figure shows the change in area of the ZnO (red) and Zn (black) Auger peak for the industrial $Cu/ZnO/Al_2O_3$ catalyst and for the change in area for the ZnO reference (blue).

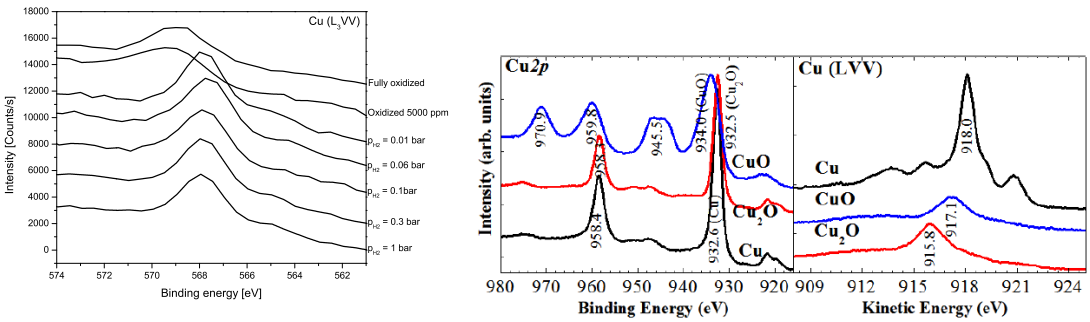

(a) (b)

Figure 5.11: Figure a: The figure shows the change in the Cu L_3VV auger line for the industrial $Cu/ZnO/Al_2O_3$ catalyst for different reduction pressures. Figure b shows Cu2p and the L_3VV Auger peak for the three oxidation states of copper measured by XPS. Captured from [88].

In fig. 5.12(b) the area analysis of the Cu2p and Zn2p peaks is shown. For the oxidized $Cu/ZnO/Al_2O_3$ catalyst the Cu2p peak clearly has the shake up feature as seen for CuO in fig. 5.11(b). As for the Auger peak, Cu is fully reduced to the metallic Cu state at the first pretreatment step in 0.01 bar hydrogen. In fig. 5.12(b) two point of the oxi-

dized $Cu/ZnO/Al_2O_3$ are presented representing the catalyst as received and as oxidized in 5,000 ppm O_2/Ar for 16 h. The size of the shake up feature for the as received catalyst is much bigger than for the catalyst oxidized at 5000 ppm O_2 and is therefore marked as fully oxidized. Having a smaller shake up feature for the fully oxidized catalyst indicates a surface of mixed oxidation states.

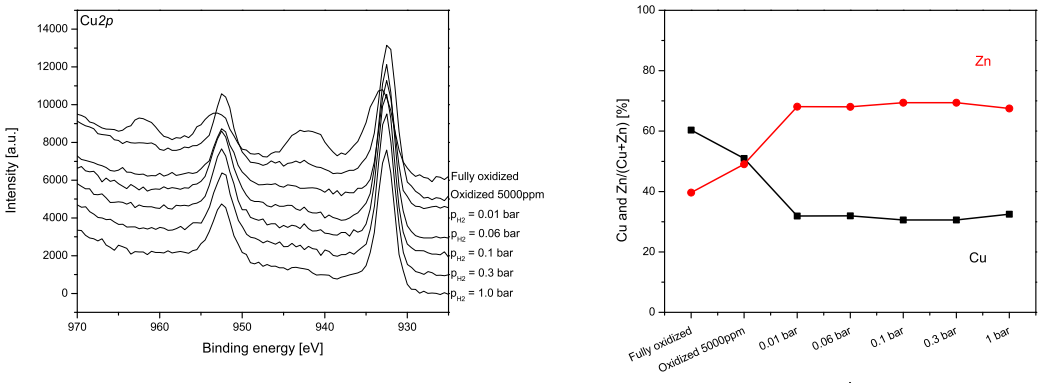

(a) (b)

Figure 5.12: The figure shows the area analysis of the Cu2p and the Zn2p as a function of the hydrogen pressure during the pretreatment.

The large change in the surface area of Cu and Zn is related to the appearance of the shake up peak for the Cu2p peak. For the oxidized samples the area of copper peak is much larger than zinc whereas the ratio changes completely when the catalyst is reduced during pretreatment. The area of the peaks for Cu and Zn for the reduced samples is the same for all partial pressures of hydrogen during the 16 h pretreatment.

5.4 Discussion

The surface area of copper on the $Cu/ZnO/Al_2O_3$ catalyst is determined by the three adsorption methods previously described. The copper area measured by the three methods after a pretreatment in different partial pressures of hydrogen is shown in fig. 5.13. The Cu area is determined by both the H_2-TPD, N_2O-RFC and H_2-TA methods and is evaluated as the area of the Cu surface per catalyst weight.
Subsequent to a pretreatment in 0.01 bar of hydrogen, the N_2O titration method and the H_2-TPD return essentially the same Cu area of around 16.5 m^2/g. H_2-TA gives a slightly lower area (-13%) due to incomplete reduction of Cu_2O as described in sec. 5.2.3. The Cu area determined by N_2O-RFC is observed to increase with the partial pressure of hydrogen except for the pretreatment in 0.05 bar hydrogen. The surface area of the same catalyst determined by H_2-TPD and H_2-TA is observed to decrease as a function of the hydrogen

partial pressure. Despite the relative low pressures of hydrogen during pretreatment, the impact on the surface area determined with the three different methods are substantial i.e. up to ±60-65%. Note that the average of the surface area based on the N_2O-RFC and H_2-TPD displayed in fig. 5.13 is approximately a constant independent of the pretreatment.

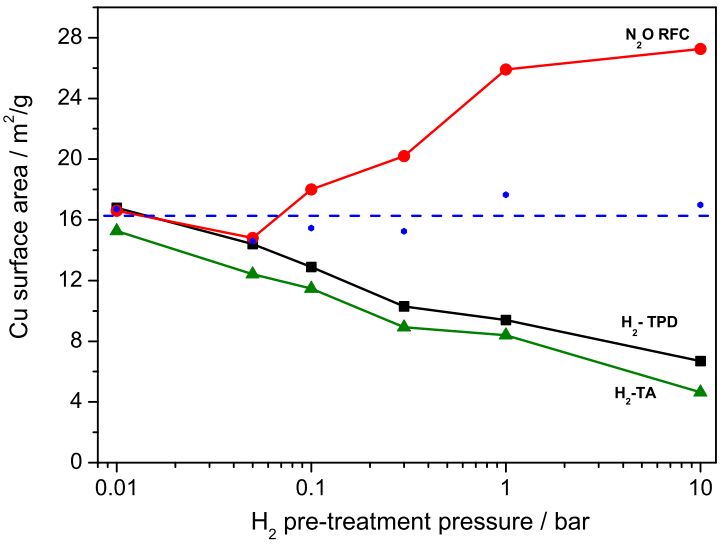

Figure 5.13: The figure shows the change in Cu surface area as determined by N_2O-RFC (red), H_2-TPD (black) and H_2-TA (green) by applying a pretreatment in different partial pressures of H_2 for 16 h. The average of the Cu areas determined using H_2-TPD and N_2O-RFC are plotted with blue dots. The blue dashed line is to guide the eye.

The measurements of the Cu surface area by N_2O-RFC and H_2-TPD deviate to an increasing extent as the partial pressure of H_2 is raised during the pretreatment as seen in fig. 5.13. The Cu area determined by N_2O-RFC is relying on the assumption that Cu is only present in the metallic state. Hence, the Cu surface is solely responsible for the oxygen adsorption during the N_2O decomposition. However, the oxidation process is not selective in its nature. The incorporation of the reduced Zinc atoms found by XPS in the surface of the copper nanoparticles will increase the oxygen uptake from N_2O as a Zn atom incorporated into the Cu surface is expected to react with one N_2O molecule while a surface Cu atom only reacts with 0.5 N_2O molecule.

5.4.1 Geometric model

In an attempt to link the measured copper area from the three adsorption methods to the spectroscopy data a simple geometric model is made. The model relies on a number of assumptions to give a quantitative measure of the surface composition. The microscopic morphology of the industrial type methanol synthesis catalyst can in general be considered as an agglomeration of spherical nanoparticles alternately consisting of Cu and Zn. In an idealized picture, the catalyst tablet is constructed by identical arrays of nanoparticles each representing the overall element distribution. This assumption enables the overall element composition of the catalyst is due to rotational symmetry to be represented by a half sphere of a particle array.

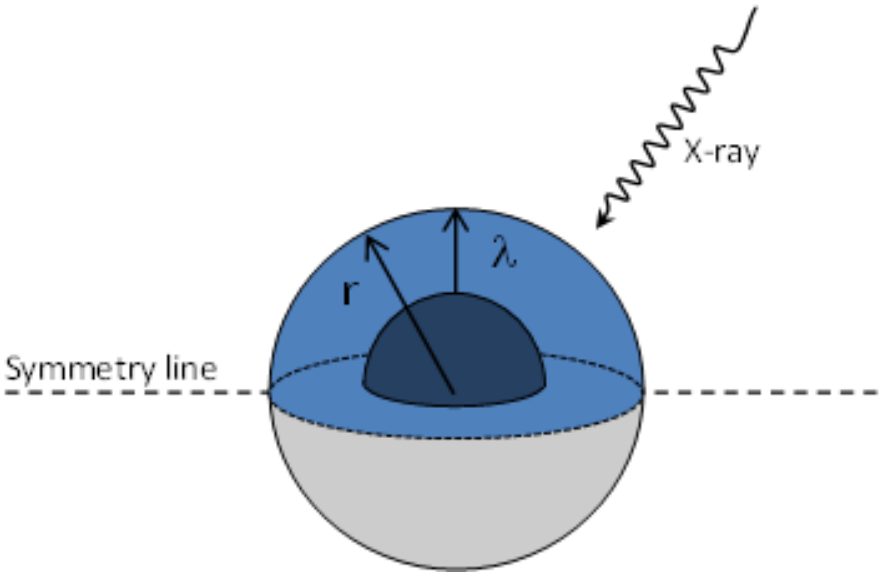

Figure 5.14: The figure shows the principle of the geometric model converting the XPS signal to a copper surface area. The mean free path of the electrons causes XPS only to probe a fraction of the volume of nanoparticles in the catalyst.

The probing depth of the XPS technique is limited to the inelastic mean free path of the induced photoelectron in the analyzed matter. The probing depth is generally limited to a few Å. This means that the XPS data only contains information of the elemental configuration of the nanoparticle surface.
The fraction of the particle which is analyzed by XPS is given by the ratio between the volume of the rim divided by the volume of the spherical cap and is expressed by the following equation:

$$\frac{V_{\text{rim}}}{V_{\text{half sphere}}} = \frac{r^3 - (r-\lambda)^3}{r^3} \tag{5.8}$$

Where r is the radius of the nanoparticle and λ is the inelastic mean free path. By X-Ray Diffraction (XRD) of the catalyst, the average particle size of the ZnO particles is estimated to 90 Å. The inelastic mean free path of the analyzed electrons can be calculated by the TPP-2M formula [89] to be 8.77 Å in ZnO and 7.46 Å in metallic Zn using the Zn $2p_{3/2}$ peak and Al$K\alpha$ line. This results in an analyzed particle fraction of 0.48. The density of Zn atoms per gram of catalyst weight can be derived from the overall Zn content (25 mol%) and the molar weight of Zn times Avogadro's number. The number of reduced Zn atoms, as a function of the pretreatment, is calculated based on the XPS data and corrected by the analyzed particle fraction. By assuming that each Zn atom is incorporated into the surface of the Cu particles, applying an "atoms per unit area" of surface of 1.46×10^{19} Zn atoms m^{-2} identical to Cu, the apparent Zn surface area can be evaluated. The corresponding Cu area is calculated by subtracting the Zn area from the reference Cu area.
The assumed XPS probing depth depending on the inelastic mean free path of the electron of the ZnO particles is shown in the illustration in fig. 5.14. The model relies on spherical particles being probed.

5.4.2 Surface alloy

The observations of a deviating copper surface area determined by the selective H_2-TPD and non-selective N_2O-RFC methods combined with the observed formation of metallic Zn by XPS with increasing partial pressure of H_2 during pretreatment strongly suggests a surface alloying of copper and zinc. Previous STM studies of Zn deposition on Cu(111) single crystals have shown that a Cu-Zn surface alloy is formed by random substitution of the Zn atoms homogeneously into the Cu(111) surface layer [90][91]. The fact that metallic Zn is observed by XPS provides strong evidence that ZnO is reduced into metallic Zn at the interface between the Cu and ZnO particles followed by the formation of a Cu-Zn surface alloy [92][93]. The formation of a Cu-Zn surface alloy is additionally supported by the data in fig. 5.13.

Contrary to the data of the N_2O-RFC, the H_2-TPD peak decreases with increasing p_{H2} during the pretreatment. The H_2-TPD method is based on the specific desorption profile associated with only metallic Cu. Hence, incorporation of reduced Zn at the surface of the Cu particles decreases the Cu area measured by the H_2-TPD method. Density Functional Theory, DFT, calculations show that the hydrogen adsorption energy at Zn sites incorporated in a Cu(111) surface will decrease by 28 kJ/mol compared to that at a clean

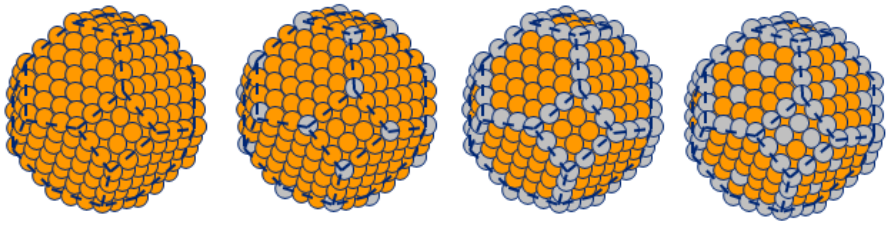

Figure 5.15: The ball model shows the purposed mechanism of surface alloying of copper and zinc subsequent to pretreatment.

Cu(111) surface. The DFT calculations are made by Poul Georg Moses from Haldor Topsoe. The calculations are carried out using the DACAPO code on a 2x2 (111) surface with a thickness of 3 atomic layers allowing only the upper layer to relax. H adsorption energies are calculated on the possible high symmetry sites on a pure Cu slab and on a Cu slab with 50% of the top layer Cu atoms substituted with Zn. The hydrogen adsorption energy means that the reduction in the peak area of the H_2-TPD can be directly assigned to a loss of Cu surface area and show that Zn is incorporated into the surface of the Cu particles. An illustration of the progressive Cu-Zn alloy formation is shown schematically in fig. 5.15.

The data in fig. 5.13 enables the quantification of metallic Zn in the Cu-Zn surface alloy. The change in observed surface area relative to that measured after the pretreatment in 10 mbar H_2 is interpreted as a change in Zn/Cu element ratio in the surface of the Cu particles. In fig. 5.16 the ratio of Zn in the Cu surface is evaluated for the H_2-TPD and the N_2O-RFC experiment, respectively. The zinc enrichment in the copper surface as a function of the pretreatment is seen to be similar even though two independent techniques are applied. This fact further supports the explanation of a Cu-Zn surface alloy formation. The Zn enrichment in the Cu surface is observed to reach 60% for a 16 h pretreatment in 10 bar H_2. This observation is remarkable taking into account the relative mild conditions applied during the pretreatment. Another interesting observation is that the average surface area measured by N_2O-RFC and H_2-TPD is approximately independent of the hydrogen pretreatment pressure. This indicates that the total geometric surface area of the Cu particles is virtually unchanged during the reduction process perhaps because wetting of particles of similar size does not strongly change the exposed surface area.

The amount of hydrogen which is used for establishing the equilibrium coverage is extracted from the H_2-TPD measurement. In fig. 5.17 is the Cu surface area determined by H_2-TPD plotted against the area determined by the H_2-TA consumption profile after the correction. By linear regression the area determined by H_2-TA is underestimated by 12.3% compared the H_2-TPD. Consecutive N_2O-RFC and H_2-TA loops have shown that the Cu_2O surface is in fact only partially reduced during the H_2-TA experiment. The experiment showed that approximately 80% of the adsorbed oxygen is removed at the applied experimental

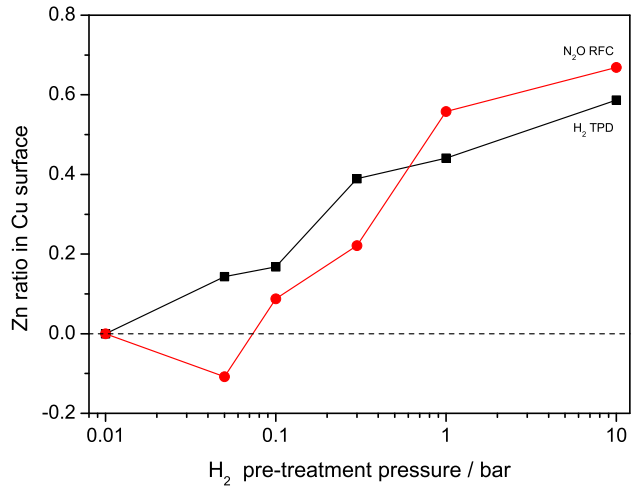

Figure 5.16: The figure shows ratio of Zn enrichment in the Cu surface evaluated for both the N_2O-RFC and H_2-TPD technique.

conditions, which is in line with the analysis in fig. 5.17.

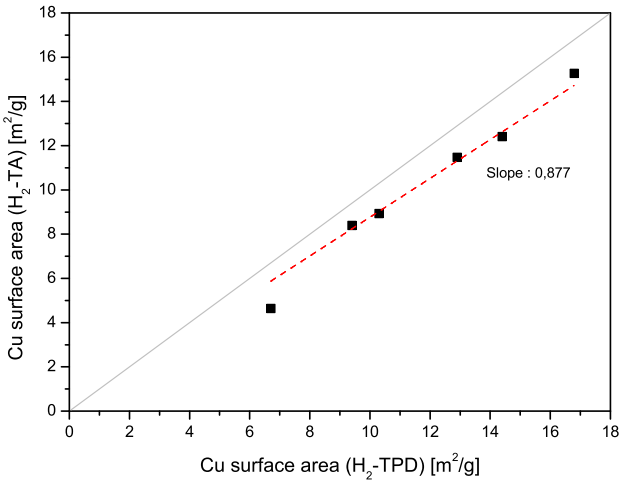

Figure 5.17: The graph shows the Cu surface area determined by H_2-TPD plotted against the Cu area derived from the corrected H_2 consumption during H_2-TA experiment. The linear regression shows that the H_2-TA experiment underestimates the Cu area by 12.3%.

The formation of Cu-Zn alloy is supported by bridging the XPS data and the Cu area

determined by H_2-TPD through a simple geometric model. In the geometric model described, the fraction of reduced and oxidized Zn is used and it is assumed that each metallic Zn atom replaces a Cu surface atom. Fig. 5.18 displays the specific Cu surface area as a function of the H_2 pretreatment pressure for XPS as calculated by the simple geometric model and evaluated by H_2-TPD assuming that the latter probes the Cu surface atoms. The nice correlation between the metallic Zn measured by XPS and the decrease in Cu surface area determined by H_2-TPD seen from the graph in fig. 5.18, lends credit to H_2-TPD as an accurate method for determining the specific Cu (Zn free) surface area.

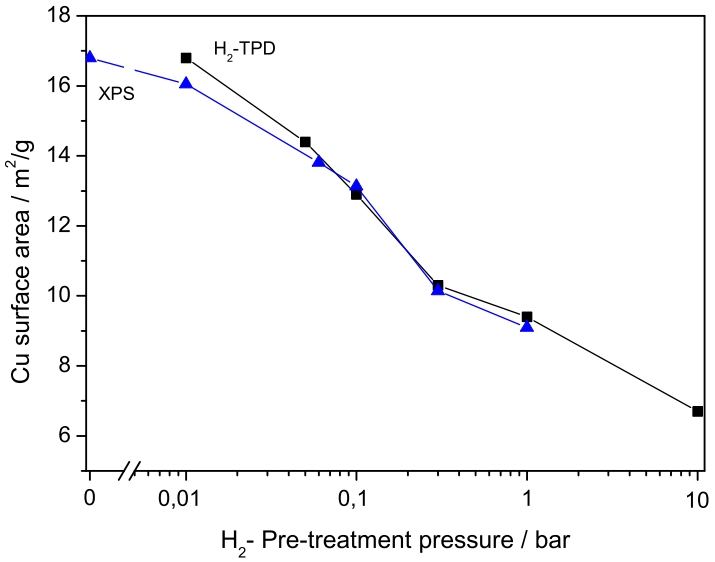

Figure 5.18: The figure shows the correlation between the Cu surface areas determined by H_2-TPD and the Cu surface area based on the XPS data derived by the geometric model. The black line corresponds to the area determine by H_2-TPD and the blue line by XPS.

5.5 Summary

In summary, the combined study of XPS, H_2-TPD, N_2O-RFC and H_2-TA, has provided clear evidence of a surface decoration of metallic Zn present on the Cu particle surface. Combining the methods elegantly gives insight to the debated origin of surface ZnOx species. Subsequent to different pretreatment, XPS clearly showed an enhancement of the metallic Zn feature in the $L_3M_{4,5}M_{4,5}$ Auger peak increasing with the partial pressure of H_2. The presence of copper particles was found to be essential for reducing ZnO. Complementary surface sensitive methods in the case of N_2O titration showed an increase in

the oxygen uptake from nitrous oxide while secondary H_2-TA and the H_2-TPD experiments showed a decrease in adsorbed and desorbed hydrogen, respectively. The experimental observations were consistent with the formation of a Cu-Zn surface alloy formation during the pretreatment. The interplay between the evaluated surface areas of the N_2O-RFC and H_2-TPD techniques can be utilized to quantify the amount of metallic Zn in the Cu surface. This study provides a reinterpretation and a more accurate determination of the specific Cu surface determination based on specific area measurements of four independent techniques.

Chapter 6

Summary and Conclusion

The thesis presented has been divided into five chapters. The first chapter served as an introduction to the field of heterogeneous catalysis and described the future challenges in finding sustainable replacements for fossil fuels. Methanol was mentioned as being one of the most promising alternatives, with potential for its synthesis from a combination of solar power, industrial exhaust waste, and sea water.
The second chapter concerned the experimental setup used as frameset for the Ph.d. project. The methods available and utilized during the projects were presented and discussed giving the fundamental insight needed in order to discuss the presented results.
The third chapter was an experimental investigation into the nature of the active sites for dissociation of CO on ruthenium. The project was a collaborative work between three UHV-facilities, each with different unique strengths within surface science. The project bridged the gap between CO desorption from ruthenium single crystals and nanoparticulate ruthenium. The main conclusions from the project were:

1. 1. Inducing or suppressing step sites on a ruthenium single crystal by sputtering or poisoning respectively proved to influence the dissociation of CO, with the conclusion that CO dissociation is sensitive to the structure of the Ru surface.

2. CO dissociative adsorption was by CO TPD found to occur at step sites whereas the CO was molecularly adsorbed on the terraces.

3. The crossover in CO desorption from a Ru single crystal and ruthenium nanoparticles was bridged. Sputtering a Ru single crystal led to desorption features similar to nanoparticles. Equally, annealing nanoparticles led to a desorption spectra similar to that obtained from the single crystal.

The fourth chapter was a surface scientific project on a model Cu/Ru system. The project was a collaborate work between a UHV-facility and a heterogeneous catalysis lab testing real catalysts in a plug flow reactor. The project was the story of how the fundamental knowledge obtained from model systems in surface science studies can contribute to the design of real catalyst. The important conclusion from the investigation of the Cu/Ru system was:

1. A model system of a Cu overlayer on a Ru thinfilm was proven to be more active

compared to both Cu and Ru towards ammonia oxidation.

2. The counterintuitive behavior of the system was explained by a straining of the Cu surface layer shifting the d-band downwards in energy.

3. 3. The Cu/Ru system was applied to a high surface area support and was found to exhibit a higher activity than Cu and Ru.

The fifth and final chapter was a study of the pretreatment of an industrial type methanol catalyst. The project was conducted in collaboration with Sebastian Kuld from Haldor Topsoe. The project concerned the characterization of the surface by means of three adsorption methods and one spectroscopy method. Linking the four methods gave a consistent explanation of the surface after a pretreatment in hydrogen. The most conspicuous results from the study were:

1. The H_2-TPD and H_2-TA experiments provided a copper surface area that deviated from the N_2O-RFC measurement.

2. XPS experiments explained the dynamical change by a surface alloying of Cu and Zn.

3. A reinterpretation of the methods used to determine the Cu surface area is needed.

4. A direct quantification of the specific Cu and Zn areas are possible independently is needed.

The three projects presented have proven how it is possible to manipulate the reactivity of both model systems but also real catalysts. Depending on the reaction probed, nanoscale catalysts have thoroughly been investigated and optimized for the given reaction. The three projects concerned three different approaches of optimizing a catalyst, either by special sites, overlayers or by surface alloying. In all cases insight to better catalysts were given.

Bibliography

[1] BP statistical review of world energy 2013. www.BP.com.

[2] S. Dahl and I. Chorkendorf. Solar Fuel Generation: Towards practical implementation. *Nature materials*, 11:100–101, FEB 2012.

[3] Catalyst challenges. www.case.dtu.dk.

[4] Olah G. Beyond oil and gas: The methanol economy. *Angewandte Chemie International Edition*, 44:2636–2639, 2005.

[5] Olah G. Towards oil independence through renewable methanol chemistry. *Angewandte Chemie International Edition*, 52:104–107, 2013.

[6] I. Chorkendorff and J. W. Niemantsverdriet. *Concepts of Modern Catalysis And Kinetics*. Wiley-VCH Verlag GmbH and Co., 2003.

[7] B. Hammer, J. K. Norskov. Why gold is the noblest of all the metals. *Nature*, 376:238–240, JUL 2002.

[8] T. Bligaard and J. K. Nørskov. Ligand effects in heterogenous catalysis and electrochemistry. *Electrochimica Acta*, 52:5512–5516, FEB 2007.

[9] A Ozaki and K Aika. *Catalysis: science and technology*, volume 1. Springer-Verlag, 1981.

[10] P Stoltze H.L Skriver A Ruban, B Hammer and J. K. Nørskov. Surface electronic structure and reactivity of transition and noble metals. *Journal of Molecular Catalysis A: Chemical*, 115(3):421–429, FEB 1997.

[11] J. Greeley, I. E. L. Stephens, A. S. Bondarenko, T. P. Johansson, H. A. Hansen, T. F. Jaramillo, J. Rossmeisl, I. Chorkendorff, and J. K. Norskov. Alloys of platinum and early transition metals as oxygen reduction electrocatalysts. *Nature Chemistry*, 1(7):552–556, OCT 2009.

[12] A. V. Ruban, H. L. Skriver, and J. K. Nørskov. Surface segregation energies in transition-metal alloys. *Physical Review B*, 59(24):15990–16000, JUN 1999.

[13] U Diebold. The surface science of titanium dioxide. *Surface Science Reports*, 48(5-8):53–229, 2003.

[14] G. A. Somorjai. *Chemistry in Two Dimensions, Surfaces.* Cornell University Press, Ithaca, 1981.

[15] I. Chorkendorff. Experimental surface physics: Lecture notes for the experimental surface physics course on dtu. 2003.

[16] Johansson M., Jørgensen J. H., Chorkendorff I. Combined high-pressure cell ultrahigh vacuum system for fast testing of model metal alloy catalysts using scanning mass spectrometry. *Rev. Sci. Instrum.*, 75(6):2082–2093, JUN 2004.

[17] Johansson M., Lytken O., Chorkendorff I. Design parameters for measurements of local catalytic activity on surfaces. *Appl. Surf. Sci.*, 252:3673–3685, 2006.

[18] H. Schulz. Short history and present trends of Fischer Tropsch synthesis. *Applied Catalysis A: General*, 186:3–12, 1999.

[19] H. Pfnür, P. Feulner, and D. Menzel. *Journal of Chemical Physics*, 79:4613–4623, 1983.

[20] Ellen D. Williams and W.H. Weinberg. The geometric structure of carbon monoxide chemisorbed on the ruthenium (001) surface at low temperatures. *Surface Science*, 82(1):93–101, 1979.

[21] G. Michalk, W. Moritz, H. Pfnür, and D. Menzel. *Surface Science*, 129:92–106, 1983.

[22] T. Zubkov, G. A. Morgan, and J. T. Yates. *Chemical Physics Letters*, 362:181–184, 2002.

[23] Yann Tison, Kenneth Nielsen, Duncan J. Mowbray, Lone Bech, Christian Holse, Federico Calle-Vallejo, Kirsten Andersen, Karsten W. Mortensen, Jens J. Jacobsen, and Jane H. Nielsen. Scanning Tunneling Microscopy Evidence for the Dissociation of Carbon Monoxide on Ruthenium Steps. *Journal of Physical Chemistry C*, 116(27):14350–14359, JUL 12 2012.

[24] D. W. Goodman. Model catalytic studies over metal single-crystals. *Accounts of Chemical Research*, 17:194–200, 1984.

[25] R.D. Kelley and D.W. Goodman. Catalytic methanation over single crystal nickel and ruthenium - reaction-kinetics on different crystal planes and the correlation of surface carbide concentration with reaction-rate. *Surface Science*, 123:743–749, 1982.

[26] I.N. Remediakis T. Bligaard G. Jones J. Engbæk O. Lytken S. Horch J.H. Nielsen J. Sehested J.R. Rostrup-Nielsen J.K. Nørskov M.P. Andersson, E. Abild-Pedersen and I. Chorkendorff. Structure sensitivity of the methanation reaction: H2-induced co dissociation on nickel surfaces. *Journal of Catalysis*, 255:6–19, 2008.

[27] T. Zubkov, G. A. Morgan, J. T. Yates, O. Kühlert, M. Lisowski, R. Schillinger, D. Fick,

and H. J. Jänsch. *Surface Science*, 526:57–71, 2003.

[28] Søren B. Vendelbo, Martin Johansson, , Jane H. Nielsen, and Ib Chorkendorff. *Physical Chemistry Chemical Physics*, 13:4486–4493, 2011.

[29] H.J. Freund M. Mavrikakis, M. Baumer and J.K. Nørskov. Structure sensitivity of co dissociation on rh surfaces. *Catalysis Letters*, 81:153–156, 2002.

[30] S. Dahl, E. Törnqvist, and I. Chorkendorff. Dissociative adsorption of n2 on ru(0001): A surface reaction totally dominated by steps. *Journal of Catalysis*, 192(2):381–390, 2000.

[31] Søren Bastholm Vendelbo. *Structure Sensitivity of CO Dissociation and the Methanation Reaction on a Ruthenium Single Crystal.* PhD thesis, Technical University of Denmark (DTU), 2010.

[32] G Rangelov L Surnev and G Bliznakov. Interaction of oxygen with a Ru(0001) surface. *Surface Science*, 159(2-3):299–310, 1985.

[33] E. Shincho, C. Egawa, S. Naito, and K. Tamaru. *Surface Science*, 149:1–16, 1985.

[34] S. B. Vendelbo, M. Johansson, D. J. Mowbray, M. P. Andersson, F. Abild-Pedersen, J. H. Nielsen, J. K. Nørskov, and I. Chorkendorff. *Topics in Catalysis*, 53:357–634, 2010.

[35] T. Zambelli, J. Wintterlin, J. Trost, and G. Ertl. Identification of the active sites of a surface-catalyzed reaction. *Science*, 273(5282):1688–1690, 1996.

[36] Murphy S. Nielsen R. M. Nielsen J. H. Strebel, C. and I. Chorkendorff. Probing the active sites for co dissociation on ruthenium nanoparticles. *Physical Chemistry Chemical Physics*, 14(22):8005–8012, 2012.

[37] J. Gavnholt and J. Schiøtz. *Physical Review B*, 77:035404, 2008.

[38] S. Murphy, C. Strebel, S. B. Vendelbo, C. Conradsen, Y. Tison, K. Nielsen, L. Bech, R. M. Nielsen, M. Johansson, I. Chorkendorff, and J. H. Nielsen. *Physical Chemistry Chemical Physics*, 13:10333–10341, 2011.

[39] R. M. Nielsen, S. Murphy, C. Strebel, M. Johansson, J. H. Nielsen, and I. Chorkendorff. *Surface Science*, 603:3420–3430, 2009.

[40] M. Gsell P. Jakob and D. Menzel. Interactions of adsorbates with locally strained substrate lattices. *The Journal of Chemical Physics*, 114(22):10075–10085, 2001.

[41] B. Hammer M. Mavrikakis and J. K. Nørskov. Effect of strain on the reactivity of metal surfaces. *Physical Review Letters*, 81(13):2819–2822, 1998.

[42] Lu Gang, B. G. Anderson, J. van Grondelle, R. A. van Santen, W. J. H. van Gennip, J.

W. Niemantsverdriet,. P. J. Kooyman, A. Knoester, and H. H. Brongersma. Alumina Supported Cu Ag Catalysts for Ammonia Oxidation to Nitrogen at Low Temperature. *Journal of Catalysis*, 206:60–70, 2002.

[43] M. Amblard, R. Burch, B.W.L. Southward. The selective conversion of ammonia to nitrogen on metal oxide catalysts under strongly oxidising conditions. *Applied Catalysis B: Environmental*, 22:159–166, 1999.

[44] M. de Boer, H. M. Huisman, R.J.M. Mos, R.G. Leliveld, A.J. van Dillen, J.W. Geus. Selective oxidation of ammonia to nitrogen over SiO2- supported MoO3 catalysts. *Catalysis Today*, 17:189–200, 1993.

[45] A. Wollner, F. Lange, H. Schmelz, H. Kniizinger. Characterization of mixed copper-manganese oxides supported on titania catalysts for selective oxidation of ammonia. *Applied Catalysis A*, 94:181–203, 1993.

[46] J. J. Ostermaier, J. R. Katzer, And W. H. Manogue. Platinum Catalyst Deactivation in Low-Temperature Ammonia Oxidation Reactions. *Journal of Catalysis*, 41:277–292, 1976.

[47] N.N. Sazonova, A.V. Simakov, T.A. Nikoro, G.B. Barannik, V.F. Lyakhova, V.I. Zheivot, Z.R. Ismagilov and H. Veringa. Selective Catalytic Oxidation Of Ammonia To Nitrogen. *React.Kinet.Catal.Lett.*, 57(1):71–79, 1996.

[48] Petra E. de Jongh. Keeping out the oxygen. *Nature Materials*, 11:265–266, 2011.

[49] Rudy W. P. Wagemans, Joop H. van Lenthe, Petra E. de Jongh, A. Jos van Dillen, and Krijn P. de Jong. Hydrogen Storage in Magnesium Clusters: Quantum Chemical Study. *American Chemical Society Journals*, 127:16675–16680, 2005.

[50] Louis Schlapbach and Andreas Zuttel. Hydrogen-storage materials for mobile applications. *American Chemical Society Journals*, 414:353–358, 2001.

[51] S. Brandenberger, O. Krocher, A. Tissler and R. Althoff. The State of the Art in Selective Catalytic Reduction of NOx by Ammonia Using Metal Exchanged Zeolite Catalysts. *Catalysis Reviews*, 50:492–531, 2008.

[52] L.I. Darvell, K. Heiskanen, J.M. Jones, A.B. Ross, P. Simell, A. Williams. An investigation of alumina-supported catalysts for the selective catalytic oxidation of ammonia in biomass gasification. *Catalysis Today*, 81:681–692, 2003.

[53] A. Scheuer, M. Votsmeier, A. Schuler, J. Gieshoff, A. Drochner Æ H. Vogel. NH3-Slip Catalysts: Experiments Versus Mechanistic Modelling. *Top. Catal.*, 52:1847–1851, 2009.

[54] I Chorkendorff S. Dahl S. Bredmose Simonsen, D. Chakraborty. Alloyed Ni-Fe nanoparticles as catalysts for NH3 decomposition. *Applied Catalysis A*, 447:22–31,

AUG 2012.

[55] D.P. Sobczyk,. A.M. de Jong, E.J.M. Hensen and R.A. van Santen. Activation of ammonia dissociation by oxygen on platinum sponge studied with positron emission profiling. *Journal of Catalysis*, 219:156–166, 2003.

[56] N. I. Ilchenko, N. P. Chebotareva and N. V. Shvidak. Oxidation Of Ammonia On Transition Metal Carbides. *Reaction Kinetics and Catalysis Letters*, 3(4):343–349, 1976.

[57] J. A. Rodriguez And C. T. Campbell. A Quantum-Chemical Study Of The Adsorption Of Water, Formaldehyde And Ammonia On Copper Surfaces And Water On Zno(0001). *Surface Science*, 197:567–593, 1988.

[58] van de Kerkhof G. J. C. S., Biemolt W., Jansen A. P. J., van Santen R. A. dissociation of ammonia on a copper surface and the effect of oxygen coadsorption: a quantum-chemical study. *Surface Science*, 284:361–371, 1993.

[59] Astrid Boisen, Soren Dahl, Jens K. Norskov, Claus Hviid Christensen. Why the optimal ammonia synthesis catalyst is not the optimal ammonia decomposition catalyst. *Journal of Catalysis*, 230:309–312, 2005.

[60] K. Christmann, G. Ertl, H. Shimizu. Model studies on bimetallic Cu/Ru catalysts: I. Cu on Ru(0001). *Journal of Catalysis*, 61(2):397–411, 1980.

[61] E Houston, C H F. Peden, D S Blair And D W Goodman. Monolayer And Multilayer Growth Of Cu On The Ru(0001) Surface. *Surface Science*, 167:427–436, 1986.

[62] J.H. Sinfelt, Y.L. Lam, J.A. Cusumano, A.E. Barnett. Nature of ruthenium-copper catalysts. *Journal of Catalysis*, 42:227–237, 1976.

[63] K. S. Kim , J. H. Sinfelt , S. Eder , K. Markert , K. Wandelt. Photoemission studies of physisorbed xenon atoms on ruthenium/copper surfaces. *J. Phys. Chem.*, 91:2337–2342, 1987.

[64] J.T. Yates Jr., C.H.F. Peden, D.W. Goodman. Copper site blocking of hydrogen chemisorption on ruthenium. *Journal of Catalysis*, 94(2):576–580, 1985.

[65] José A. Rodriguez, D. Wayne Goodman. The Nature of the Metal-Metal Bond in Bimetallic Surfaces. *Catalysis Today*, 257:897–903, 1992.

[66] Raevskaya, M.V., Yanson, I.E., Sokolova, I.G. The effect of nickel on interaction in the copper-ruthenium system. *Journal of Catalysis*, 192(2):237–241, 1987.

[67] Cui X., Zhou J., Ye Z., Chen H., Li L., Ruan M., Shi J. Selective catalytic oxidation of ammonia to nitrogen over mesoporous CuO/RuO2 synthesized by co-nanocasting-replication method. *Journal of Catalysis*, 270:310–317, 2010.

[68] George A. Olah, Alain Goeppert and G. K. Surya Prakash. Chemical Recycling of Carbon Dioxide to Methanol and Dimethyl Ether - From Greenhouse Gas to Renewable, Environmentally Carbon Neutral Fuels and Synthetic Hydrocarbons. *J. Org. Chem.*, 74:487–498, 2009.

[69] M. Behrens, F. Studt, I. Kasatkin, S. Kühl, M. Hävecker, F. Abild-Pedersen, S. Zander, F. Girgsdies, P. Kurr, B. L. Kniep, M. Tovar, R. W. Fischer, J. K. Nørskov, R. Schlögl. The Active Site of Methanol Synthesis over Cu/ZnO/Al2O3 Industrial Catalysts. *Science*, 336:893–897, MAY 2012.

[70] R. Naumann d Alnoncourt, X. Xia, J. Strunk, E. Löffler, O. Hinrichsen and M. Muhler. The influence of strongly reducing conditions on strong metal support interactions in Cu/ZnO catalysts used for methanol synthesis. *Phys. Chem. Chem. Phys.*, 8:1525–1538, FEB 2006.

[71] J. D. Grunwaldt, A. M. Molenbroek, N.Y. Topsøe, H. Topsøe, and B. S. Clausen. In Situ Investigations of Structural Changes in Cu/ZnO Catalysts. *Journal of Catalysis*, 194:452–460, MAY 2000.

[72] Y. Kanai T. Kakumoto T. Watanabe J. Nakamura T. Fujitani, M. Saito and T. Uchijima. The role of metal oxides in promoting a copper catalyst for methanol synthesis. *Catalysis Letters*, 25:271–276, JAN 1994.

[73] C. V. Ovesen, B. S. Clausen, J. Schiotz, P. Stoltze, H. Topsøe and J. K. Norskov. Kinetic Implications of Dynamical Changes in Catalyst Morphology during Methanol Synthesis over Cu/ZnO Catalysts. *Journal of Catalysis*, 168:133–142, 1997.

[74] Grunwaldt J. D., Molenbroek A. M., Topsoe N. Y., Topsoe H. and Clausen B. S. In situ investigations of structural changes in Cu/ZnO catalysts. *Journal of Catalysis*, 194(2):452–460, SEP 2000.

[75] Hansen P. L. and Wagner J. B. and Helveg S. and Rostrup-Nielsen J. R. and Clausen B. S. and Topsoe, H. Atom-resolved imaging of dynamic shape changes in supported copper nanocrystals. *Science*, 295(5562):2053–2055, MAR 15 2002.

[76] H. Wilmer and O. Heinrichsen. Dynamical changes in Cu/ZnOAl2O3 catalysts. *Catal. Lett.*, 82:117–122, 2002.

[77] Peter C.K. Vesborg, Ib Chorkendorff, Ida Knudsen, Olivier Balmes, Jesper Nerlov, Alfons M. Molenbroek, Bjerne S. Clausen and Stig Helveg. Transient behavior of Cu/ZnO-based methanol synthesis catalysts. *Journal of Catalysis*, 262:65–72, JAN 2009.

[78] S. Zander, E. L. Kunkes, M. E. Schuster, J. Schumann, G. Weinberg, D. Teschner, N. Jacobsen, R. Schlögl and Malte Behrens. The Role of the Oxide Component in the Development of Copper Composite Catalysts for Methanol Synthesis. *Angewandte Chemie International Edition*, 52:6536–6540, 2012.

[79] E. Tørnqvist B .S Clausen M. Muhler, L. P. Nielsen and H. Topsœ. Temperature-programmed desorption of H_2 as a tool to determine metal surface areas of Cu catalysts. *Catalysis Letters*, 14(3-4):241–249, MAY 1992.

[80] T. Genger, O. Hinrichsen and M. Muhler. The temperature programmed desorption of hydrogen from copper surfaces. *Catalysis Letters*, 59:137–141, MARCH 1999.

[81] C. Baltes, S. Vukojevic, F. Schüth. Correlations between synthesis, precursor, and catalyst structure and activity of a large set of CuO/ZnO/Al2O3 catalysts for methanol synthesis. *Journal of Catalysis*, 258:334–344, AUG 2008.

[82] G.C. Chinchen, C.M. Hay, H.D. Vandervell, K.C. Waugh. The measurement of copper surface areas by reactive frontal chromatography. *Journal of Catalysis*, 103(1):79–86, JAN 1987.

[83] O. Heinrichsen, T. Genger and M. Muhler. Chemisorption of N2O and H2 for the Surface Determination of Copper Catalysts. *Chem. Eng. Technol.*, 23(11):956–959, 2000.

[84] E.D. Batyrev, J.C. vanden Heuvel, J. Beckers, W.P.A. Jansen, and H.L. Castrium. Kinetic Implications of Dynamical Changes in Catalyst Morphology during Methanol Synthesis over Cu/ZnO Catalysts. *Journal of Catalysis*, 229:136–142, 2005.

[85] F. Yang, Y. Choi, J. Hrbek and J. A. Rodriguez. Autocatalytic Reduction of a Cu2O/Cu(111) Surface by CO: STM, XPS, and DFT Studies. *J. Phys. Chem. C*, 114(40):17042–17050, JUL 2010.

[86] H. Wilmer, T. Genger, and O. Hinrichsen. The interaction of hydrogen with alumina-supported copper catalysts: a temperature-programmed adsorption/temperature-programmed desorption/isotopic exchange reaction study. *Journal of Catalysis*, 215:188–198, 2003.

[87] Y.K. Gao, F. Traeger, O. Shekhah, H. Idriss, C. Woll. Kinetic Implications of Dynamical Changes in Catalyst Morphology during Methanol Synthesis over Cu/ZnO Catalysts. *Journal of Colloid and Interface Science*, 338, 2009.

[88] Dahlang Tahir and Sven Tougaard. Electronic and optical properties of Cu, CuO and Cu2O studied by electron spectroscopy. *J. Phys.: Condens. Matter*, 24, 2012.

[89] S.Tanuma, C. J. Powell, D. R. Penn. Calculations of Electron Inelastic Mean Free Paths (IMFPs). *Surface and Interface analysis*, 20:77–89, 1993.

[90] M. Sano, T. Adaniya, T. Fujitani, J. Nakamura. Oxidation of a Zn-deposited Cu(111) surface studied by XPS and STM. *Surf. Sci*, 514:261–266, 2002.

[91] M. Sano, T. Adaniya, T. Fujitani and J. Nakamura. Formation Process of a Cu-Zn Surface Alloy on Cu(111) Investigated by Scanning Tunneling Microscopy. *Journal of*

Physical Chemistry, 106:7627–7633, 2002.

[92] W. P. A. Jansen, J. Beckers, J. C. v. d. Heuvel, A.W. Denier v. d. Gon, A. Bliek, and H. H. Brongersma. Dynamic Behavior of the Surface Structure of Cu/ZnO/SiO2 Catalysts. *Journal of Catalysis*, 8:229–236, 2002.

[93] M. M. Viitanen, W. P. A. Jansen, R. G. Van Welzenis, and H. H. Brongersma. Cu/ZnO and Cu/ZnO/SiO2 Catalysts Studied by Low-Energy Ion Scattering. *J. Phys. Chem. B*, 103:6025–6029, 1999.

Included papers

PCCP

Dynamic Article Links

Cite this: *Phys. Chem. Chem. Phys.*, 2011, **13**, 10333–10341

www.rsc.org/pccp

PAPER

Probing the crossover in CO desorption from single crystal to nanoparticulate Ru model catalysts

S. Murphy, C. Strebel, S. B. Vendelbo, C. Conradsen, Y. Tison, K. Nielsen, L. Bech, R. M. Nielsen, M. Johansson, I. Chorkendorff and J. H. Nielsen*

Received 11th February 2011, Accepted 1st April 2011
DOI: 10.1039/c1cp20371a

Using model catalysts, we demonstrate that CO desorption from Ru surfaces can be switched from that typical of single crystal surfaces to one more characteristic of supported nanoparticles. First, the CO desorption behaviour from Ru nanoparticles supported on highly oriented pyrolytic graphite was studied. Both mass-selected and thermally evaporated nanoparticles were deposited. TPD spectra from the mass-selected nanoparticles exhibit a desorption peak located around 410 K with a broad shoulder extending from around 480 K to 600 K, while spectra obtained from thermally evaporated nanoparticles exhibit a single broad feature from ~350 K to ~450 K. A room temperature deposited 50 Å thick Ru film displays a characteristic nanoparticle-like spectrum with a broad desorption feature at ~420 K and a shoulder extending from ~450 K to ~600 K. Subsequent annealing of this film at 900 K produced a polycrystalline morphology of flat Ru(001) terraces separated by monatomic steps. The CO desorption spectrum from this surface resembles that obtained on single crystal Ru(001) with two large desorption features located at 390 K and 450 K due to molecular desorption from terrace sites, and a much smaller peak at ~530 K due to desorption of dissociatively adsorbed CO at step sites. In a second experiment, ion sputtering was used to create surface defects on a Ru(0 1 54) single crystal surface. A gradual shift away from the desorption spectrum typical of a Ru(001) surface towards one resembling desorption from supported Ru nanoparticles was observed with increasing sputter time.

I. Introduction

While surface science studies of macroscopic single crystal surfaces have yielded much valuable insight into the fundamental principles of heterogeneous catalysts, the well-known materials gap between surface science and industrial catalysis exists.[1–4] Typically, industrial catalysts are much more complex in nature than the single crystal surfaces encountered in many surface science studies. A better representation of these materials can be obtained by studying an ensemble of nanoparticles supported on a well-defined planar substrate.[5–7] Such model systems can be used to investigate the effect of the particle size and the influence of the support material on reactivity. Moreover, nanoparticulate model catalysts are more suited to studying the correlation between structure and activity in structure-sensitive reactions because of the resemblance to industrial catalysts, which comprise a high density of various active sites such as edge or corner sites, as compared to single crystal surfaces where the number of equivalent step or kink sites can be outweighed by several orders of magnitude by less-active terrace sites.[8,9] As part of our efforts to understand the materials gap we have been investigating the crossover in desorption behaviour between the two model catalyst systems, *i.e.* single crystal surfaces *versus* supported nanoparticles. Here we present details of our investigation of the thermal desorption of CO from a Ru(0 1 54) single crystal surface and from Ru nanoparticles supported on highly oriented pyrolytic graphite (HOPG).

Ruthenium is a versatile catalyst, which has been particularly investigated with respect to methanation and Fischer–Tropsch synthesis.[10–12] As an elementary step in this process the adsorption of CO on single crystal Ru(001) has been studied extensively by various surface science methods.[13–22] CO adsorbs on the Ru(001) basal surface in an upright position *via* the carbon atom at all coverages up to saturation at around 2/3 of a monolayer.[23–25] The CO molecules adsorb in on-top positions up to a coverage of 1/3 of a monolayer, forming a $(\sqrt{3}\times\sqrt{3})R30^\circ$ adlayer structure.[26–28] At higher coverages, the $(\sqrt{3}\times\sqrt{3})R30^\circ$ structure is disrupted as strong repulsive interactions cause CO molecules to be displaced from on-top positions (though the exact microstructure of the higher coverage overlayers is still debated[29]).

Center for Individual Nanoparticle Functionality, Department of Physics, Technical University of Denmark, 2800 Kgs. Lyngby, Denmark. E-mail: jane@fysik.dtu.dk; Fax: +45 4593 2399

The change in adlayer structure is reflected in the CO desorption behaviour. For coverages up to 1/3 of a monolayer CO desorbs in a single peak decreasing from 480 K to 450 K with increasing coverage (α_1 peak), while for higher coverages a second peak develops around 350–400 K (α_2 peak).[18,22,30,31] In addition to these peaks, which are due to desorption of molecularly adsorbed CO, an additional much smaller peak may also be observed at around 530 K, arising from the desorption of CO that has been dissociatively adsorbed at step sites (β peak).[13,19,21,22,32] This was demonstrated by Shincho *et al.*,[13] Yamada *et al.*[19] and Zubkov *et al.*[21,22] using isotopic scrambling experiments, which rely on the recombination and desorption of atomic carbon and oxygen originating from the dissociative adsorption of CO. It was furthermore demonstrated that deposition of carbon at surface steps blocked them for dissociative adsorption of CO and resulted in the disappearance of the β peak from CO desorption spectra.[22,32]

The CO desorption from more open Ru single crystal surfaces has also been investigated and displays similarities to TPD spectra obtained from the Ru(001) plane.[33–37] For the Ru(110) plane, for example, the α_1 and α_2 peaks at similar temperatures were observed along with two β peaks attributed to dissociation of CO at different sites. The desorption of CO_2 from the Ru(110) surface at 380–450 K was furthermore observed.

If we consider the information available with regard to CO desorption from supported Ru nanoparticles, a number of studies have investigated CO desorption from Ru catalysts prepared by chemical impregnation of SiO_2 and Al_2O_3 supports.[38–42] Typically, two main features were observed in these studies, a low temperature feature located between 350 K and 475 K, and a higher temperature feature located between 600 K and 700 K.[38–42] The two features at lower temperatures agree well with the double-peak spectrum obtained from Ru(001)[18,22,30,31] and the variation in the temperatures recorded for the desorption features in the different studies could be attributed to the different heating rates used. Moreover, where desorption experiments were performed in reactors under a He carrier gas flow,[38–41] the measured desorption temperatures could also be influenced by readsorption of CO, which was found to shift desorption peaks to higher temperatures.[39] The desorption of CO_2 was also observed in some of these studies, which could be taken as evidence of CO dissociation occuring over the Ru nanoparticles.[39,40,42]

Here, we demonstrate that it is possible to link the desorption behaviour of supported nanoparticles (both mass-selected particles formed in a magnetron-sputter gas-aggregation source and vapour-deposited particles) and that of the single crystal surface using two approaches. In the first case, we demonstrate the transition from nanoparticle-like CO desorption behaviour to single-crystal surface behaviour in Ru nanoparticles supported on HOPG. In the second case, we demonstrate the reverse transition from single-crystal surface to nanoparticle-like CO desorption behaviour by means of Ar^+ ion pre-sputtering of the Ru(0 1 54) surface.

II. Experimental

The experiments were performed in three separate UHV systems. The experiments on Ru nanoparticles were performed in a multichamber ultrahigh vacuum (UHV) system (Omicron, Multiscan Lab) with a base pressure in the low 10^{-11} mbar region.[43,44] This system is equipped with facilities for combined scanning tunneling microscopy (STM) and scanning electron microscopy (SEM), as well as Auger electron spectrsocopy (AES), ion scattering spectroscopy (ISS) and temperature programmed desorption (TPD) measurements. The thermal desorption experiments on the Ru(0 1 54) surface were performed in a UHV chamber with a base pressure below 10^{-10} mbar, which is equipped with facilities for TPD and AES, as well as a high-pressure cell.[32] STM measurements on the Ru(0 1 54) surface were performed in a UHV chamber with a base pressure below 10^{-10} mbar,[45] which is equipped with X-ray photoelectron spectroscopy (XPS) and an Aarhus-type STM.[46]

A Ru nanoparticles on HOPG

The HOPG substrates (SPI-1, 7 mm × 7 mm × 0.5 mm) were cleaved in air and mounted in sample holders incorporating a pyrolytic boron nitride (PBN) radiative heater, which is capable of heating the sample to temperatures in excess of 975 K. A C-type thermocouple (W-5 at.% Re/W-26 at.% Re) was placed in contact with the substrate in order to monitor and control the sample temperature *via* a PID controller (Eurotherm 2408). Upon insertion into UHV, the samples were outgassed for several hours at 775 K to outgas adsorbed contaminants prior to use. Two different methods were used to deposit Ru nanoparticles.

In the first method, mass-selected nanoparticles were deposited from an inert-gas aggregation source (Mantis Deposition Ltd.), which is described in detail elsewhere.[43,44] Briefly, a flux of Ru atoms is produced by a magnetron sputter head, which is condensed into nanoparticles upon contact with cooled Ar gas atoms. The ionised fraction of the nanoparticle beam is filtered to select the mass of the nanoparticles to be deposited using a quadrupole mass filter, before the nanoparticles are soft-landed (*i.e.* they have a kinetic energy of ≤ 0.1 eV atom^{-1}) onto HOPG substrates. For these studies, we have investigated both as-cleaved HOPG and surfaces that have been sputtered for 15 min with 500 eV Ar^+ ions at a current density of ~ 1 μA cm^{-2} and subsequently outgassed at 935 K. The 15 min sputtering causes defects in at least the first two layers of the surface.[47]

In the second method, Ru films were deposited on HOPG by electron-beam evaporation of a 99.99% purity Ru rod. The substrates were either as-cleaved or sputtered for 30 s with 500 eV Ar^+ ions under the same conditions as those given above. Sputtering for only 30 s produces approximately 5% of defects in the topmost surface layer. The substrate was grounded while the Ru rod was held at a positive bias of 500 V.[48] A quartz crystal balance was used to monitor the deposition rate (typically 0.46–0.9 Å min^{-1}) and estimate the final film thickness.

Ion Scattering Spectroscopy (ISS) was used to confirm the cleanliness of the HOPG substrate and the deposited Ru nanoparticles and thin films. The ISS spectra were recorded using 1 keV He^+ ions produced by a differentially pumped electron impact ion source (ISE 100, Omicron Nanotechnology). The reflected ions were detected at a 147° scattering angle with a hemispherical energy analyser.

TPD experiments were performed in the preparation chamber of the UHV system. The samples were dosed with a 1 : 1 mixture of two different isotopically labeled CO molecules, namely $^{13}C^{16}O$ (CIL, 99% ^{13}C, $<10\%$ ^{18}O)[49] and $^{12}C^{18}O$ (CIL, 2% ^{16}O). Both gases were dosed simultaneously using separate leak valves until a total chamber pressure of 2×10^{-8} mbar was attained. The ratio of the two gases was held constant by monitoring the mass spectrometer signal for each component. The samples were dosed in this manner for 10 min, corresponding to an exposure of nine Langmuir, which was sufficient to saturate the surface. It was possible to observe the saturation in the CO uptake during dosing with the mass spectrometer. The sample temperature was then ramped at a rate of 1 K s^{-1} in UHV and the CO desorption from the substrate was analysed using a differentially pumped Balzers QMA 125 quadrupole mass spectrometer. The spectrometer was equipped with an oxygen-free high conductivity (OFHC) copper sniffer tip with a 1 mm diameter aperture, which is positioned within 0.5 mm of the sample surface. This arrangement allows the local gas composition above the sample surface to be measured with negligible contribution from the sample holder or surroundings.

The isotope exchange reaction ($^{12}C^{18}O + {}^{13}C^{16}O \rightarrow {}^{12}C^{18}O + {}^{13}C^{16}O + {}^{13}C^{18}O + {}^{12}C^{16}O$) allows us to determine the relative amount of CO that has been dissociated on the surface from the TPD spectra. If the adsorbed $^{13}C^{16}O$ and $^{12}C^{18}O$ molecules dissociate on the surface, the dissociated species can scramble and recombine into the four possible CO isotopologues $^{12}C^{16}O$, $^{13}C^{16}O$, $^{12}C^{18}O$ and $^{13}C^{18}O$. The TPD mass spectrometer signals of 28 amu, 29 amu, 30 amu and 31 amu were background subtracted and integrated to find the total desorption of each isotopologue. Particular attention was paid to the $^{13}C^{18}O$ signal as this does not have a high natural background in the UHV chamber like $^{12}C^{16}O$, and does not contribute to molecular desorption like either $^{13}C^{16}O$ or $^{12}C^{18}O$. Assuming an equal probability for scrambling into each of the four products, the amount of desorbed $^{13}C^{18}O$ will account for approximately one quarter of the total amount of adsorbed CO molecules that have been dissociated.

STM was performed at room temperature in constant current mode, using electrochemically etched W tips without any in-vacuum treatments other than applying a series of voltage pulses (typically 4–9 V for 10–100 ms) or scanning for several lines with increased bias ($U \approx 2$ V) in order to condition the tip. The typical tunnel parameters used to image the particles in this study were $U = 10$–600 mV for the gap bias and $I = 0.1$–0.8 nA for the tunnel current. Slow scan speeds were adopted with a typical line scan frequency of about 0.5–1 Hz.

B Ru(0 1 54) surface

The samples used for these experiments are Ru(0 1 54) single crystals (Mateck GmbH.), which on average expose 27-atom wide (001) terraces separated by monatomic steps. Due to the hexagonal close-packed structure of Ru, the steps will be of two alternating structures, one with three-fold symmetry and the other with four-fold symmetry.[22] For the TPD experiments presented here, a Ru(0 1 54) sample was cleaned by repeated cycles of sputtering with 1 keV Ar^+ ions at 800 K for 30 min, oxidation in 10^{-7} mbar O_2 at 1100 K for 10 min, reduction in 10^{-6} mbar H_2 at 500 K for 30 min, and finally annealing to 1200 K in UHV for 1 min. The cleanliness of the sample was checked by AES and CO TPD and oxygen titration measurements (which were used to check for carbon contamination).[32] TPD measurements were performed using a (Balzers 125) quadrupole mass spectrometer fitted with a differentially pumped OFHC copper sniffer tip with a 2 mm diameter circular aperture. This orifice was positioned at a distance of 0.5 mm from the sample surface, so that only desorption from the front side of the single crystal was measured. The sample temperature was measured by means of a C-type thermocouple spot-welded to the side of the crystal. The crystal was mounted on tungsten filaments which were used to provide direct current heating. During TPD measurements the sample temperature was ramped linearly at a rate of 2 K s^{-1}. The sample was mounted in the UHV chamber out of direct line-of-sight of the ionisation gauge in order to avoid hot-filament induced chemistry.

A second Ru(0 1 54) sample was used for the STM measurements, which was cleaned using a similar procedure to that described above.[50] The sample was sputtered using 1 keV Ar^+ ions by quickly rastering a 3 mm diameter ion beam with a current density of 18 μA cm^{-2} across the sample surface. The cleanliness was checked using STM, XPS and CO TPD measurements (the TPD setup was similar to the one described above). STM measurements were performed at room temperature in constant current mode, using electrochemically etched W tips. Images were typically recorded with a gap bias of 1 V and a tunneling current of 0.4–1 nA.

III. Results

A Ru nanoparticles on HOPG

The morphology of the mass-selected nanoparticles has been described in detail elsewhere.[43,44] Depositions were carried out so that between 10% and 40% of the HOPG surface was covered by a monodisperse distribution of nanoparticles with a mean diameter in the range from 2 nm to 15 nm.[51] Transmission electron microscopy (TEM) was used to measure the particle size distributions obtained after mass filtering and it was found that the diameters of the nanoparticles were distributed within ±15% of the mean diameter. TEM measurements revealed that smaller nanoparticles displayed more well-defined facets, while larger nanoparticles were found to be irregular in shape with evidence of significant surface roughness.[44] An example of a STM image of mass-selected 9.7 nm Ru nanoparticles on HOPG is shown in Fig. 1(a). We have previously established that the morphology of nanoparticles supported on sputtered or as-cleaved HOPG is basically the same.[43] Fig. 1(b) shows the total CO desorption spectrum obtained from 9.7 nm Ru nanoparticles. The TPD spectrum is characterised by a desorption peak located around 410 K, followed by a broad shoulder extending from around 480 K to 600 K. The molecularly- and dissociatively-adsorbed components of the TPD spectrum [also shown in Fig. 1(b)] can be deconvoluted by utilising the isotope exchange reaction,

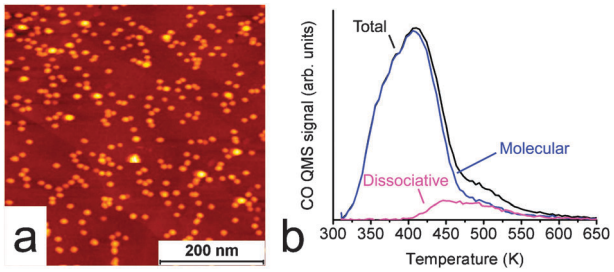

Fig. 1 STM and CO desorption from size-selected Ru nanoparticles on HOPG. (a) STM image of 9.7 nm Ru nanoparticles on sputtered HOPG. (b) CO TPD spectrum obtained from 9.7 nm Ru nanoparticles on as-cleaved HOPG, showing the total CO desorption, as well as the contributions from molecularly- and dissociatively-adsorbed CO.

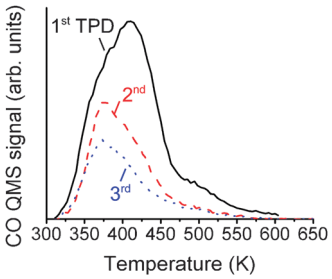

Fig. 2 Three successive CO TPD spectra obtained from 9.7 nm mass-selected Ru nanoparticles on as-cleaved HOPG, showing a drop in the desorption area.

$^{12}C^{18}O + {}^{13}C^{16}O \rightarrow {}^{12}C^{18}O + {}^{13}C^{16}O + {}^{13}C^{18}O + {}^{12}C^{16}O$, which is expected to occur after CO dissociation. It is clear that the large desorption peak located around 410 K corresponds to the molecularly desorbed component (*i.e.* mass-29 and mass-30 CO), while desorption of dissociatively adsorbed CO (here only mass-31 CO is used in the analysis), which displays peaks at 450 K and 530 K, is largely responsible for the broad shoulder up to 600 K seen in the total CO desorption spectrum.

Fig. 2 shows three successive CO TPD spectra obtained from 9.7 nm Ru nanoparticles on as-cleaved HOPG. The main desorption feature, which is located around 410 K in the first TPD, shifts to 375 K in the second and third spectra. There is also a substantial loss in the CO desorption area (63%) between the first and second TPD, and a smaller drop (30%) between the second and third TPD. This behavior was consistently observed for different nanoparticle sizes on as-cleaved and sputtered HOPG. It was usually found that the loss in desorption area became small or negligible after the second or third TPD. Three mechanisms can be identified as candidates for this deactivation: (1) sintering, (2) poisoning by loose carbon from the support, and (3) annealing-out of the initial surface roughness of the as-deposited nanoparticles. We have previously confirmed by STM that small nanoparticles (*e.g.* ~3 nm) deposited onto as-cleaved HOPG do sinter at elevated temperatures (775–975 K).[43] We have also performed oxygen titration experiments (not presented here), which indicate that carbon is present at the surface of the nanoparticles after heating to temperatures comparable to those encountered during the desorption experiments. We can therefore confirm that both of these mechanisms contribute to the deactivation of the nanoparticles, while the third proposed mechanism requires further investigation by performing annealing experiments in the TEM.

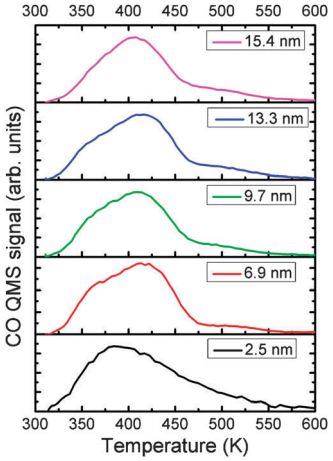

Fig. 3 CO TPD spectra obtained for different sized Ru nanoparticles supported on as-cleaved HOPG. The curves have been normalised to the same peak height.

Fig. 3 compares the total CO TPD spectra obtained from nanoparticles of different sizes supported on as-cleaved HOPG. The curves have been normalised to the same peak height in order to compare their shape. The TPD spectra are qualitatively similar being characterised by a broad desorption feature with a peak around 410–420 K and a broad shoulder extending from ~450 K to ~600 K. The low-temperature shoulder along with the high-temperature tail seems to increase as the nanoparticle size decreases, being most prominent for the 2.5 nm size. In previous studies of PVD grown Ru nanoparticles on mica, the position of the CO desorption feature was not observed to change substantially with the mean particle size.[52]

In addition to investigating the CO desorption behavior from mass-selected nanoparticles produced using the inert-gas aggregation source, we have also investigated the CO desorption behavior of PVD-grown Ru nanoparticles on HOPG. The morphology of these nanoparticles has been discussed in detail elsewhere.[43] Briefly, Ru films deposited onto as-cleaved HOPG at room temperature were found to display bimodal growth with small round nanoparticles decorating the substrate step edges and large flat nanoparticles formed on the terraces. The mean diameter of these nanoparticles was between 3 nm and 5.5 nm and their mean height was around 1.5 nm, while the spread in the measured size distributions was of the order of ±30%. On sputtered HOPG, room temperature deposition of Ru results in the formation of small round nanoparticles with a narrow size distribution. In this case, the mean particle diameter was approximately 2.3 nm and the mean height was close to 1.3 nm, while the spread in the measured particle size was ±20%. Examples of these two nanoparticle morphologies are shown in Fig. 4(a) and (c), which show STM images of 1 Å Ru films deposited on as-cleaved and sputtered HOPG, respectively. These images were obtained after CO TPD measurements were made. The average diameter of the nanoparticles from the 1 Å deposition was 5.2 ± 2.1 nm on the terraces

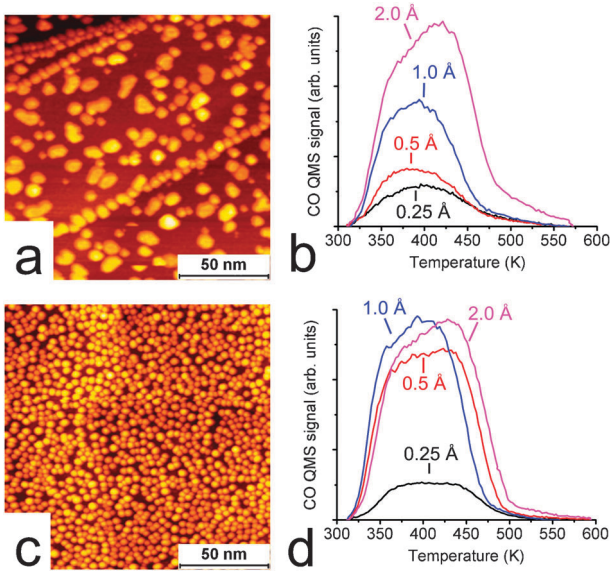

Fig. 4 STM and CO TPD measurements of Ru films deposited onto HOPG. (a) STM image of a 1 Å Ru film deposited onto as-cleaved HOPG. The average diameter of the terrace nanoparticles was 5.2 nm and their average height was 1.7 nm. (b) CO TPD spectra from 0.25–2.0 Å Ru films on as-cleaved HOPG. (c) STM image of a 1 Å Ru film deposited onto HOPG that has been pre-sputtered with 500 eV Ar^+ ions for 30 s. The average nanoparticle diameter was 2.1 nm and the average height was 1.1 nm. (d) CO TPD spectra from 0.25–2.0 Å Ru films on sputtered HOPG.

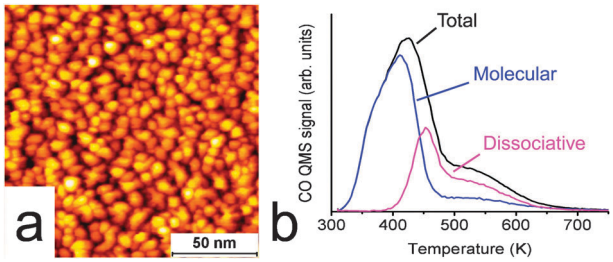

Fig. 5 (a) STM image of a 50 Å Ru film deposited on as-cleaved HOPG at room temperature. (b) The corresponding CO TPD spectrum obtained from the film, showing the total CO desorption, as well as the contributions from molecularly- and dissociatively-adsorbed CO.

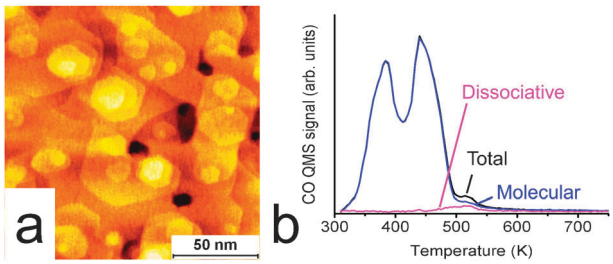

Fig. 6 (a) STM image of a 50 Å Ru film deposited on as-cleaved HOPG after annealing in UHV at 900 K for 10 min. (b) The corresponding CO TPD spectrum obtained from the film, showing the total CO desorption, as well as the contributions from molecularly- and dissociatively-adsorbed CO.

and 3.9 ± 1.0 nm along the steps, in the case of deposition on the as-cleaved HOPG surface [*cf*. Fig. 4(a)], and 2.1 ± 0.5 nm in the case of deposition on the pre-sputtered HOPG [*cf*. Fig. 4(c)]. The heights of the nanoparticles were on the order of 1–2 nm.[43] Fig. 4(b) and (d) show CO desorption spectra for different nominal film thicknesses deposited on (b) as-cleaved HOPG and (d) HOPG sputtered for 30 s with 500 eV Ar^+ ions. The desorption spectra are characterised by a single broad feature from ~350 K to ~450 K. For Ru nanoparticles deposited on as-cleaved HOPG the CO desorption area increases continuously with increasing nominal film thickness in the thickness range investigated here [see Fig. 4(b)]. This reflects the fact that the HOPG surface is gradually covered by Ru nanoparticles with increasing film thickness. By contrast, there is a substantial jump in the CO desorption area from the 0.25 Å to 0.5 Å Ru films on sputtered HOPG, after which the amount of CO desorbing from the surface remains approximately constant. In this case, the HOPG surface is partially exposed for the 0.25 Å film, but is almost completely saturated by Ru nanoparticles at a nominal film thickness of 0.5 Å [see Fig. 4(d)]. Thereafter, the total Ru surface area exposed to CO remains approximately constant for thicker films.[43] As was the case for the mass-selected nanoparticles, successive TPD spectra of the vapour-deposited nanoparticles (not shown here) also displayed deactivation of the nanoparticles between the first and second TPD measurements.

We have examined the CO desorption behaviour of these PVD-grown Ru films up to the extreme case of a 50 Å Ru thin film. Fig. 5(a) shows an image of a 50 Å Ru film deposited on as-cleaved HOPG at room temperature. The surface morphology of the film comprises nanoparticles with a mean diameter of 6 ± 2 nm. The substrate cannot be imaged by STM as the film is several layers thick. Fig. 5(b) shows the corresponding CO desorption spectrum, which shows a single broad desorption feature centered around 420 K and a broad shoulder from 500 K to 600 K. After obtaining this spectrum the film was annealed for 10 min at 900 K in UHV. The resulting film morphology, shown in Fig. 6(a), is polycrystalline with large flat terraces separated by monatomic steps. The corresponding CO desorption spectrum is shown in Fig. 6(b), and shows two desorption features at ~390 K and ~450 K. An additional, smaller peak can be seen at ~530 K. This spectrum agrees well with the typical desorption spectrum obtained from the Ru(001) facet.[18,22,30–32] The two principal peaks can be attributed to desorption of molecularly adsorbed CO from the terraces (α peaks), while the smaller peak can be attributed to desorption of dissociatively adsorbed CO from step sites (β peak).[13,22]

B Ru (0 1 54) surface

Fig. 7(a) and (b) show STM images of the non-sputtered Ru (0 1 54) surface and the same surface after sputtering for 5 min, respectively. The non-sputtered surface is characterised by terraces with a width varying between 4 nm and 10 nm, encompassing the expected average terrace width of 6.5 nm (corresponding to 27 atoms), and separated by straight monatomic steps with a measured height of 0.21 ± 0.01 nm, which is in good agreement with the distance between the (001) planes of ruthenium. In comparison, the steps on the sputtered surface display a high degree of roughness, while small islands are

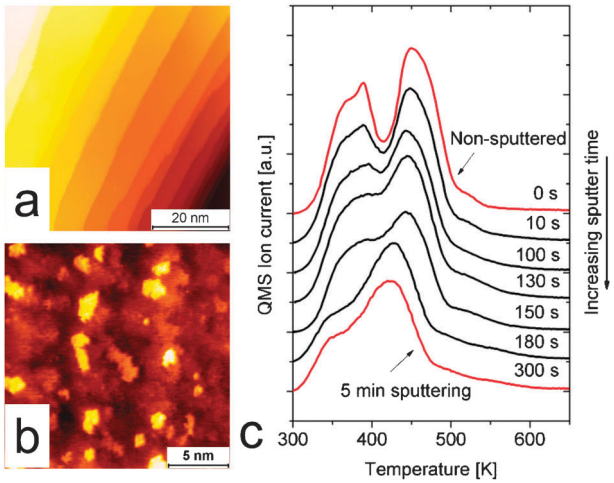

Fig. 7 STM and CO TPD measurements from a Ru(0 1 54) single crystal surface before and after Ar^+ ion sputtering. (a) STM image of the clean non-sputtered Ru(0 1 54) surface. (b) STM image of the same surface after sputtering with 1 keV Ar^+ ions for 5 min. (c) Sequence of CO TPD spectra obtained from the Ru(0 1 54) surface after sputtering with 1 keV Ar^+ ions for increasing periods of time.

evident on the terraces, which are presumably formed by surface restructuring as a result of the sputtering process.

Fig. 7(c) shows a sequence of CO desorption spectra obtained from the Ru(0 1 54) surface after different periods of sputtering with 1 keV Ar^+ ions at room temperature. The CO desorption spectrum from the non-sputtered surface shows two desorption peaks located at 390 K and 460 K that are characteristic of CO desorption from (001) terraces (α_1- and α_2-peaks) and a peak at $\sim$535 K corresponding to the dissociative adsorption at step sites (β-peak).[18,22,30–32] However, with increased surface sputtering a gradual transition is observed between the double-peak spectrum towards a single broad feature centered around 420 K. The desorption feature seen at 390 K on the non-sputtered surface gradually disappears with increased sputtering time until it is no more than a shoulder on the low-temperature side of the main desorption feature seen for the 5 min sputtered surface. In addition, the peak at 460 K on the non-sputtered surface gradually shifts down in temperature with increased sputtering time until the feature is located around 420 K.

It should be pointed out once again that the STM and TPD data of the Ru(0 1 54) surface presented here were obtained in two different UHV systems. However, in both cases the cleanliness of the surface before and after sputtering was confirmed (by XPS in the case of the STM measurements, and by AES and oxygen titration measurements in the case of the TPD experiments) to ensure that a contamination level below $\sim$1% was obtained. Moreover, CO TPD measurements were also performed in the STM system, which yielded qualitatively similar results to those presented here.

IV. Discussion

A Comparison of desorption energies

As demonstrated in Section IIIA the isotope exchange reaction unambiguously identifies molecular desorption being responsible for the main desorption feature at 410–420 K, while dissociative adsorption is responsible for smaller features at 430 K and 500 K. For comparison, Table 1 gives a summary of the CO desorption features reported from various studies (including this study) of supported Ru nanoparticles and single crystal surfaces. For the purposes of comparing our results to literature values, desorption energies based on the data presented in Table 1 are calculated and presented together in Fig. 8. The desorption features were classified into two categories corresponding to molecular (first-order) and dissociative (second-order) adsorption on the basis of the literature surveyed in Section I. The first-order desorption energies were calculated using the Redhead equation[53] and assuming a pre-exponential factor of 10^{13} s^{-1}. The second-order desorption energies were solved iteratively using the equation:[54]

$$E_{\mathrm{des}}(\theta) = RT_{\mathrm{p}} \ln\left(\frac{2\theta\nu(\theta)RT_{\mathrm{p}}^2}{E_{\mathrm{des}}(\theta)\beta}\right) \qquad (1)$$

where T_{p} is the desorption peak temperature, θ is the remaining CO coverage (assumed to be half the initial coverage) and R is the gas constant. The desorption energy E_{des} and the pre-exponential factor ν are both assumed to be constant with coverage, where $\nu = 10^{13}$ s^{-1}.

From our CO TPD experiments on graphite-supported nanoparticles, we calculate desorption energies of 112–113 kJ mol^{-1}, which agree reasonably well with the values calculated from previous studies of oxide-supported nanoparticles,[38–42] particularly

Table 1 Summary of CO desorption features from saturation coverages of CO on various supported Ru nanoparticles and single crystal surfaces. The peak temperatures for the different desorption features and the heating rate are listed. Temperature intervals for some features have been indicated by hyphenated values. The desorption features have been classified into two categories; T_α representing molecular desorption and T_β representing dissociative adsorption

System	T_α/K	T_β/K	Heating rate/K s^{-1}
Ru NPs/HOPG[a]	410-420	450, 530	1
50 Å Ru/HOPG (as-deposited)[a]	420	450, 530	1
50 Å Ru/HOPG (annealed)[a]	390, 450	530	1
Ru/mica[52]	$\sim$410		1.5
Ru/Al_2O_3[38]	375	475, 600–630	1
Ru/Al_2O_3[39]	460	620	1
Ru/SiO_2[40]	450	650	1.5
Ru/SiO_2[41]	405, 473	698	0.17
(001)[18,30]	405-420, 465-480		5
(109)[22]	400, 450	535	2
(0 1 54)[32]	$\sim$390, $\sim$460	535	2
(0 1 54) non-sputtered[a]	$\sim$390, $\sim$460	535	2
(0 1 54) sputtered[a]	$\sim$420		2
Ru(S)-[15(001)×2(100)][20]	400, 470	520	9
(1 $\bar{1}$ 10)[13]	460	$\sim$580	15
(2 $\bar{1}$ 10)[19]	$\sim$460	$\sim$530	7.7
(2 $\bar{1}$ 22)[19]	$\sim$470	$\sim$530	5.2
(101)[33]	$\sim$480	$\sim$520	30
(100)[34]	$\sim$403, $\sim$495		8
(100)[35]	350, 380, 500		4
(100)[36]	375, $\sim$400, $\sim$500		8.7
(110)[37]	400, 440-460	500, 540	3

[a] This work.

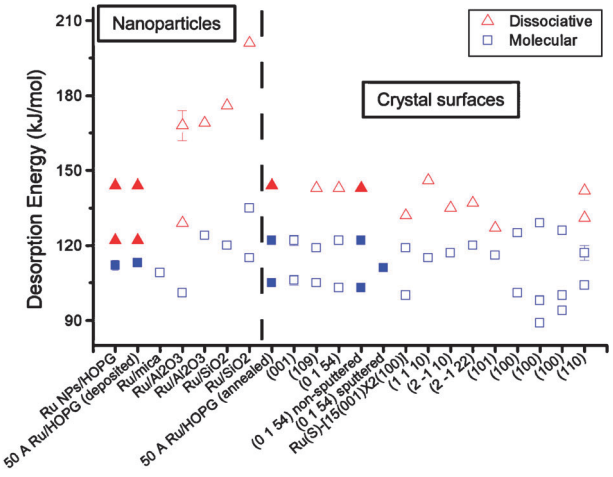

Fig. 8 Summary of the desorption energies calculated using the data presented in Table 1. Open symbols are data taken from previous studies, while filled symbols are taken from the present study. Temperature intervals for certain features are indicated by error bars.

with the case of PVD-grown nanoparticles on mica, see Fig. 8.[52] On the other hand, the desorption energies for dissociatively adsorbed CO (122 kJ mol^{-1} and 144 kJ mol^{-1}) calculated for our graphite supported nanoparticles are much lower than those estimated from the data available from these other studies, where a high temperature desorption feature was typically observed between 600 K and 700 K, corresponding to desorption energies around 164–201 kJ mol^{-1}. The origins of these high temperature peaks were investigated by McCarty and Wise[38] who used isotopic scrambling of $^{13}C^{16}O$ and $^{12}C^{18}O$ to investigate the dissociation of CO over Ru/Al_2O_3. While they observed isotope exchange at ~475 K (129 kJ mol^{-1}), which is in reasonable agreement with the results obtained in the present study, they also observed an unusual behaviour at ~600 K where the levels of ^{18}O containing isotopologues ($^{12}C^{18}O$ and $^{13}C^{18}O$) were found to decrease, while the levels of ^{16}O containing isotopologues ($^{12}C^{16}O$ and $^{13}C^{16}O$) increased. This indicated that an excess of ^{16}O was being derived from some source, though the Al_2O_3 support was ruled out as a potential source on the basis of blank TPD measurements. As a result, the nature of the higher temperature desorption feature observed between 600 K and 700 K in most of these studies has not been adequately explained and may be linked to the method of preparing the catalyst, *i.e.* wet impregnation.

B Origins of the nanoparticle desorption spectra

Compared to the single crystal surfaces, the desorption energies calculated for both molecularly- and dissociatively-adsorbed CO on the supported nanoparticles in the present study generally fall within the range of energies calculated for both the basal Ru surface and for more open surfaces. This may be attributed to the fact that the nanoparticles expose facets with different orientations. In the simplest representation of the nanoparticle shape, *i.e.* the Wulff construction, the nanoparticles will principally comprise (001), (101) and (100) facets, as these have the lowest surface free energy.[44,55] Consequently, the desorption spectra should mainly contain contributions from these facets. However, we have previously shown that the shape of the mass-selected Ru nanoparticles departs from the Wulff construction,[44] and consequently the CO desorption behaviour is expected to be more complex than one based on this simple model. In addition to the orientation of the facets exposed on the nanoparticle surface, their size may also influence the desorption spectra. For example, it has been shown that the double-peak molecular desorption feature characteristic of the Ru(001) facet appears to be inhibited on stepped Ru single crystal surfaces when the average terrace width is sufficiently narrow.[13,19] Shincho *et al.*[13] found a single desorption feature during CO desorption from a Ru(S)-[5(001)×(110)] surface comprising five-atom wide (001) terraces,[56] whereas Westre *et al.*[20] and Zubkov *et al.*[22] observed two desorption features during desorption from saturated CO coverages on Ru(S)-[15(001)×2(100)] and Ru(S)-[9(001)×2(101)] surfaces comprising fifteen- and nine-atom wide (001) terraces, respectively. There are two possible explanations for this: (1) the terraces are too small to accommodate the ordered overlayer structures found on extended (001) facets and (2) a localised lattice strain is produced in the vicinity of steps, which has been shown to influence CO adsorption.[57] In the case of nanoparticles, where facet sizes can be comparably small to the terrace widths found on highly stepped single crystal surfaces, both of these mechanisms may play a role in determining the CO desorption behaviour from the nanoparticle surface. In Fig. 4, a change in the desorption spectrum may be present for the smallest (*i.e.* 2.5 nm) of the nanoparticles with an increase in the low-temperature shoulder and in the high-temperature tail. This suggests that different sites are relatively more abundant on the very small nanoparticles. Detailed investigations of several mass-selected nanoparticle sizes in the 1–5 nm range are needed before conclusions can be made, but it is interesting to note that carbon-supported cobalt nanoparticles, which—just like ruthenium—are catalysts for the Fischer–Tropsch (FT) reaction, show an increase in FT activity for the very small sizes.[58]

It should also be pointed out that pre-adsorption of a small amount of O_2 or H_2O onto the Ru(001) surface prior to CO adsorption can substantially shift the TPD spectrum from the double-peak spectrum to a spectrum similar to that obtained from supported nanoparticles.[59,60] However, in the present study ISS measurements performed on the nanoparticles both before and after the TPD experiments showed no evidence of oxygen (*i.e.* below the detection limit of 1% of a monolayer). This indicates that the shape of the TPD spectra is related to the structure of the clean nanoparticle surface. We therefore conclude that the TPD spectrum obtained from the nanoparticles can be linked to a combination of the compact facet size on the nanoparticle surface, and the fact that more open facets may be exposed. This is particularly true when the shape of the nanoparticles departs from the equilibrium shape. Moreover, we observe two features corresponding to desorption of dissociatively adsorbed CO at 450 K and 530 K (desorption energies of 122 kJ mol^{-1} and 144 kJ mol^{-1}, respectively), which point to the presence of two main dissociation sites for CO on the nanoparticle surface.

C Crossover in desorption behaviour

A key result of the present study is that we have been able to demonstrate the crossover in CO desorption behaviour between Ru nanoparticles and the basal Ru surface simply by annealing a PVD-grown thin film to high temperature. The fact that we observe dissociative CO adsorption both before and after annealing the film proves that the surface remains free of carbon from the support, which would otherwise block the undercoordinated sites responsible for CO dissociation on the surface.[22,32] A key element in the formation of the polycrystalline film in Fig. 6 is that an epitaxial relationship exists between the vapour deposited Ru and the HOPG surface. In the case of the mass-selected nanoparticles discussed earlier, no such epitaxial relationship is obtained since the nanoparticles are formed before deposition and assume random orientations when landed on the surface. As expected, it was therefore not possible to obtain a morphology like that shown in Fig. 6(a) by annealing a thin film of mass-selected nanoparticles at 900 K. However, we believe that this should in principle be possible if higher anneal temperatures are used, which was not possible with the existing experimental set-up.

It was also possible to demonstrate the reverse transition in desorption behaviour between that of the basal Ru surface and that of Ru nanoparticles by sputtering a single crystal surface. As the amount of sputtering increases the amount and type of surface sites change as probed by the CO TPDs in Fig. 7(c). It is seen that the amount of step sites giving rise to the small shoulder at 510 K for the non-sputtered surface increases with more sputtering and changes into a broad feature ranging from below 500 K to at least 600 K for the most sputtered surface. This indicates that the sputtering introduces more undercoordinated sites, and that different kinds of sites exist giving rise to different desorption temperatures of dissociatively adsorbed C and O. More detailed STM studies of the sputtered surface would be required to identify the different site configurations.

It was found that the molecular desorption feature at 390 K gradually disappears, while the desorption feature at 460 K, corresponding to more strongly bound molecular CO, shifts downwards in temperature with increased sputtering. This can be rationalized as an effect of having smaller average terrace sizes on the sputtered surface. As mentioned earlier, the terraces may be too small to accommodate the ordered overlayer structures found on extended (001) facets. Also, it has previously been suggested by Jakob *et al.*[57] that the region 1–2 nm from the step exhibits a compressed lattice, which would result in a weaker binding of CO.[61] With a higher abundance of terrace sites in close proximity to a step, more weakly bonded CO would be expected, in excellent agreement with our CO TPDs.

It is observed that desorption of CO from the sputtered surface starts immediately upon heating from room temperature, whereas the desorption from the non-sputtered surface does not start until around $\sim$20 K above room temperature. This indicates that our CO TPD spectra from the sputtered surfaces do not probe all sites available on the surface, as the TPD spectrum from the non-sputtered surface appears to do. As such, one should not attempt to rationalise the apparent trend in Fig. 7(c) that the total CO desorption area decreases with increased sputtering time, until TPD experiments starting from below room temperature are performed.

V. Summary

We have compared the CO desorption characteristics of a stepped Ru(001) single crystal with Ru nanoparticles supported on graphite and have established the crossover in CO desorption behaviour between the two. Our main findings were:

- Mass-selected Ru nanoparticles deposited on HOPG display a single CO desorption feature around 410–420 K followed by a broad shoulder from 480 K to 600 K. Utilising the isotope exchange reaction we have established that the larger peak at 410–420 K is principally due to molecularly desorbing CO, while the shoulder is due to desorption of dissociatively adsorbed CO.
- Successive TPD measurements result in deactivation of the nanoparticles due to sintering and/or poisoning of the catalyst surface by carbon from the support. A possible third deactivation mechanism involves annealing-out the non-equilibrium surface features of the nanoparticles.
- Ru nanoparticles grown on HOPG by vapour deposition display broadly the same characteristics as the mass-selected nanoparticles. Moreover, by annealing a PVD-grown thin film we demonstrate a crossover in CO desorption spectra from that characteristic of supported nanoparticles to one characteristic of a stepped Ru(001) single crystal surface.
- Starting from a stepped Ru(001) single crystal surface we have also demonstrated the reverse transition from single crystal to nanoparticle-like CO desorption behaviour by means of Ar^+ ion sputtering.

We have shown that it is possible to vary the desorption behaviour between the two model catalyst systems by using straightforward sample preparation methods. These results demonstrate the complementary nature of both model catalyst systems and affirm the validity of studying both in order to narrow the materials gap to more complex industrial catalysts. With further work, for example using more well-defined Wulff constructed nanoparticles or mesoscale crystals,[62] even greater insight into the crossover between the desorption behavior of single crystal surfaces and supported nanoparticles can be obtained.

This work was supported by the Danish National Research Foundation and the EU FWP7 Marie Curie Intra-European Fellowship ESRCN (PIEF-GA-2008-220055).

References

1 D. W. Goodman, *Chem. Rev.*, 1995, **95**, 523.
2 G. A. Somorjai, R. L. York, D. Butcher and J. Y. Park, *Phys. Chem. Chem. Phys.*, 2007, **9**, 3500.
3 H. Oosterbeek, *Phys. Chem. Chem. Phys.*, 2007, **9**, 3570.
4 J. Assmann, V. Narkhede, N. A. Breuer, M. Muhler, A. P. Seitsonen, M. Knapp, D. Crihan, A. Farkas, G. Mellau and H. Over, *J. Phys.: Condens. Matter*, 2008, **20**, 184017.
5 C. R. Henry, *Surf. Sci. Rep.*, 1999, **31**, 231.
6 H. J. Freund, H. Kuhlenbeck, J. Libuda, G. Rupprechter, M. Bäumer and H. Hamann, *Top. Catal.*, 2001, **15**, 201.
7 S. Haq and R. Raval, *Phys. Chem. Chem. Phys.*, 2007, **9**, 3641.
8 S. Dahl, P. A. Taylor, E. Törnqvist and I. Chorkendorff, *J. Catal.*, 1998, **178**, 679.

9 S. Dahl, A. Logadottir, R. C. Egeberg, J. H. Larsen, I. Chorkendorff, E. Törnqvist and J. K. Nørskov, *Phys. Rev. Lett.*, 1999, **83**, 1814.
10 R. A. Dalla'Betta and M. Shelef, *J. Catal.*, 1977, **48**, 111.
11 H. Abrevaya, M. J. Cohn, W. M. Targos and H. J. Robota, *Catal. Lett.*, 1990, **7**, 183.
12 R. J. Madon, S. C. Reyes and E. Iglesia, *J. Phys. Chem.*, 1991, **95**, 7795.
13 E. Shincho, C. Egawa, S. Naito and K. Tamaru, *Surf. Sci.*, 1985, **149**, 1.
14 J. C. Fuggle, E. Umbach, P. Feulner and D. Menzel, *Surf. Sci.*, 1977, **64**, 69.
15 H. Pfnür, P. Feulner, H. A. Engelhardt and D. Menzel, *Chem. Phys. Lett.*, 1978, **59**, 481.
16 P. Feulner, H. A. Engelhardt and D. Menzel, *Appl. Phys.*, 1978, **15**, 355.
17 J. A. Schwarz and S. R. Kelemen, *Surf. Sci.*, 1979, **87**, 510.
18 H. Pfnür, P. Feulner and D. Menzel, *J. Chem. Phys.*, 1983, **79**, 4613.
19 T. Yamada, Y. Iwasawa and K. Tamaru, *Surf. Sci.*, 1989, **223**, 527.
20 E. D. Westre, D. E. Brown, J. Kutzner and S. M. George, *Surf. Sci.*, 1994, **302**, 280.
21 T. Zubkov, G. A. Morgan and J. T. Yates, *Chem. Phys. Lett.*, 2002, **362**, 181.
22 T. Zubkov, G. A. Morgan, J. T. Yates, O. Kühlert, M. Lisowski, R. Schillinger, D. Fick and H. J. Jänsch, *Surf. Sci.*, 2003, **526**, 57.
23 T. E. Madey, *Surf. Sci.*, 1979, **79**, 575.
24 G. E. Thomas and W. H. Weinberg, *J. Chem. Phys.*, 1979, **70**, 1437.
25 H. Pfnür, D. Menzel, F. M. Hoffmann, A. Ortega and A. M. Bradshaw, *Surf. Sci.*, 1980, **93**, 431.
26 E. D. Williams and W. H. Weinberg, *Surf. Sci.*, 1979, **82**, 93.
27 G. Michalk, W. Moritz, H. Pfnür and D. Menzel, *Surf. Sci.*, 1983, **129**, 92.
28 H. Pfnür and D. Menzel, *Surf. Sci.*, 1984, **148**, 411.
29 P. Jakob, *J. Chem. Phys.*, 2004, **120**, 9286.
30 S. Kneitz, J. Gemeinhardt and H. P. Steinrück, *Surf. Sci.*, 1999, **440**, 307.
31 S. H. Payne, J. S. McEwen, H. J. Kreuzer and D. Menzel, *Surf. Sci.*, 2005, **594**, 240.
32 S. B. Vendelbo, M. Johansson, D. J. Mowbray, M. P. Andersson, F. Abild-Pedersen, J. H. Nielsen, J. K. Nørskov and I. Chorkendorff, *Top. Catal.*, 2010, **53**, 357.
33 P. D. Reed, C. M. Comrie and R. M. Lambert, *Surf. Sci.*, 1976, **59**, 33.
34 R. Ku, N. A. Gjostein and H. P. Bonzel, *Surf. Sci.*, 1977, **64**, 465.
35 G. Lauth, T. Solomun, W. Hirschwald and K. Christmann, *Surf. Sci.*, 1989, **210**, 201.
36 G. Rotaris, A. Baraldi, G. Comelli, M. Kiskinova and R. Rosei, *Surf. Sci.*, 1996, **359**, 1.
37 J. Wang, Y. Wang and K. Jacobi, *Surf. Sci.*, 2001, **488**, 83.
38 J. G. McCarty and H. Wise, *Chem. Phys. Lett.*, 1979, **61**, 323.
39 G. G. Low and A. T. Bell, *J. Catal.*, 1979, **57**, 397.
40 E. Zağli and J. L. Falconer, *J. Catal.*, 1981, **69**, 1.
41 H. M. Miura, M. L. McLaughlin and R. D. Gonzalez, *J. Catal.*, 1983, **79**, 227.
42 N. Kakuta and J. M. White, *J. Catal.*, 1986, **97**, 150.
43 R. M. Nielsen, S. Murphy, C. Strebel, M. Johansson, J. H. Nielsen and I. Chorkendorff, *Surf. Sci.*, 2009, **603**, 3420.
44 R. M. Nielsen, S. Murphy, C. Strebel, M. Johansson, I. Chorkendorff and J. H. Nielsen, *J. Nanopart. Res.*, 2010, **12**, 1249.
45 J. H. Nielsen, L. Bech, K. Nielsen, Y. Tison, K. P. Jørgensen, J. L. Bonde, S. Horch, T. F. Jaramillo and I. Chorkendorff, *Surf. Sci.*, 2009, **603**, 1182.
46 F. Besenbacher, E. Lægsgaard, K. Mortensen, U. Nielsen and I. Stensgaard, *Rev. Sci. Instrum.*, 1988, **59**, 1035.
47 S. Murphy, R. M. Nielsen, M. Johansson and J. H. Nielsen, *Carbon*, 2011, **49**, 376.
48 Therefore, some surface defects may have been formed on the HOPG by accelerated positive Ru ions coming from the electron-beam evaporator.
49 Our measurements indicated a concentration of approximately 1% $^{13}C^{18}O$ in the $^{13}C^{16}O$ dosing gas.
50 The only differences were that the reduction step was carried out for 20 min and the final anneal step in UHV was carried out at 1400 K for 2 min.
51 The corresponding diameter of a sphere with the selected mass is used to identify the nanoparticles.
52 C. Park, W. G. Durrer, H. Poppa and J. T. Dickinson, *J. Catal.*, 1985, **95**, 361.
53 P. A. Redhead, *Vacuum*, 1962, **12**, 203.
54 I. Chorkendorff and J. W. Niemantsverdriet, *Concepts of Modern Catalysis and Kinetics*, Wiley, 2007.
55 J. Gavnholt and J. Schiøtz, *Phys. Rev. B: Condens. Matter*, 2008, **77**, 035404.
56 Here we have used the notation for stepped surfaces to describe the Ru(1 1 10) surface.
57 P. Jakob, M. Gsell and D. Menzel, *J. Chem. Phys.*, 2001, **114**, 10075.
58 G. L. Bezemer, J. H. Bitter, H. P. C. E. Kuipers, H. Oosterbeek, J. E. Holewijn, X. Xu, F. Kapteijn, A. J. van Dillen and K. P. de Jong, *J. Am. Chem. Soc.*, 2006, **128**, 3956.
59 H. I. Lee, B. E. Koel, W. M. Daniel and J. M. White, *J. Catal.*, 1982, **74**, 192.
60 K. L. Kostov, H. Rauscher and D. Menzel, *Surf. Sci.*, 1992, **278**, 62.
61 M. Mavrikakis, B. Hammer and J. K. Nørskov, *Phys. Rev. Lett.*, 1998, **81**, 2819.
62 N. Tian, Z. Y. Zhou, S. G. Sun, Y. Ding and Z. L. Wang, *Science*, 2007, **316**, 732.

Strong Cu-ZnO interaction in industrial type methanol synthesis catalysts: Quantification of Zn atoms in the Cu surface

S. Kuld, C. Conradsen, I. Chorkendoff and S. Sehested

Abstract

Methanol synthesis has attracted renewed interest recently due to its potential importance as a solar fuel and its importance in chemical industry in general. In particular, the influence of ZnO on the activity for Cu/ZnO based methanol catalysts has been a subject of discussion. Here we observe a structural alteration of the measured specific Cu area of an industrial type MeOH catalyst ($Cu/ZnO/Al_2O_3$) that is strongly dependent on the pretreatment. The combination of H_2-Temperature Programmed Desorption, N_2O Reactive Frontal Chromatography, H_2-Transient Adsorption and X-ray Photoelectron Spectroscopy analysis provides a consistent explanation of surface alloying between Cu and Zn. The applied analysis enables a reinterpretation of the techniques used for determination of the Cu surface area providing quantification of the specific Cu and Zn areas independently.

Introduction

Methanol is an important chemical that is used for production of formaldehyde, acetic acid, MTBE, MTO, Gasoline blending, DME etc. The use of methanol is growing especially as an energy carrier and synthetic substitute for conventional fuels [1,2]. Synthesis of methanol is carried out over a $Cu/ZnO/Al_2O_3$ methanol catalyst that has been used industrially since the 1960ties. The $Cu/ZnO/Al_2O_3$ catalyst has been subject of intensive research for decades but nevertheless the nature of the active site is still debated. It is widely accepted that ZnO in methanol catalysts increase activity of these Cu based systems [3,4]. The exact role of the ZnO is however not perfectly clear. At reducing conditions the presence of ZnO_x species has been reported to partly cover the Cu particles as a result of Strong Metal Support Interaction (SMSI) [4-9]. A previous study combining N_2O RFC, H_2-TPD with a pretreatment in reducing atmospheres showed a change in the copper area linked with a transient maximum of methanol synthesis activity [10]. Studies of model systems of Cu/ZnO report that pretreatments influence the morphology of Cu nanoparticles explained by the formation of strong binding oxygen vacancies in the ZnO [6,11]. In addition, ambient pressure XPS on Cu/ZnO catalysts of high Cu content has shown surface decoration of ZnO_x species on Cu nanoparticles at relative mild conditions [4,12].

In this study the, nature of the SMSI between ZnO_x and Cu under reducing conditions is investigated for an industrial type methanol catalyst. A systematic examination using several techniques has shown significant dynamical changes in the state of the Cu surface as a consequence of an increasing partial pressure of hydrogen. This study elucidates the pitfalls in chemisorption methods for determination of the Cu surface area and offer a more accurate determination of the specific Cu surface area together with strong evidence that Zn is present in the metallic state in a Cu-Zn-surface-alloy. The surface sensitive methods provide information of the specific copper and zinc areas as a function of the partial pressure of hydrogen during pretreatment. The

methods provide quantitative information of the Zn oxidation state and coverage on Cu surfaces as a function of the pretreatment.

The same catalyst is treated by two parallel experimental sequences in a fixed bed reactor system and a combined HPC (High Pressure Cell) and UHV (Ultra High Vacuum) setup. In figure 1 the experimental procedure is schematically illustrated.

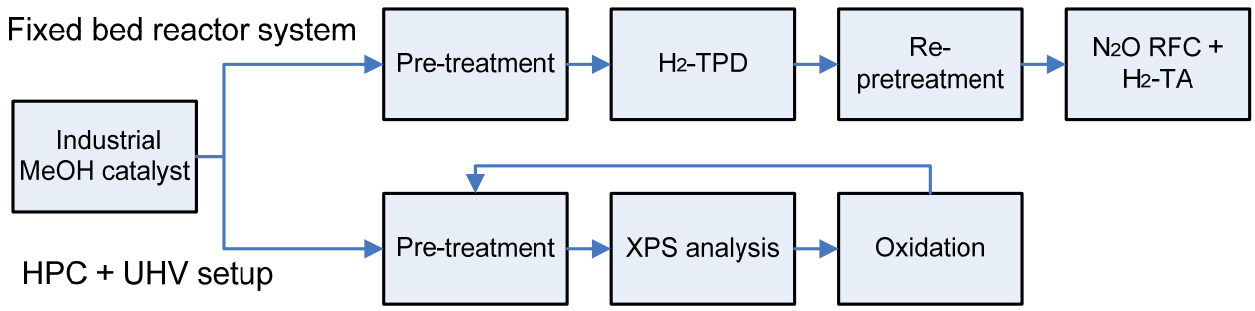

Figure 1: The figure shows a schematic block diagram of the experimental treatment sequences applied in the present work. The top route is applied in a fixed bed reactor system, while the bottom sequence is applied in the combined HPC and UHV system

Measurements of specific Cu areas are carried out in a fixed bed flow set-up described in [13] and equivalent to that discussed in [14]. Gases of high purity are used: He (99.9999%), H_2 (99.9999%), H_2/He (1% H_2, 99.9995%), N_2O/He (1% N_2O, 99.9995%). Fast online gas analysis is performed by a calibrated quadrupole mass spectrometer (Balzers GAM 445).

For each experiment, 200 mg of catalyst with a sieve fraction between 150-300 µm are loaded into a U-shaped quartz reactor with an inner diameter of 4 mm. The $Cu/ZnO/Al_2O_3$ catalyst used for the present experiments is an industrial type $Cu/ZnO/Al_2O_3$ catalyst (60:25:15) [mol%] made by co-precipitation according to [15]. The catalyst is heated in dry synthesis gas ($CO:CO_2:H_2$ = 5:5:90) at 220°C for 72 h prior to the presented work.

Prior to each Cu surface area measurement the catalysts is reduced in 140 ml/min of an 1% H_2/He gas mixture by ramping the temperature by 2 K min^{-1} from 300 to 493 K. Directly after the activation procedure, the sample is subjected to a pre-treatment in different partial pressures of H_2. During the pre-treatment, the temperature is maintained at 493 K for 16 hours. Subsequently, the reactor is purged for 0.5 h with 100 ml/min of He and cooled to the desired temperature to achieve an adsorbate-free reduced Cu surface.

A two-step series of experiments are applied for each set of different pre-treatment conditions. The first step consists of Cu area determination by temperature programmed desorption of H_2 (H_2-TPD) subsequent to the pre-treatment. The H_2-TPD is known to be nondestructive with respect to the Cu surface area [13]. The second step implies a re-reduction and pre-treatment followed by a N_2O reactive frontal chromatography (N_2O RFC) at 50°C [16] and H_2 transient adsorption (H_2-TA) at room temperature. The re-reduction and pre-treatment is done in order to ensure that H_2-TPD and N_2O-RFC are conducted with the on same basis. After each experiment series, the catalyst sample is replaced. The area determination sequence is selected to eliminate the possibility

of sintering caused by the N_2O chemisorption procedure [13]. The experimental details of the H_2-TPD, N_2O-RFC and H_2-TA are described in the supplementary material.

To determine the copper surface area by the H_2-TPD experiments we follow the procedure described in [13]. Based on previous TPD studies of hydrogen on Cu single crystals the saturation coverage of hydrogen on all low-index planes of Cu is reported to be half a monolayer (θ_H=0.5 ML) [17]. However, at the applied experimental conditions it is only possible to achieve an equilibrium coverage of 80% of the saturation coverage, i.e. θ_H=0.4 ML [*13*].

Using that each hydrogen atom is bridging two Cu surface atoms [13], the corresponding equation for the dissociative adsorption of H_2 on the Cu surface is:

$$\mathrm{H_{2(g)}} + 4\mathrm{Cu_{(s)}} \rightarrow 2(\mathrm{Cu\text{-}H\text{-}Cu})_{(s)}$$

The surface area of the Cu particles is calculated by assuming a molecular stoichiometry of Cu_s/H_2 = 4, an equilibrium coverage of 0.4 ML, and a number of Cu atoms per unit area of 1.46×10^{19} copper atoms m^{-2} [3].

The copper surface area is equivalently determined by N_2O RFC as reported in [16]. The temperature of the catalyst during the N_2O RFC measurement is 323 K, which is chosen for selective chemisorption of N_2O while minimizing sub-surface oxidation.

Immediately after the N_2O titration process, the gas mixture is changed to pure He and the temperature is lowered to ambient temperature. After purging the catalyst for a short period, the gas mixture is changed to a 1% H_2/He gas composition. The catalyst is exposed to the H_2/He mixture for 1 hour while monitoring the H_2 uptake. This treatment results in a delayed consumption of hydrogen emerging after a few minutes exposure and lasting for around 10 min. An example of a hydrogen uptake curve is seen in the supplementary material. The hydrogen uptake is a titration of the chemisorbed oxygen in the copper surface and is named here as Hydrogen Transient Adsorption (H_2-TA).

The X-ray Photoelectron Spectroscopy (XPS) measurements are performed in an Ultra High Vacuum (UVH) setup with a base pressure of 10^{-10} Torr. The catalyst can be transferred to a High Pressure Cell (HPC) for pre-treatment. The pressure in the HPC is controlled by a pressure controller to 1 bar and the gas flow of He and H_2 or oxygen is controlled by mass flow controllers. For the XPS measurements the x-rays are generated from a dual anode x-ray source from SPECS using Al K_α radiation with photon energy of 1486.3 eV while the photoelectrons are measured with a Phoibos Hemispherical Energy Analyzer.

An industrial type $Cu/ZnO/Al_2O_3$ catalyst and pure ZnO powder (Transpek-Silox Industry, India) are pressed to a tablet and placed in a custom-made stainless steel sample holder. The sample is suspended on tungsten wires, which act as filament for heating. The holder fixates the catalyst tablet and has circular opening of 4 mm diameter as a XPS window. The catalyst tablet is transferred to UHV and heated to 120^{o}C for two hours to remove water. The temperature is measured by a C-type thermocouple clamped between catalyst and sample holder. After the initial characterization, the catalyst is transferred back to the HPC and exposed to a

pretreatment identical to the one used for the area sensitive techniques. The surface is reset by heating to 70°C in 5.000 ppm O_2/Ar for 16 hours between each pre-treatment.

The XPS characterization subsequent to the pre-treatment is conducted to examine the extent to which metallic Zn is present in the surface of the catalyst. In Figure 2a the $L_3M_{4,5}M_{4,5}$ auger peak is shown for the Cu/ZnO/Al_2O_3 catalyst for hydrogen pretreatment pressures between 0.01 to 1 bar. In Figure 2b the Auger line for the pure ZnO reference and the Cu/ZnO/Al_2O_3 system before and after a pre-treatment at 1 bar H_2 is displayed. The positions of all auger peaks are aligned by the C1s peak. For the Cu/ZnO/Al_2O_3 a Shirley background is subtracted and normalized to the peak height of the ZnO feature.

The single peak In Figure 2a is resolved during acquisition of XPS data. A shoulder feature appears at 3 eV lower binding energy for the Cu/ZnO/Al_2O_3 catalyst subsequent to the pretreatment in 0.01 bar of hydrogen. The shoulder feature becomes more pronounced for higher partial pressures of hydrogen. In Figure 2b the pure ZnO tablet is reduced at 1 bar H_2 for 16 hours with no effect on the auger peak in clear contrast to the Cu/ZnO/Al_2O_3 catalyst.

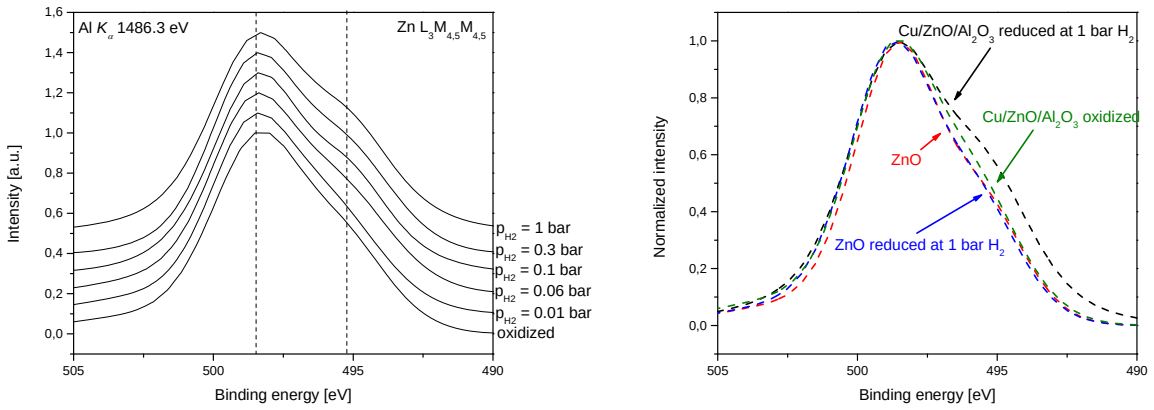

Figure 2: Figure A shows the $L_3M_{4,5}M_{4,5}$ Auger peaks for the oxidized and reduced Cu/ZnO/Al_2O_3 catalyst. The figure B shows the reference sample of pure ZnO, the reduced ZnO and Cu/ZnO/Al_2O_3 catalyst oxidized and reduced

The Cu areas measured on the Cu/ZnO/Al_2O_3 catalyst after pretreatments in different partial pressures of hydrogen are plotted in Figure 3. The Cu area is determined by both the H_2-TPD, N_2O RFC and H_2-TA methods and is evaluated as the area of the Cu surface per catalyst weight. Subsequent to a pretreatment in 0.01 bar of hydrogen, the N_2O titration method and the H_2-TPD return essentially the same Cu area of around 16.5 m^2/g. H_2-TA gives a slightly lower area (-13%). This is ascribed to incomplete reduction of Cu_2O as described in the supplementary material. The Cu area determined by N_2O RFC is observed to increase with the partial pressure of hydrogen except for the pretreatment in 0.05 bar hydrogen. The surface area of the same catalyst determined by H_2-TPD and H_2-TA is observed to decrease as a function of the hydrogen partial pressure. Despite the relative low pressures of hydrogen during pretreatment, the impact on the surface area determined with the three different methods are substantial i.e. up to ±60-65%. Note that the average of the

surface area based on the N_2O RFC and H_2-TPD displayed in Figure 3 (blue dots) is approximately a constant independent of the pretreatment.

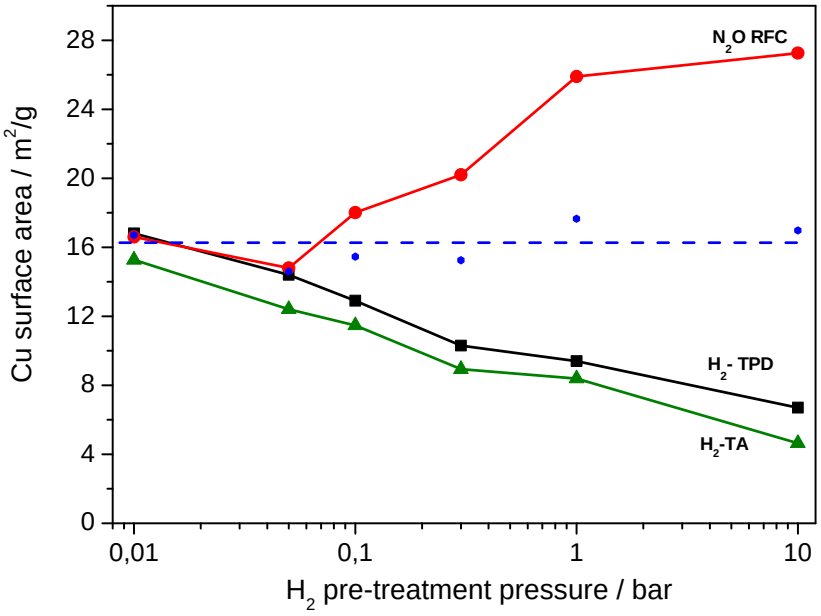

Figure 3: The figure shows the change in Cu surface area as determined by N_2O RFC (red), H_2-TPD (black) and H_2-TA (green) by applying a pretreatment in different partial pressures of H_2 for 16h. The average of the Cu areas determined using H_2-TPD and N_2O RFC are plotted with blue dots. The blue dashed line is to guide the eye.

The reduction of ZnO to Zn is not trivial to detect by XPS. The Zn $2p_{3/2}$ lines for Zn and ZnO are positioned at 1021.4 eV and 1021.7 eV, respectively [18]. The change in valence state for Zn(II) to Zn(0) is observed as a more pronounced 3 eV downward shift in binding energy of the $L_3M_{4,5}M_{4,5}$ Auger peak (see supplementary). Hence the shoulder feature appearing as a consequence of the pretreatment in Figure 2a is assigned to originate from metallic Zn. The Auger peaks are fitted as a linear combination of the oxidized Auger peak and the oxidized Auger peak shifted 3 eV downwards in binding energy. A deconvolution of the fit allows for a quantification of the peak areas assigned to metallic Zn and ZnO and thereby determine the extent of metallic Zn in the surface layers of the catalyst. In Figure 4 the change in the peak-areas of Zn and ZnO are shown for different pretreatment conditions for both the $Cu/ZnO/Al_2O_3$ catalyst and the pure ZnO reference. A gradual enrichment of metallic Zn up to 10% is observed for the $Cu/ZnO/Al_2O_3$ catalyst subsequent to the pretreatment. A reference ZnO sample was exposed to 1 bar of H_2 and no metallic Zn was measured. These measurements demonstrate the importance of copper for catalyzing the reduction of ZnO.

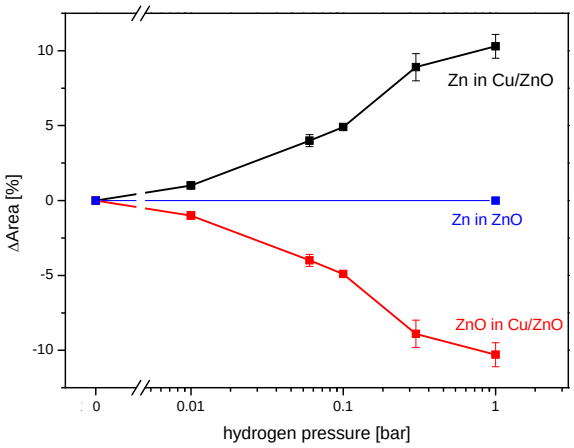

Figure 4: The figure shows the change in area of the ZnO (red) and Zn (black) Auger peak for the industrial Cu/ZnO/Al_2O_3 catalyst and for the change in area for the ZnO reference (blue).

Previous STM studies of Zn deposition on Cu(111) single crystals have shown that a Cu-Zn surface alloy is formed by random substitution of the Zn atoms homogeneously into the Cu(111) surface layer [19,20]. The fact that metallic Zn is observed by XPS provides strong evidence that ZnO is reduced into *metallic* Zn at the interface between the Cu and ZnO particles followed by the formation of a Cu-Zn surface alloy. The formation of a Cu-Zn surface alloy is additionally supported by the data in Figure 3 as discussed in the following.

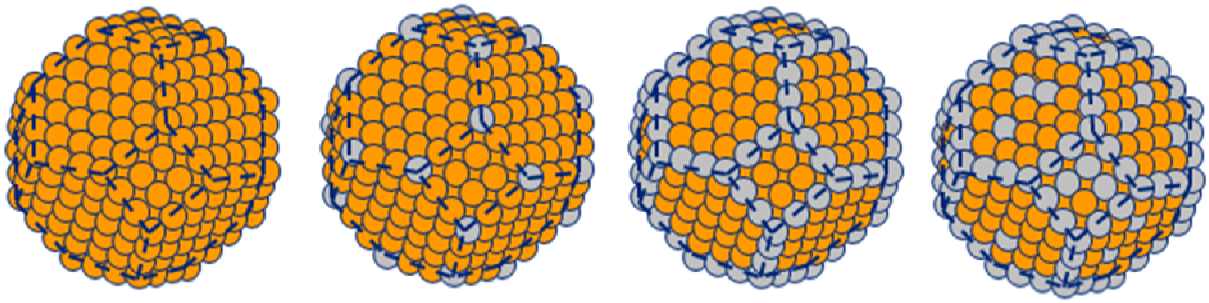

Figure 5: The figure shows an illustration of the progress in Cu-Zn alloying as a consequence of the pre-treatment.

The measurements of the Cu surface area by N_2O-RFC and H_2-TPD deviates to an increasing extend as the partial pressure of H_2 is raised during the pretreatment as seen in Figure 3. The Cu area determined by N_2O RFC is relying on the assumption of only Cu is present in the metallic state. Hence, the Cu surface is solely responsible for the oxygen adsorption during the N_2O decomposition. However, the oxidation process is not selective in its nature. The incorporation of the reduced Zinc atoms found by XPS in the surface of the copper

nanoparticles will increase the oxygen uptake from N_2O as a Zn atom incorporated into the Cu surface is expected to react with one N_2O molecule while a surface Cu atom only reacts with 0.5 N_2O molecule.

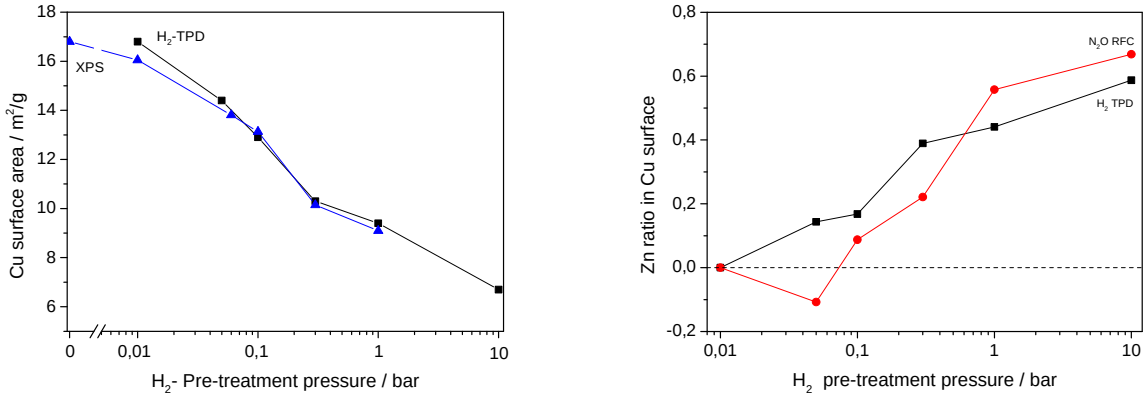

Figure 6: A shows the correlation between the Cu surface areas determined by H_2-TPD and based on the XPS data by applying a simple model. B shows ratio of Zn enrichment in the Cu surface evaluated for both the N_2O RFC and H_2-TPD techniques.

Contrary, to N_2O RFC, the H_2-TPD peak decrease with increasing p_{H2} during the pretreatment. The H_2-TPD technique is based on the specific desorption profile associated with only metallic Cu. Hence, incorporation of reduced Zn at the surface of the Cu particles decrease the Cu area measured by the H_2-TPD method. Density Functional Theory, DFT, calculations show that the hydrogen adsorption energy at Zn sites incorporated in a Cu(111) surface will decrease by 28 kJ/mol compared to that at a clean Cu(111) surface (see supplementary material). This means reduction in the peak area of the H_2-TPD can be directly assigned to a loss of Cu surface area and show that Zn is incorporated into the surface of the Cu particles. An illustration of the progressive Cu-Zn alloy formation is shown schematically in Figure 5.

The formation of Cu-Zn surface alloy is supported by a comparison of the XPS data and the Cu area determined by H_2-TPD through a simple geometric model. In the model, the fraction of reduced and oxidized Zn is used and it is assumed that each metallic Zn atom replaces a Cu surface atom (see supplementary material). Figure 6a displays the specific Cu surface area as a function of the H_2 pre-treatment pressure for XPS as calculated by the simple geometric model and evaluated by H_2-TPD assuming that the latter probes the Cu surface atoms. The nice correlation between the metallic Zn measured by XPS and the decrease in Cu surface area determined by H_2-TPD seen from the graph in Figure 6a, lends credit to H_2-TPD as an accurate method for determining the specific Cu (Zn free) surface area.

The area derived from the H_2-TA experiment is evaluated by assuming water is formed in the reduction of oxygen chemisorbed at the Cu surface and subsequently transferred to the support [21]. Despite the fact that the area determined by N_2O is increasing with pre-treatment pressure the amount of H_2 consumed during the H_2-TA experiment is decreasing in the same way as the H_2-TPD. This observation is very reasonable in the context of Cu-Zn surface alloying. The Zn enrichment in the Cu surface leads to the formation of ZnO during N_2O RFC. The less reducible nature of ZnO prohibits H_2 consumption during the H_2-TA experiment. The H_2-TA

experiment probes the oxygen in the Cu_2O surface oxide formed during the N_2O RFC experiment but not ZnO in the Cu surface.

Finally, the data in Figure 1Figure 3 enables the quantification of metallic Zn in the Cu-Zn surface alloy. The change in observed surface area relative to that measured after the pretreatment in 10 mbar H_2 is interpreted as a change in Zn/Cu element ratio in the surface of the Cu particles. In Figure 6B the ratio of Zn in the Cu surface is evaluated for the H_2-TPD and the N_2O RFC experiment, respectively. The zinc enrichment in the copper surface as a function of the pretreatment is seen to be similar even though two independent techniques are applied. This fact consolidates the explanation of a Cu-Zn surface alloy formation. The Zn enrichment in the Cu surface is observed to reach approximately 60 % for a 16 h pretreatment in 10 bar H_2. This observation is remarkable taking into account the relative mild conditions applied during the pretreatment. Another interesting observation is that the average surface area measured by N_2O-RFC and H_2-TPD is approximately independent of the hydrogen pretreatment pressure - see Figure 3. This indicates that the total geometric surface area of the Cu particles is virtually unchanged during the reduction process perhaps because wetting of particles of similar size does not strongly change the exposed Cu surface area.

In summary, the combined study of XPS, H_2-TPD, N_2O RFC and H_2-TA, has provided clear evidence of a surface decoration of metallic Zn present on Cu particle surface. Merging the techniques elegantly gives insight to the debated origin of surface ZnO_x species. Subsequent to different pretreatment, XPS clearly showed an enhancement of the metallic Zn feature in the $L_3M_{4,5}M_{4,5}$ Auger peak increasing with the partial pressure of H_2. The presence of copper particles was found to be essential for reducing ZnO. Complementary surface sensitive methods in the case of N_2O titration showed an increase in the oxygen uptake from nitrous oxide while secondary H_2-TA and the H_2-TPD experiments showed a decrease in adsorbed and desorbed hydrogen, respectively. The experimental observations were consistent with the formation of a Cu-Zn surface alloy formation during the pretreatment. The interplay between the evaluated surface areas of the N_2O RFC and H_2-TPD techniques can be utilized to quantify the amount of metallic Zn in the Cu surface. This study provides a reinterpretation and a more accurate determination of the specific Cu surface determination based on specific area measurements of four independent and consistent techniques.

References:

[1] Olah G. A. Chemical and Engineering News, 81, 2003, 5-5
[2] Olah G. A. Angewandte Chemie International Edition, 52, 2013, 104-107
[3] O. Heinrichsen, T. Genger and M. Muhler, Chem. Eng. Technol 23, 2000, 11
[4] M. Behrens, F. Studt, I. Kasatkin, S. Kühl, M. Hävecker, F. Abild-Pedersen, S. Zander, F. Girgsdies, P. Kurr, B. L. Kniep, M. Tovar, R. W. Fischer, J. K. Nørskov and R. Schlögl, Science, 336, 2012, 893-897
[5] R. N. d'Alnoncourt, X. Xia, J. Strunk, E. Löffler, O. Hinrichsen and M. Muhler, Phys. Chem. Chem. Phys. 8, 2006, 1525-1538
[6] J.D. Grunwaldt, A. M. Molenbroek, N.Y. Topsøe, H. Topsøe, and B. S. Clausen, Journal of Catalysis, 194, 2000, 452-460
[7] Y. Kanai T. Watanabe, T.Fujitani, M. Saito, J.Nakamura and T.Uchijima, Catalysis Letters, 27, 1994, 67-78
[8] N. Y. Topsøe and H. Topsøe, Topics in Catalysis, 8, 1999, 267-270
[9] E.D. Batyrev, J.C. vanden Heuvel, J. Beckers, W.P.A. Jansen, and H.L. Castrium, J. Catal. 229 (2005) 136-142

[10] H. Wilmer, T. Genger, and O. Hinrichsen, Journal of Catalysis 215 (2003) 188–198
[11] P.C.K. Vesborg, I. Chorkendorff, I. Knudsen, O. Balmes, J. Nerlov, A. M. Molenbroek, B. S. Clausen,S. Helveg, Journal of Catalysis, 262, 2009, 65-72
[12] S. Zander, E. L. Kunkes, M. E. Schuster, J. Schumann, G. Weinberg, D. Teschner, N. Jacobsen, R. Schlögl and M. Behrens, Angew. Chem. Int. 52, 2013, 6536-6540
[13] M. Muhler, L. P. Nielsen, E. Törnqvist, B .S Clausen and H. Topsøe. Catal.Lett, 1992, 14, 241
[14] T. Genger, O. Hinrichsen and M. Muhler. Catal.Lett., 1999, 59, 137
[15] Baltes, S. Vukojevic, F. Schüth, Journal of Catalysis, 258, 2008, 334–344
[16] G. C. Chinchen, C.M. Hay, H.D. Vendervell, K.C Waugh, J. Catal, 1987, 79, 103
[17] G. Anger, A. Winkler and K.D. Rendulic, Surf. Sci. 1989, 220, 1.
[18] Y.K. Gao, F. Traeger, O. Shekhah, H. Idriss, C. Woll, J. Colliod Interface Sci. 338 (2009) 16
[19] M. Sano, T. Adaniya, T. Fujitani and J. Nakamura, J. Phys. Chem. B., 106, 2002, 7627-7633
[20] M. Sano, T. Adaniya, T. Fujitani, J. Nakamura, Surf. Sci. 514, 2002, 261-266
[21] O. Hinrichsen, T. Genger and M. Muhler, Stud. Surf. Sci. Catal. 130, 2000, 3825-3830

Catalytic activity of model- and high surface area Cu/Ru catalyst for low temperature ammonia oxidation

C. Conradsen, S. Olesen, D. Chakraborty, I. Chorkendorff.

Abstract

A surface science study of a pseudomorphic copper layer on a ruthenium thinfilm is found to perform better than both pure copper and ruthenium towards ammonia oxidation. The Cu/Ru system is investigated with XPS and ISS and an optimal surface coverage of copper of 0.78 ML is found. The improved activity of the pseudomorphic overlayer can be explained by the d-band model and a strain of the copper lattice. The copper overlayer is proven to work in both a model system and under more realistic conditions on a high surface area support in a plug flow reactor. Incorporating copper in the ruthenium thinfilm is further found not to have the same beneficial effect as the overlayers.